UNIVERSITY OF CALIFORNIA, SAN DIEGO

Multiscale Dynamics of Atmospheric and Oceanic Variability in the Climate System

A dissertation submitted in partial satisfaction of the
requirements for the degree
Doctor of Philosophy

in

Oceanography

by

Aneesh C. Subramanian

Committee in charge:

    Art Miller, Chair
    Bruce Cornuelle, Co-Chair
    Sarah Gille
    Philip Gill
    Myrl Hendershott
    Markus Jochum
    Raghu Murtugudde
    Rick Salmon

2012

The dissertation of Aneesh C. Subramanian is approved,
and it is acceptable in quality and form for publication
on microfilm and electronically:

_____

_____

_____

_____

_____

_____
                                          Co-Chair

_____
                                            Chair

University of California, San Diego

2012

DEDICATION

To my parents for the gift of life

and to my teachers, family and friends

who taught me how to extract sweetness from life.

Joseph L. Reid, premier physical oceanographer at Scripps Institiution of Oceanography, La Jolla, Calif., received the highly prized Albatross Award at the 1988 Joint Oceanographic Assembly in Acapulco "for his outrageous insistence that ocean circulation models should bear some resemblance to reality."
— Stevenson, R. E. (1988), Eos Trans. AGU, 69(49), 1628

Joe Reid and the Albatross Award, 1988

The fox knows many things but the hedgehog knows one big thing.
—Archilochus, Greek poet

TABLE OF CONTENTS

LIST OF FIGURES

ACKNOWLEDGEMENTS

No one deserves more thanks for the success of this work than my wonderful advisers **Art Miller** and **Bruce Cornuelle** and co-advisers **Raghu Murtugudde**, **Markus Jochum**. I wholeheartedly thank them for their continuous encouragement, guidance and support.

I thank **Art Miller** for his continued support as an adviser, teacher, colleague and foremost, as a friend. I always looked upon him for advice - academic or non-academic. He very patiently critiqued my research methods and let me develop an independent research approach which I will always cherish! I feel that I am more disciplined, simple and confident after working under his guidance. The opportunity to watch **Bruce Cornuelle** in action (particularly during the discussions) has fashioned my way of thought in problem solving. He has been a valuable adviser, and I hope my four and half years of working with him have left me with atleast few of his qualities and a fraction of his endless knowledge. I am deeply grateful to **Raghu** for his continued trust and for all the research ideas he has shared with me over the years. I am highly indebted to **Markus** for his time in advising and guiding me with research on CCSM and all the help rendered in visits to NCAR. Without their trust and guidance this thesis would not have been possible.

Special thanks to my brilliant friend, colleague and adviser **Ibrahim Hoteit** for his perseverance and belief in our work with particle filters and many helpful suggestions on the research. It has always been great fun to work and argue about filtering with him. I thank my committee members, **Rick Salmon, Myrl Hendershott, Philip Gill and Sarah Gille** for their time and effort and for making themselves available during their busy schedules for many engaging and stimulating discussions.

Special thanks go to **Andy Moore, Hernan Arango and Manu Di Lorenzo** for personally sharing their expertise with ROMS. Also, special thanks to the CCSM group at NCAR, specifically, **Mitch Moncrieff, Rich Neale, Frank Bryan, Dennis Shea** and everyone else in CGD, NCAR for making my stay at NCAR a very memorable one scientifically and personally.

I am privileged to learn from the great teachers: **Glenn Ierley, Clint Winant, Rick Salmon, Myrl Hendershott, Bob Guza, Philip Gill, Paola Cessi, Joel Norris, Ken Melville, Peter Franks and Lynne Talley**. I thank them for imbibing in me the rigor of mathematics and physics required to study ocean-atmosphere dynamics. I will cherish the many timeless conversations with Glenn Ierley on topics from mathematics in the world to the world and its meaning. I wish to thank Caroline for her selfless help with compas, our computing cluster and the SIO graduate office which made me feel welcome and wanted at SIO for the past five years.

I wish to thank all my friends at SIO, to name only a few: **Ben, Yvonne, San, Peter, Gordy, James, Mike, Shang, Tom, Miller group: Dian, Lauren, Mike, Ankur, Nick, Ryan** for the many hours of togetherness, surf and sun. I also wish to thank the "**pier gladiators**", who have very rarely failed to organize "a soccer game a week", for keeping me sane. A very special thanks to my dear former officemate, **Hajoon Song** who always helped me with matlab code, discussing assimilation theory, chatting or playing sports.

A very special thanks to **Mani, Arvind, Shyam** for bitter and sweet times of road trips and unending entertaining conversations. Thanks to **Ambi, Sai, Joel, Asitu**. A very special sense of gratitude and sentiment for **Donata** for all the kind patience and belovedness showered on me. I am indebted to my brother **Hemang** and his wife for their prayers. My special thanks are due to my sister **Susmitha** and her husband. The three great new people in my life: my nephew **Abhinav** (3 years), niece **Abyukta** (6 mos) and the new life in my sister's womb will always be dear to me. I am forever indebted to my **father** for his continuous guidance and patience despite all my ignorance. I owe everything to my **mother** for taking care of every need of mine. I dedicate this thesis to my parents and to my teachers and family.

and D. Waliser, "The MJO in CCSM4", J. Climate 24, 6261-6282 (2011). The dissertation author was the primary investigator and author of this paper.

Chapters 4 and 5, in part, are material being prepared for submission as: A. Subramanian, A. Miller and B. Cornuelle, E. di Lorenzo, Fiamma Straneo and Bob Weller, "Structure, properties and heat content of eddies in the Southeast Pacific Ocean during VOCALS-REx: An Ocean State Estimate Study", In Preparation (2012). The dissertation author was the primary investigator and author of this manuscript.

Chapter 6, in part, is a reprint of material as it appears in A. Subramanian, I. Hoteit, B. Cornuelle, A. Miller and H. Song, "Linear vs Non- linear Filtering with scale selective corrections for balanced dynamics in a simple atmospheric model", J. Atm. Sci. subjudice (2011). The dissertation author was the primary investigator and author of this paper.

<center>VITA</center>

2004	B. Tech. in Naval and Ocean Engg., Indian Institute of Technology, Madras, India.
2006	M. Sc. in Mech. Engg., Indian Institute of Science, Bangalore, India.
2012	Ph. D. in Oceanography, University of California, San Diego

<center>PUBLICATIONS</center>

A. Subramanian, I. Hoteit, B. Cornuelle, A. Miller and H. Song, "Linear vs Nonlinear Filtering with scale selective corrections for balanced dynamics in a simple atmospheric model," J. Atm. Sci. subjudice (2011).

H. Song , I. Hoteit, B. D. Cornuelle, A. Subramanian, "An Adjoint-Based Adaptive Ensemble Kalman Filter," Mon. Wea. Rev. *subjudice* (2010).

A. Subramanian, M. Jochum, A. Miller, R. Murtugudde, R. Neale and D. Waliser, "The MJO in CCSM4," J. Climate **24**, 6261-6282 (2011).

H. Song , I. Hoteit, B. D. Cornuelle, A. Subramanian, "An adaptive approach to mitigate background covariance limitations in the ensemble Kalman filter," Mon. Wea. Rev. **138**, 2825-2845 (2010).

ABSTRACT OF THE DISSERTATION

Multiscale Dynamics of Atmospheric and Oceanic Variability in the Climate System

by

Aneesh C. Subramanian

Doctor of Philosophy in Oceanography

University of California, San Diego, 2012

Art Miller, Chair
Bruce Cornuelle, Co-Chair

Multiscale dynamics in the atmosphere-ocean system is ubiquitous from dust devils in the garden to tropical cyclones to mesoscale eddies in the ocean and deep ocean circulation. The purpose of this thesis is to advance ocean-atmosphere general circulation modeling and methodologies for data assimilation in order to resolve more pieces of the climate modeling puzzle than before. Specifically, it focuses on modeling the Madden-Julian Oscillation in a climate model and modeling mesoscale eddies in a regional ocean model with data assimilation. While most climate models today fail to simulate even the large-scale features of the MJO, we find that CCSM4 reproduces many realistic aspects of MJO behavior. CCSM4

produces coherent, broadbanded and energetic patterns in eastward propagating intraseasonal zonal winds and OLR in the tropics with MJO-like characteristics. Broadscale patterns, as revealed in combined EOFs of U850, U200 and OLR, are remarkably consistent with observations and indicate that convective coupling occurs in the simulated MJOs. Relations between the MJO in the model and its concurrence with other climate states reveal that higher amplitude MJO activity occurs during weak warm ENSO events and during periods of weak meridional shear and negative zonal shear during the Indian Monsoons. MJO response to anthropogenic climate change is assessed using CCSM4 in a second study. In global warming scenarios, the model simulation indicates an increase in the number of days with higher amplitude MJOs and also a higher number of active MJO days in the Indian and West Pacific Ocean. These findings are consistent with MJO activity observations of the present and past.

The second half of this thesis discusses the implementation of assimilation methodologies in physical oceanography. It presents the mathematical recipe of the assimilation method adapted in the present study and also illustrates the implementation of assimilation of observed data over the oceans in a regional ocean model (ROMS) in the Southeast Pacific region. Fifteen-day ROMS I4D-VAR data assimilation fits are performed successfully. The normalized absolute misfit between the observations and the corresponding model states is reduced close to the observational error range. Eddies are identified from the ocean state estimate along the track of the VOCALS-Rex cruise of 2008 and studied for their hydrography and velocity structure. Cyclonic eddies (sea level anomaly lows) are characterized by shoaling isopycnals in the upper 300 m, colder temperature cores and a shallower salinity minima. It is also observed that the water mass properties of the core of the eddy has similar properties to that in the subantarctic water close to the coast. A heat budget analysis for the period of the cruise reveals that the advection is the predominant process that balances the surface heat flux and temperature tendency. Vertical diffusion is the second highest term balancing the heat budget with the horizontal diffusion being an order of magnitude smaller.

Lastly, the role of the linear analysis step of the ensemble Kalman filters

(EnKF) in disrupting the balanced dynamics in a simple atmospheric model is investigated and compared to a fully nonlinear particle-based filter (PF). Identical twin experiments show that EnKF and PF capture the variables on the slow manifold well as the dynamics is very stable. PFs, especially the SKRF, capture slaved modes better than the EnKF implying a full Bayesian analysis estimates the nonlinear model variables better. The PFs perform significantly better in the fully coupled nonlinear model where fast and slow variables modulate each other. This suggests that the analysis step in the PFs maintains the balance in both variables much better than the EnKF.

Chapter 1

Prolegomenon

This chapter serves as an introduction to the thesis. The purpose is to motivate the discussion on the advances in ocean-atmosphere general circulation modeling and the data assimilation problem. Specifically, it focuses on modeling the Madden-Julian Oscillation in a climate model and modeling mesoscale eddies in a regional ocean model with data assimilation. It introduces in broad brush-strokes, a picture of the development in climate modeling, regional ocean modeling and data assimilation fields of research and their main motivations. It illustrates the objectives of combining fully complex ocean general circulation models (OGCM) and oceanographic data. It also depicts the difficulties in modeling the Madden-Julian Oscillation and improvements achieved by a state-of-the-art climate system model. An overview of these problems studied in this thesis is presented. This chapter also has a road-map of the thesis, which should serve as a reader's guide.

1.1   Background

THE earth is the only place in the universe known by humankind that supports life. Covered by a thin blanket of air, a thinner film of water and a thin veneer of soil, the three combine to support a web of life of wondrous diversity and continual change. The unique characteristics of the earth in order for it to support life is its climate. The very fine balance of the

Earths climate provides just the necessary condition required to support life. The impact of a changing climate on such a fine balance could be profound. Hence, an indepth study of the climate system and its component subsystems is essential for humans to find a roadmap for sustaining the diverse life forms on this planet without spoiling its fine balance.

Since ancient times, humans have been trying to satisfy their curiosity about earth's climate by studying various aspects of it. Here is a brief history of man's study of earth's climate and weather. The Babylonians studied cloud patterns to predict the weather in the 6th century B. C.. The Greek philosopher Aristotle described weather patterns in *Meteorologica*. Theophrastus, one of Aristotle's student, published the Book of Signs which dealt with weather forecasting. The ancient civilizations of China and India also included different approaches to weather prediction extending from astronomy to studying the changes in animal behavior during different weather.

The greatest minds of the Renaissance were also intrigued by the possibility of weather prediction. The thermometer was invented by Galileo Galilei in the 16th century, and a mercury barometer was invented by Evangelista Torricelli in the 17th century. These were the first few steps taken to make quantitative observations of weather and study Earth's atmosphere scientifically, especially its weather and climate. Modern weather forecasting methods began with the invention of the electric telegraph in 1835. The telegraph facilitated an instantaneous collection of observations of weather conditions from a larger area than ever before.

Great progress was made in the science of meteorology during the 20th century. The possibility of numerical weather prediction was proposed by Lewis Fry Richardson in 1922, (Lynch, 2006) though computers did not exist to complete the vast number of calculations required to produce a forecast before the event had occurred. The first computerized weather forecast was performed by a team led by the mathematician John von Neumann.

Jules Charney, John von Neumann, Eliassen and Smagorinsky pioneered the field of numerical weather prediction, which was the first foray into a computational framework of weather and climate studies. As a natural extension to Jules

Charney's work, Norman Philips completed in mid-1955, his monumental general circulation experiment [N. Philips, 1960]. Despite the simplicity of the model he used, the results were remarkable in their ability to reproduce the salient features of the general circulation. With this, he began a new era in mankind's quest to understand the earth's climate system. The ensuing five decades have seen a revolutionary change in both the fields of computers and the field of computational modeling of earth's weather and climate.

1.1.1 General circulation models

General Circulation Model (GCM) is a mathematical model of the general circulation of the atmosphere or ocean and is based on the Navier-Stokes equations on a sphere along with the thermodynamic terms for various energy sources. The solution of a series of equations that describe the movement of energy, momentum and various tracers (e.g. water vapor in the atmosphere and salt in the oceans) and the conservation of mass is therefore satisfied by these equations. The accuracy of the model partly depends on the spatial resolution of the grid points and the length of the timestep. A compromise must be made between the resolution desired, the length of integration and the computational facilities available. A climate model must be a simplification of the real world since there are several complex climate processes that are yet to be understood, and also many of the feedbacks between the climate processes are computationally very intensive and challenging. The dynamics in the earth's atmosphere-ocean system ranges in length and time from micro to climate timescales as shown in Figure 1.1

1.1.2 Present challenges in climate modeling

The complexity of earth's climate system presents a challenge to climate theory. Today we try to simulate the climate by capturing as much of the dynamics as we can in comprehensive numerical models. We also try to understand the climate using observations and idealized models. As our comprehensive models improve, they more and more become the primary tools by which theory confronts

observations. The study of global warming is an especially good example of this trend. A handful of major modeling centers around the world compete in creating the most convincing climate simulations and the most reliable forecasts of climate change, while large observational efforts are mounted with the stated goal of improving these comprehensive models.

The complex system of earth's climate is associated with a wide range of physical, biological and chemical feedbacks which together occur in a continuum of temporal and spatial variability. The traditional boundaries of weather, seasonal prediction, regional and global climate are strictly artificial. The scale interactions between the large-scale climate and the microscale to mesoscale processes that govern weather and regional climate cannot be treated as independent phenomena.

Today's global coupled climate system models take into account the whole climate system (Figure 1.2). The accurate representation of the continuum of variability in numerical models is a challenging but essential goal. For example, the effects of changes in deep ocean stratification will play an important role in the change of earth's climate averaged over decades to centuries, while local changes in windstress or solar forcing may not play a role at these timescales. Yet, on timescales shorter than a season, the relative importance could be reversed.

In the equatorial troposphere, the Madden-Julian Oscillation is a planetary scale wave envelope of complex multiscale convection. The Madden-Julian Oscillation (MJO) has long been an aspect of the global climate that has provided a challenging test for the climate modeling community. There have been numerous studies of simulation of the MJO and boreal summer intraseasonal variability (BSISV) in general circulation models (GCMs), since the 1980s, ranging from Hayashi and Golder (1986, 1988); Lau and Lau (1986), through to more recent studies by Zhang et al. (2006b); Sperber and Annamalai (2008b); Kim et al. (2009b). Over the past two decades developments in our understanding of what the MJO is and what drives it have parallelled attempts to reproduce the MJO in climate models. In fact, many advances in understanding the MJO have come through modeling studies. In particular, the failure of climate models to simulate various aspects of the MJO has prompted investigations into the mechanisms that

are important to its initiation and maintenance, leading to improvements both in our understanding of, and ability to simulate, the MJO.

Chapters 2 and 3 of this thesis present results from the analysis of an improved Madden Julian Oscillation simulation using the new Community Climate System Model version 4 (CCSM-4). Most GCMs still suffer from poor simulations of the MJO. There have been many improvements in the simulations of the MJO over the last decade. Yet it is still a mystery why most climate models have a difficult time simulating a realistic MJO or forecasting one. Only recently has the link between MJO simulations and convection parameterization been explored. (Zhou et al., 2011b; Kim et al., 2009b).

We assess the ability of the Community Climate System Model-4 (CCSM-4) to represent the Madden Julian Oscillation, the dominant form of intraseasonal variability in the tropical atmosphere. We use the US CLIVAR MJO Working Group prescribed diagnostic tests to evaluate the models mean state, variance and wavenumber-frequency characteristics in a 20-year simulation of the intraseasonal variability in zonal winds at 850 hPa (U850) and 200 hPa (U200) and Outgoing Longwave Radiation (OLR). While most climate models today fail to simulate even the large-scale features of the MJO, we find that CCSM4 reproduces many realistic aspects of MJO behavior.

The mesoscale variability is the dominant signal in the global ocean circulation variability. The advent of satellite oceanography in the 1970s revealed the ubiquity of the so-called mesoscale phenomena (gyres, eddies, jets, fronts, meanders) in the world's oceans. This discovery triggered observational and modeling efforts that have shown the mesoscale to be a very important component of dynamical oceanography at all scales (e.g. in transporting momentum, heat, mass, energy, chemical and biological properties). Thus, resolving the mesoscale variability is crucial to correctly understand the dynamics of the ocean circulation and to estimate the associated heat transport, even at climatic scales (Stammer and Wunsch, 1999).

Mesoscale dynamics encompasses oceanic phenomena with a horizontal scale ranging approximately from 10 to 100 km and an associated time scale of

a few days. The mesoscale phenomena from the dynamical perspective concerns processes with timescales ranging from the buoyancy oscillation ($2\pi/N$, where N is the buoyancy (Brunt-Vaisala) frequency) to a pendulum day ($2\pi/f$, where f is the Coriolis parameter), encompassing mesoscale eddies and the full spectrum of inertia-gravity waves but stopping short of synoptic-scale phenomena which have Rossby numbers less than 1 in atmospheric dynamics.

Chapters 4 and 5 of this thesis focus on studying mesoscale eddies in the upwelling regions along the west coast of South America. These eddies affect the distribution of sea-surface temperature (SST) in the South East Pacific (SEP) in two major ways. Eddy heat fluxes drive SST changes that affect the atmospheric boundary layer (ABL) by altering its stability and consequent heat, momentum and moisture fluxes at the air-sea interface. Eddies also affect nutrient transport, which controls ocean biology. The main focus of this research is aligned with one of the scientific goals of VAMOS [1] Ocean Cloud Atmosphere Land Study-Regional Experiment(VOCALS-REx). VOCALS is an international CLIVAR program, the major goal of which is to develop and promote scientific activities leading to improved understanding of the South East Pacific (SEP) coupled ocean-atmosphere-land system on diurnal to inter-annual timescales.

The dynamics of mesoscale ocean eddies during an observational campaign in November 2008 in the SEP region will be explored in this modeling and data assimilation study that will aid in the diagnosis of the VOCALS-REx observations. Observed mesoscale oceanic surveys of the VOCALS campaign will be used in data assimilation experiments to diagnose the dynamics and sensitivities of the ocean circulation fields. Data assimilation fits of the VOCALS hydrographic surveys (and concomitant data) will provide crucial dynamically consistent diagnostics of the circulation for interpreting the relation between physical variables, atmospheric variables and biology. Most ocean models still suffer from a poor simulation of the ocean eddy field. Although there have been improvements in the simulations of ocean eddies over the last decade, it is still unknown why most numerical models

---

[1] VAMOS is the Variability of the American Monsoon Systems, which is a CLImate VARiability Working Group (CLIVAR) multidisciplinary international program that addresses monsoonal flows over both North and South America.

have a difficult time simulating ocean eddies realistically. Only recently has the link between ocean mesoscale modeling and data assimilation been explored (De Mey, 1997; Powell et al., 2008, 2009; Moore et al., 2011; Song, 2011).

Eddies in the SEP form near the coasts and propagate westward, resulting in narrow bands of high eddy kinetic energy (EKE) in the coastal region and a broader, weaker EKE tongue stretching out beyond 90° W in the offshore region (Chaigneau and Pizarro, 2005; Johnson and McTaggart, 2010). The hydrographic and velocity structures of cyclonic and anticyclonic eddies in the SEP are first characterized using data from VOCALS-REx, an extensive field campaign that surveyed upper-ocean and atmospheric properties in the SEP (Wood et al., 2011). Cyclonic eddies were associated with cooler surface temperatures than the mean conditions, whereas anticyclonic eddies were associated with warmer surface temperatures. The mean temperature signals were of opposite sign but equal magnitude for each type of eddy.

1.1.3   Limitations in modeling scale interactions

One of the primary simplifications in global circulation models (GCMs) is the resolution of the model in both time and space. Although the sole reason for this simplification is our limitations in computational resources, too fine a resolution may be inappropriate because processes acting on a smaller scale than the model is designed to resolve may be inadvertently incorporated. The climate research community is beginning to use higher-resolution models that are mesoscale-process permitting. Much research has to be done to reformulate parameterizations for the subgrid scale processes in these higher resolution models. Current parameterization schemes do not adequately handle the mesoscale organization of convection, which is a critical missing link in scale interaction process. The limited representation of convection and cloud processes is likely a major factor in the inadequate simulation of tropical oscillations, primarily the challenge in modeling Madden Julian Oscillations well in any present-day climate models (Slingo et al., 1996b).

Another scale interaction problem is the challenge in modeling the sub-

tropical eastern boundary regimes off the coasts of southwest Africa, Peru-Chile, and Baja-southern California. These regimes are marked by marine stratus, equatorward alongshore winds, and ocean upwelling. Large and Danabasoglu (2006) suggest that a better resolution of these features improves both the regional climate and also the large-scale climate system reducing rainfall biases across the tropical oceans (Figure 1.3, First figure from Dai (2006)).

Other examples of limitations of today's climate models in modeling scale interactions include modeling the Asian summer monsoon which is influenced by steep topographical gradients, mesoscale processes and mesoscale convective complexes. Clearly, addressing these errors is critical to climate prediction at all time scales.

Two of these many problems with today's climate models are addressed in this thesis. The first third of the thesis presents improvements achieved in modeling Madden Julian Oscillations in a state-of-the-art climate model of present day, the Community Climate System Model version 4 (CCSM-4). The second third of the thesis illustrates an experiment in ocean modeling and data assimilation of oceanic mesoscale eddies in the South East Pacific region. The last third of the thesis is a presentation of results from a data assimilation experiment in a simplified geophysical fluid dynamics model to show the importance of preserving balance during data assimilation which remains a challenging problem in today's assimilation models for GCMs.

1.2   Objectives of this dissertation

One can see from the above discussions that the modeling of the MJO in a climate model and ocean eddies in an ocean model realistically are challenges still being tackled by today's state-of-the-art ocean-atmosphere circulation models. In this context, this dissertation aims at improving our understanding and capability to simulate mesoscale and synoptic scale motions in the atmosphere and ocean. Specifically it documents an effort to model mesoscale eddies realistically in a regional ocean model with data assimilation. It also presents improvements in

modeling the MJO in CCSM4 more coherently than achieved in the previous version of CCSM. The last section in this thesis is the presentation of results from an experiment showing the benefits of nonlinear data assimilation methods over using a linear-based data assimilation method in a simplified geophysical dynamical model.

The objectives of this dissertation are threefold:

The first primary objective of this thesis is to present results from the assessment of the Community Climate System Model-4 (CCSM- 4) to represent the Madden Julian Oscillation, the dominant form of intraseasonal variability in the tropical atmosphere. The US CLIVAR MJO Working Group prescribed diagnostic tests is used to evaluate the models mean state, variance and wavenumber-frequency characteristics in a 20-year simulation of the intraseasonal variability in zonal winds at 850 hPa (U850) and 200 hPa (U200) and Outgoing Longwave Radiation (OLR). While most climate models today fail to simulate even the large-scale features of the MJO, we find that CCSM4 reproduces many realistic aspects of MJO behavior.

A second primary goal of this thesis is to better understand the structure and properties of eddies and the processes contributing to the ocean heat budget in establishing the SST distribution in the Southeast Pacific region. The climate of the Southeast Pacific (SEP) involves important feedbacks between atmospheric circulation, sea-surface temperature (SST), clouds, ocean heat transport, aerosols, and coastal orography, bathymetry and geometry (Ma et al., 1996a). The equator-ward Peru-Humboldt Current is a geostrophic flow that is baroclinically unstable and develops nonlinear mesoscale eddies that extend the current system far off-shore through squirts, jets, filaments, and westward Rossby wave propagation. The eddies result in exchanges of heat, salt, momentum and nutrients that balance the upwelling water and the local air-sea fluxes. A central goal of the second study in this thesis is to assimilate the VOCALS-Rex enhanced observations into a regional ocean model of the region and characterize the hydrographic and velocity structures of cyclonic and anticyclonic eddies in the SEP during this observation campaign. Another main goal of this thesis is to better understand the regulation

of SST across the SEP, specifically during the VOCALS-REx experiment using the ocean state estimate.

The third primary objective of this thesis is to document results from an investigation of the role of the linear analysis step of the ensemble Kalman filters (EnKF) in disrupting the balanced dynamics in a simple atmospheric model and compare it to a fully nonlinear particle-based filter (PF). The filters have a very similar forecast step but the analysis step of the PF solves the full Bayesian filtering problem while the EnKF analysis only applies to Gaussian distributions. We compare the EnKF to two flavors of the particle filter with different sampling strategies, the Sequential Importance Resampling Filter (SIRF) and the Sequential Kernel Resampling Filter (SKRF). The model admits a chaotic vortical mode coupled to a comparatively fast gravity wave mode. Identical twin experiments show that EnKF and PF capture the variables on the slow manifold well as the dynamics are very stable. The PFs perform significantly better in the fully coupled nonlinear model where fast and slow variables modulate each other.

1.3   Summary of results

MJO in CCSM4

CCSM4 produces coherent, broadbanded and energetic patterns in eastward propagating intraseasonal zonal winds and OLR in the tropical Indian and Pacific Oceans that are generally consistent with MJO characteristics. Broadscale patterns, as revealed in combined EOFs of U850, U200 and OLR, are remarkably consistent with observations and indicate that convective coupling occurs in the simulated MJOs.

MJO and Earth's Climate

A tendency for MJO to be more energetic during weak warm ENSO conditions, negative Monsoon Hadley flow, and positive zonal shear, was noted. A model simulation of a global warming scenario reveals that an increase in Tropi-

cal temperatures leads to an increase in the number of days with higher amplitude MJOs and also a higher number of active MJO days in the Indian and West Pacific ocean.

ROMS data assimilation in the Southeast Pacific

The 15-day ROMS I4D-VAR simulations successfully improve the state estimation of the Southeast Pacific ocean mesoscale eddies by adjusting the initial conditions and the surface forcing. The normalized absolute misfit between the observations and the corresponding model states is reduced close to the observational error range. Other statistical measures comparing model with observations are also improved.

Eddies and heat budget in the Southeast Pacific

Eddies are identified from the ocean state estimate along the track of the VOCALS-Rex cruise of 2008 and studied for their hydrography and velocity structure. A cyclonic eddy (sea level anomaly low) is characterized by shoaling isopycnals in the upper 300 m, colder temperature cores and a shallower salinity minima. The cyclonic eddy was observed to have a subsurface velocity core diameter of about 50 km, as well as a cooler, salty core at a depth of about 150 m.

Measurements and analyses show a mean net warming heat flux from the atmosphere to the ocean of 40-80 W m^{-2} over a wide cross-shore swath in the Southeast Pacific, and this warming has to be compensated by cooling since this region has one of the coldest temperatures at comparable latitudes around the globe. A heat budget analysis for the period of the cruise reveals that the advection is the predominant process that balances the surface heat flux and temperature tendency. Vertical diffusion is the second highest term balancing the heat budget with the horizontal diffusion being an order of magnitude smaller.

Balanced dynamics in a linear vs nonlinear filter

Ensemble Kalman Filter (EnKF) and Particle Filters (PFs) (explained in the next section) capture the variables on the slow manifold of the Lorenz-86

mode well as the dynamics is very stable. PFs, especially the SKRF, capture slaved modes better than the EnKF implying a full Bayesian analysis estimates the nonlinear model variables better. The PFs perform significantly better in the fully coupled nonlinear model where fast and slow variables modulate each other. This suggests that the analysis step in the PFs maintain the balance in both variables much better than the EnKF. It is also shown that increasing the ensemble size generally improves the performance of the PFs but has less impact on the EnKF after a sufficient number of members has been used.

1.4 Essentials

What is the MJO?

The Madden-Julian Oscillation (MJO) is the dominant form of intraseasonal variability in the tropical atmosphere. Typically, their region of genesis is over the western Tropical Indian Ocean and remain pronounced over the eastern Indian Ocean and the western Pacific Ocean as they propagate eastward (Figure 1.4). The MJO is characterized by large-scale, eastward-propagating, equatorially-trapped, baroclinic oscillations in the tropical wind field (Madden and Julian, 1971b, 1994b). Over the warmest tropical waters, in the Indian and west Pacific Ocean, there is considerable interaction between these wind field oscillations and anomalies in atmospheric deep convection. In these regions, where the convective coupling is strong, the oscillation propagates rather slowly, about 5-10 m/s. Several studies suggest that the MJO propagates slowly during its convective phase due to a coupling between Kelvin and Rossby waves brought about by the strong latent heating (Wang and Rui, 1990; Salby et al., 1994) as well as a tighter coupling to the underlying warm SST (Flatau et al., 1997; Wang and Xie, 1997; Waliser and Lau, 1999). Once the disturbances reach the vicinity of the dateline, and thus cooler equatorial waters, the convection subsides and the disturbances behave much like a damped Kelvin wave with a faster propagation speed, about 15-20 m/s (Hendon and Salby, 1994). The above characteristics are most strongly exhibited during

the boreal winter and spring when the Indo-Pacific warm pool is centered near the equator. In addition to this eastward-moving, equatorially-trapped form of tropical intraseasonal variability (TISV), the other most prolific form propagates northeastward from the equatorial Indian Ocean into Southeast Asia during the northern hemisphere summer (Wang and Xie, 1997; Wang and Rui, 1990).

What is VOCALS?

The VAMOS Ocean-Cloud-Atmosphere-Land Study (VOCALS) is an international CLIVAR program. The major goal of VOCALS is to develop and promote scientific activities leading to improved understanding of the Southeast Pacific (SEP) coupled ocean-atmosphere-land system on diurnal to inter-annual timescales (Figure 1.5). One of the principal program objectives is the elimination of systematic errors in the region of coupled atmospheric-ocean general circulation models, and improved model simulations and predictions of the coupled climate in the SEP and global impacts of the system variability.

What are ocean mesoscale eddies?

Mesoscale eddies occur when there is a balance of two major forces - one is a horizontal pressure gradient force arising from differences in water density and the other is an "apparent" force associated with the Earths rotation. This is called the Coriolis force. Eddies occur virtually everywhere in the ocean, including Arctic regions and even off the coast of Antarctica in the Southern Hemisphere. But, there is a twist - the Coriolis effect causes cold-core eddies in the southern hemisphere to rotate clockwise (cyclonic) and warm-core eddies rotate counterclockwise (anti-cyclonic). The size of eddies and rings vary as do their lifetimes - a month or so to more than a year, with an average of a few months. The largest scale eddies are caused due to instabilities of strong horizontal sheared motions, particularly in western boundary currents, and they are important in shaping the pathways and intensity of the most intense ocean currents. These eddies often take the form of well defined rings extending to great depth. At slightly smaller scales, of order tens of kilometers, eddies are generated by the slumping of horizontal density

gradients. These baroclinic eddies with strongly rotating flows and are important in the movement of watermasses from near the surface into the ocean interior and for the dynamical balance governing some of the major ocean currents such as, the Antarctic Circumpolar Current.

What is the Ensemble Kalman Filter?

The Ensemble Kalman Filter (EnKF) is a Monte Carlo implementation of the Bayesian update problem: Given a probability density function (pdf) of the state of the modeled system (the prior, called often the forecast in geosciences) and the data likelihood, the Bayes theorem is used to obtain the pdf after the data likelihood has been taken into account (the posterior, often called the analysis). This is called a Bayesian update. The Bayesian update is combined with advancing the model in time, incorporating new data from time to time.

The basic idea behind this filter is to combine the optimal forecast step of the PF with a KF correction of the particles. The weights are then kept uniform. The algorithm of the EnKF can be summarized as follows:

- *Prediction step*: As in the PF, the analyzed particles, $\boldsymbol{x}_{k-1}^{a,i}$ are advanced in time with the model to compute the forecast particles $\boldsymbol{x}_k^{f,i}$.

- *Correction step*: A KF correction step is applied to every forecast particle as

$$\boldsymbol{x}_k^{a,i} \;=\; \boldsymbol{x}_k^{f,i} + \mathbf{G}_k^e \big(\boldsymbol{y}_k^i - \boldsymbol{H}_k(\boldsymbol{x}_k^{f,i})\big). \tag{1.1}$$

The gain matrix $\mathbf{G}_k^e$ is the same as the Kalman gain but is computed from the sample covariance matrix of the $\boldsymbol{x}_k^{f,i}$ as described by (Evensen, 2003)

In Eq. (6.7), the observation was assigned a superscript index associated with each particle. This is because the observation needs to be perturbed by noise sampled from the *PDF* of the observational error (Burgers et al., 1998).

The correction step of the EnKF uses only the first two moments of the particle ensemble and is thus suboptimal for non-Gaussian systems. In practical

situations, however, the EnKF was found to be more robust than the PF when small-size ensembles were used because the Kalman update of the particles is applied using the forecast error covariance matrices estimated from the particle ensemble. This made the implementation of the Bayesian filtering feasible with high dimensional systems, as in meteorology and oceanography. The KF correction reduces the collapse of the ensemble by 'pulling' the particles toward the true state of the system, allowing the filter to operate with a reasonable number of particles (Kivman, 2003; Hoteit et al., 2008; Van Leeuwen, 2009). With large enough ensembles, however, the PF was shown to outperform the EnKF (Nakano et al., 2007; Jardak et al., 2010).

What is the Particle Filter?

The PF provides a discrete solution of the Bayesian filtering problem using point-mass representations $\sum_{i=1}^{N} w_i \delta_{\boldsymbol{x}^i}$, of the state *PDFs* (Doucet et al., 2000). The vectors $\boldsymbol{x}^i$ are called particles and the w_i are their associated weights. N is the number of particles (or the size of the ensemble). After a forecast or analysis step, the minimum variance estimate of the system state is then obtained as the weighted-average of the ensemble $\sum_{i=1}^{N} w^i \boldsymbol{x}^i$. Starting from an initial ensemble of particles $\boldsymbol{x}_0^i, i = 1, \ldots, N$, the PF algorithm consists of a prediction step to integrate the particles in time and a correction step to update the weights as follows:

- *Prediction step*: At time t_{k-1}, the particles $\boldsymbol{x}_{k-1}^i$ are integrated forward with the model to the time of the next available observation t_k.

- *Correction step*:: The new observation is used to update the weights with

$$w_k^i = \frac{1}{c_k} w_{k-1}^i \phi \left(\boldsymbol{y}_k - \boldsymbol{H}_k(\boldsymbol{x}_k^i); \mathbf{R}_k \right), \qquad (1.2)$$

where c_k is a constant normalizing the total weight. The particles remain unchanged. Thus a particle receives more/less weight proportional to its distance from the most recent observation normalized by the observational error covariance matrix $\mathbf{R}_k$.

1.5   A reader's guide to the thesis

Chapter 2 investigates the nature of the Madden-Julian Oscillation simulated in the current version of the Community Climate System Model version 4. We use the US CLIVAR MJO Working Group prescribed diagnostic tests to evaluate the models mean state, variance and wavenumber-frequency characteristics in a 20-year simulation of the intraseasonal variability in zonal winds at 850 hPa (U850) and 200 hPa (U200) and Outgoing Longwave Radiation (OLR). While most climate models today fail to simulate even the large-scale features of the MJO, we find that CCSM4 reproduces many realistic aspects of MJO behavior.

Chapter 3 considers the relations between MJO in the model and its concurrence with other climate states. Higher amplitude MJO activity occurs during weak warm ENSO events and during periods of weak meridional shear and negative zonal shear during the Indian Monsoons. MJO response to anthropogenic climate change is assessed using CCSM4. The 20th century ensemble is compared with the 21st century projection for a 8.5 W/m^{-2} forcing scenario by the end of 21st century. Observations suggest that warming in the tropical Indian and Pacific Oceans in recent decades may have contributed to increased trends in the annual number of MJO events.

Chapter 4 builds the background for the second half of this thesis and discusses the development of assimilation methodologies in physical oceanography. It presents the mathematical recipe of the assimilation method adapted in the present study and also illustrates the implementation of assimilation of observed data over the oceans in a general circulation ocean model (ROMS) for the Peruvian Current system. Mesoscale eddies generated in the upwelling regions in the South East Pacific are studied. Data assimilation of the sea state observations from satellites and ships for a period of a month in 2008 is achieved. The one-month ROMS I4D-VAR simulations successfully improve the state estimation by adjusting the initial conditions and the surface forcing. The normalized absolute misfit between the observations and the corresponding model states is reduced close to the observational error range. Other statistical measures comparing model with observations are also improved.

Chapter 5 presents results from the diagnosis of the ocean state achieved from the data assimilation experiment. Eddies are identified from the ocean state estimate along the track of the VOCALS-Rex cruise and studied for their properties and structure. Structure and properties of the measured eddy and also a heat budget analysis of the upper ocean during the cruise period is presented.

Chapter 6 investigates the role of the linear analysis step of the ensemble Kalman filters (EnKF) in disrupting the balanced dynamics in a simple atmospheric model and compare it to a fully nonlinear particle-based filter (PF). The filters have a very similar forecast step but the analysis step of the PF solves the full Bayesian filtering problem while the EnKF analysis only applies to Gaussian distributions. We compare the EnKF to two flavors of the particle filter with different sampling strategies, the Sequential Importance Resampling Filter (SIRF) and the Sequential Kernel Resampling Filter (SKRF). The PFs perform significantly better in the fully coupled nonlinear model where fast and slow variables modulate each other. This suggests that the analysis step in the PFs maintain the balance in both variables much better than the EnKF. It is also shown that increasing the ensemble size generally improves the performance of the PFs but has less impact on the EnKF after a sufficient number of members has been used.
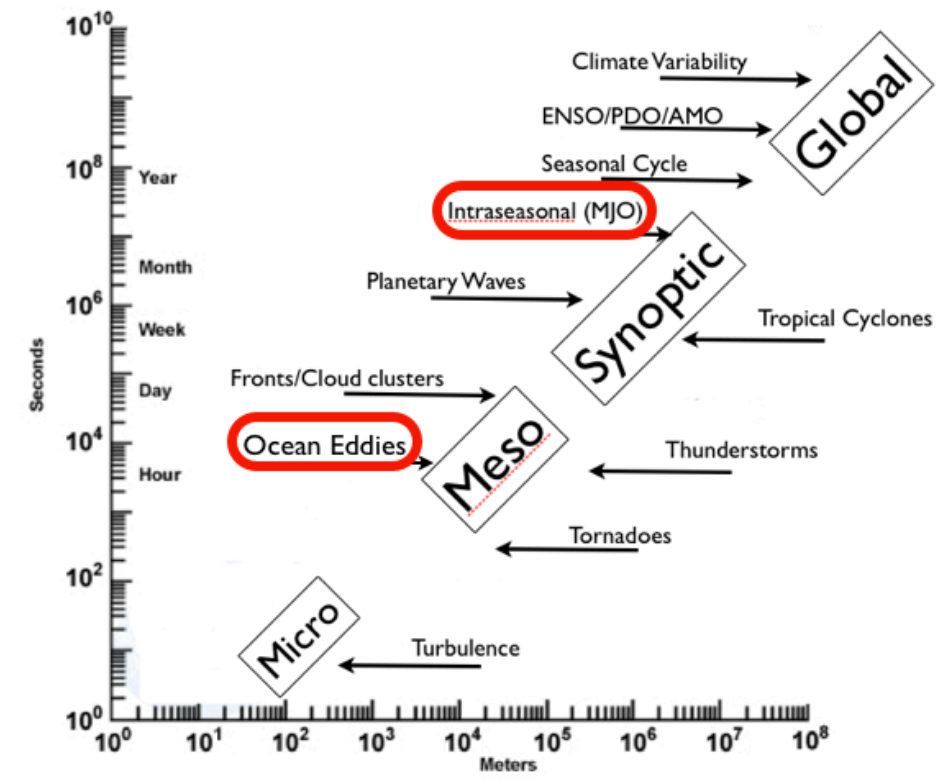
Figure 1.1: Scales of motion across time and space that exist and interact in the global climate system
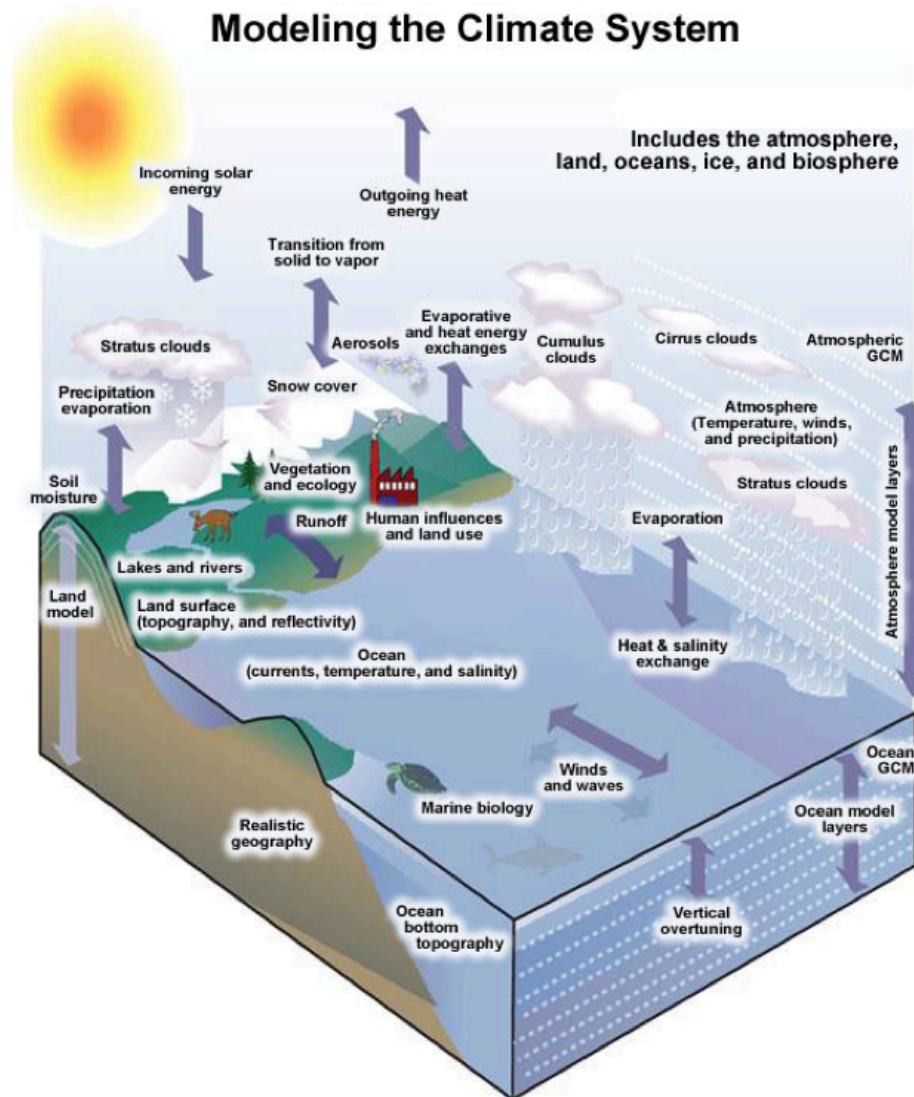
Figure 1.2: Schematic of the various processes involved in the Global Climate System (Source: `http://www.meted.ucar.edu/tropical/textbook_2nd_edition/` `media/graphics/climate_sys_ncdc.jpg`)
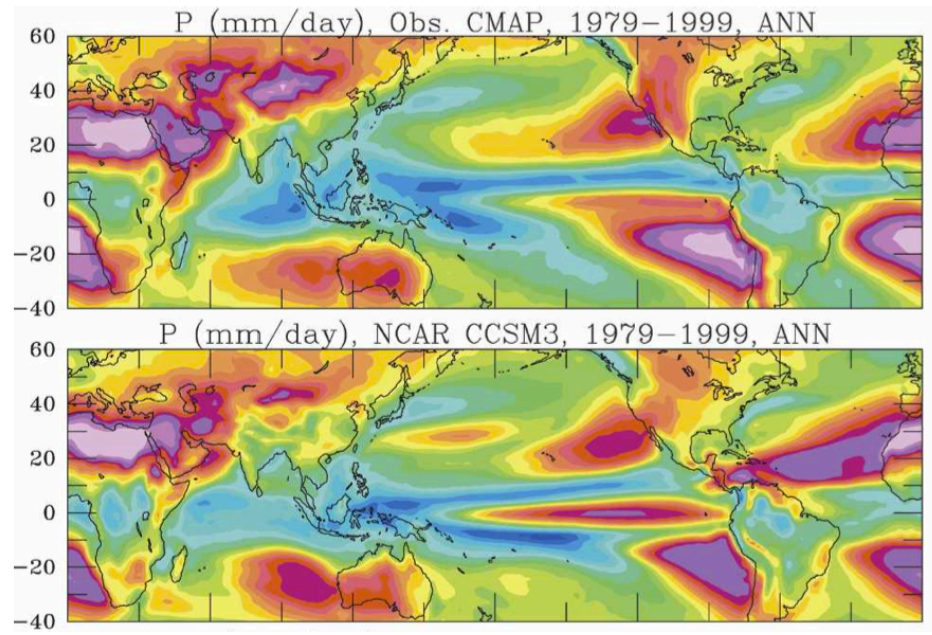
Figure 1.3: 1979-99 mean annual precipitation from observations (CMAP; Xie and Arkin 1997) and twentieth-century climate simulations by CCSM3 coupled climate model.(Dai, 2006)
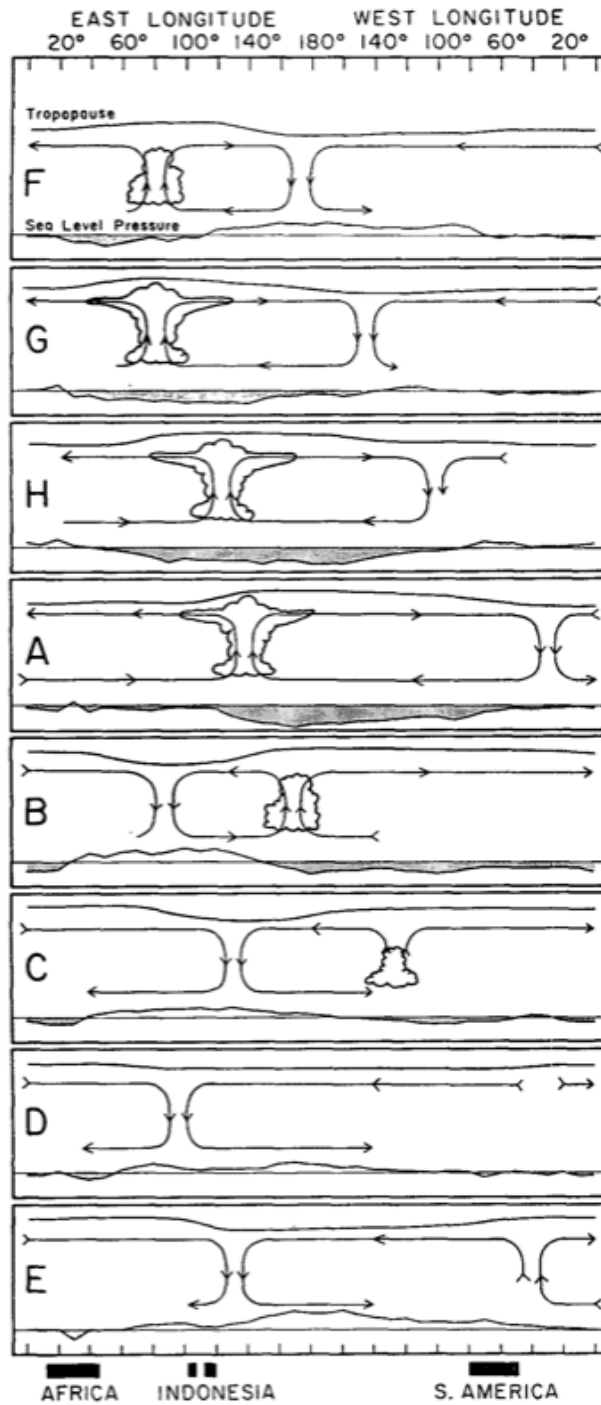
Figure 1.4: Schematic of different development stages of the MJO along the equator. Cloud symbols indicate the center of deep convective activity, and arrows represent zonal circulations, and curves above and below cloud symbols signify tropopause height and sea-level pressure perturbations, respectively. (Taken from Madden and Julian 1972a.)
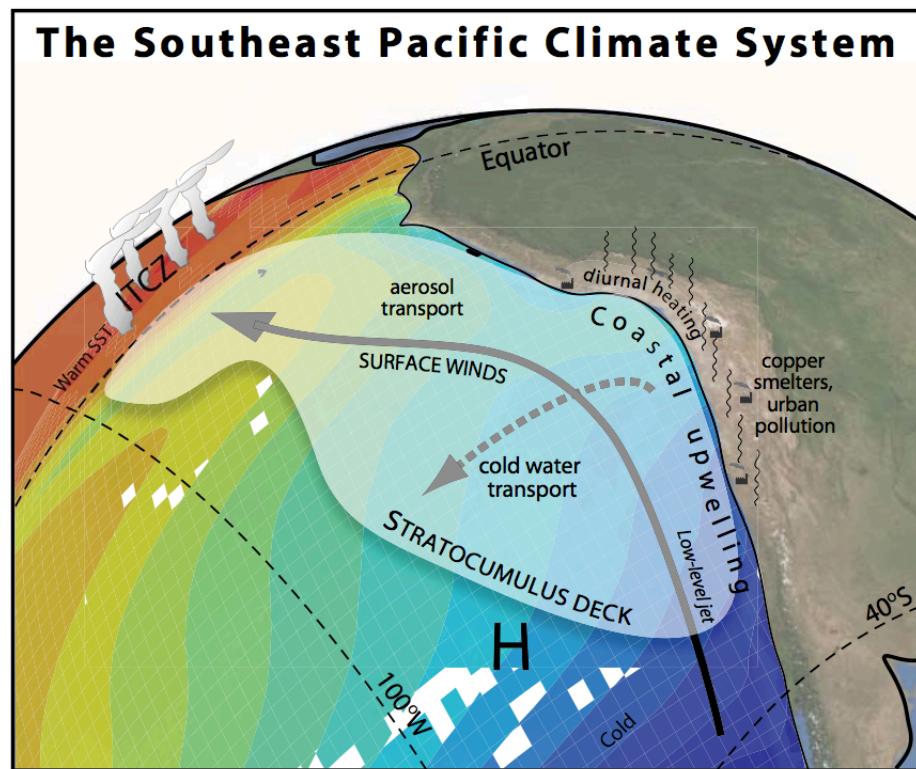
Figure 1.5: Key features of the southeast Pacific (SEP) coupled climate system being explored in the VOCALS Program.(Taken from Wood et al., 2011)

Chapter 2

The Madden Julian Oscillation in CCSM4

We assess the ability of the Community Climate System Model-4 (CCSM-4) to represent the Madden Julian Oscillation, the dominant form of intraseasonal variability in the tropical atmosphere. We use the US CLIVAR MJO Working Group prescribed diagnostic tests to evaluate the model's mean state, variance and wavenumber-frequency characteristics in a 20-year simulation of the intraseasonal variability in zonal winds at 850 hPa (U850) and 200 hPa (U200) and Outgoing Longwave Radiation (OLR). While most climate models today fail to simulate even the large-scale features of the MJO, we find that CCSM4 reproduces many realistic aspects of MJO behavior. CCSM4 produces coherent, broadbanded and energetic patterns in eastward propagating intraseasonal zonal winds and OLR in the tropical Indian and Pacific Oceans that are generally consistent with MJO characteristics. Strong peaks occur in coherence spectra with periods between 20-100 days and zonal wavenumbers between 1 and 3. Model MJO's, however, tend to be more broadbanded in frequency than in observations, with higher frequencies being associated with zonal wavenumbers in the MJO band. But broadscale patterns, as revealed in combined EOFs of U850, U200 and OLR, are remarkably consistent with observations and indicate that convective coupling occurs in the simulated MJOs.

2.1 Introduction

Four decades have passed since Madden and Julian made the pioneering discovery of a 40-50 day oscillation in the zonal winds in the tropics Madden and Julian (1971a, 1972). This discovery has led to numerous studies into a phenomenon now aptly called the Madden-Julian Oscillation (MJO). Although MJO dynamics are still not fully understood (Madden and Julian, 1994a; Zhang, 2005a), MJOs are known to interact with a panoply of climate phenomena across different spatial and temporal scales. Examples of MJO interactions with some of these phenomena include its feedbacks with El Niño events (e.g., Marshall et al., 2009; Hendon et al., 2007; Zavala-Garay et al., 2005; Bergman et al., 2001; Kessler, 2001; Takayabu et al., 1999), its feedbacks with the North Atlantic Oscillation (Cassou, 2008), its impact on the onset and break of the Indian and Australian summer monsoons (e.g., Yasunari, 1979; Wheeler and McBride, 2004), its impact on the formation of tropical cyclones (e.g., Liebmann et al., 1994; Maloney and Hartmann, 2000a,b) and its impact on the mean climate state (Sardeshmukh and Sura, 2007). Practically, studying these various climate phenomena, modeling them and being able to predict these climate events would be impossible without understanding and simulating MJOs accurately in models.

In order to fully understand these important components of earth's climate we need a better knowledge of how MJOs interact with these components at various temporal and spatial scales (Lau and Waliser, 2005a). Yet current climate models still have difficulty representing MJOs realistically. Numerous multi-model inter-comparison studies of their ability to capture MJOs have been published (Slingo et al., 1996a; Waliser et al., 2003; Lin et al., 2006a; Zhang et al., 2006a; Sperber and Annamalai, 2008a; Kim et al., 2009a) revealing how GCMs continue to struggle to represent MJOs.

Slingo et al. (1996a) have shown in their study of the tropical intraseasonal variability using atmospheric GCM simulations forced by observed monthly mean sea surface temperature (SST) that the Atmospheric Model Intercomparison Project (AMIP) models were unable to simulate the observed spectral peak in the 30-70 day period band of the global (zonal wavenumber 1) equatorial 200-hPa

velocity potential. In another paper, Lin et al. (2006a) analyzed MJO variability in 14 Coupled Model Intercomparison Project-3 (CMIP3) models elucidating that only two models had MJO variance comparable to observations but that many other MJO features were lacking realism. Kim et al. (2009a) studied an improved set of global coupled models and noted that even in these models only two of them, SPCAM and ECHAM4/OPYC, yielded a respectable representation of MJO.

The aforementioned multi-model studies attempted to provide insight into what is important for MJO simulation by comparing the different physical parameterizations employed by models of differing MJO verisimilitude. A common theme throughout these studies is that good MJO representation is strongly dependent on the convection parameterization and cloud scheme employed in the model, although many other factors come into play. As established global climate models continue to be improved with better parameterizations and physics packages, they need to be validated for their performance in representing MJO variability because of its importance in influencing other climate phenomena.

Here we document how altered parameterizations in the NCAR CCSM affect resulting MJO activity in long-term climate simulations. The latest version, CCSM4, has a novel deep convective momentum transport scheme, which may profoundly alter the behavior of MJO events in the model. Our primary goal is to quantify the characteristics of MJO activity in the CCSM4 according to the set of diagnostics that has been developed to compare MJO simulations in climate models with observations (CLIVAR Madden-Julian Oscillation Working Group 2008, hereafter CL-MJOWG08; Waliser et al., 2008).

Recent work by Zhou et al. (2011a) with CCSM3 showed that MJO's were more realistic when the model included a Convective Momentum Transport term and a dilute plume approximation in the convective parameterization scheme. Inclusion of the dilute plume approximation improves the correlation between intraseasonal convective heating and intraseasonal temperature, which is critical for the buildup of the available potential energy. More realistic low-level background zonal winds over the Indo-Pacific warm pool improve the propagation speeds of intraseasonal variability in the convecting systems. We will show that MJOs are

further improved in CCSM4 compared to previous versions of CCSM studied in Kim et al. (2009a) and Zhou et al. (2011a).

Since MJO is found here to be well represented in CCSM4, we also explore its interaction with ENSO and the Indian Monsoon. Although no strong relation arises, we demonstrate that MJOs have a tendency to be more energetic during warm ENSO time periods. While this is consistent with what can be gleaned from observations on MJO variability, further analysis will be required to solidify this relationship in terms of causal linkages.

2.2   Model simulations and validation data

The CCSM is a general circulation climate model that couples the atmosphere, land, ocean, and sea ice components. Gent et al. (2010) gives an overview and a description of the CCSM version 4 climate simulation with 26 levels in the vertical, 0.9x1.25 degree horizontal atmosphere and land resolution, and nominally 1° ocean (with enhancement to 0.5 deg near the equator) and sea ice resolution. This version has numerous changes and improvements compared to version 3, as briefly documented here.

The core of the Community Atmosphere Model (CAM) version 4 has been changed from the spectral core used in CAM 3 to the Lin-Rood finite volume core (Lin, 2004). The CAM 4.0 is the sixth generation of the NCAR atmospheric GCM and has again been developed through a collaborative process of users and developers in the Atmosphere Model Working Group (AMWG). In CAM 4.0, changes to the moist physical representations center on enhancements to the existing Zhang and McFarlane (1995) deep convection parameterization.

The calculation of Convective Available Potential Energy (CAPE) assumes an entraining plume to provide the in-cloud temperature and humidity profiles used to determine buoyancy and related cloud closure properties. The modification is based on the conservation of moist entropy and mixing methods of Raymond and Blyth (1986, 1992). It replaces the standard nondilute non-entraining plume method used in CAM3 with this dilute plume approximation in order to

increase convection sensitivity to tropospheric moisture and reduce the amplitude of the diurnal cycle of precipitation over land. Sub-grid scale Convective Momentum Transports (CMT) have been added to the deep convection scheme following Richter and Rasch (2008) and the methodology of Gregory et al. (1997). CMT affects tropospheric climate mainly through changes to the Coriolis torque. These changes result in improvement of the Hadley circulation during northern Winter and it reduces many of the model biases. In an annual mean, the tropical easterly bias, subtropical westerly bias, and the excessive southern hemisphere mid-latitude jet, seen in CCSM3, are improved. In combination these modifications to the deep-convection lead to significant improvements in the phase, amplitude and spatial anomaly patterns of the modeled El Niño, as documented in Neale et al. (2008) and Zhou et al. (2011a).

There also have been a number of changes to the ocean component of CCSM4, which will be documented in (Danabasoglu et al., 2011). For the tropical air-sea interface, the only change of relevance is the use of observed background diffusivities, which significantly reduces the tropical precipitation biases (Jochum, 2009).

The NCAR CCSM4 group provided a 500-year simulation as a Control run under 1850 preindustrial conditions. Output from that run is saved as monthly means. Since MJOs have time scales comparable to that sampling, it was necessary to re-run CCSM4 and save the fields as daily means. Due to computational resource limitations, we were unable to re-run the model for the entire 500 years. Since large ENSO events may influence the development and evolution of MJO, we decided to use two extreme 10-year periods of ENSO behavior during the 500-year run, and then combine the analysis results for the two periods. One period has the maximum ENSO variance and the other has the minimum ENSO variance during the 500-year base run. We treat the two 10-year runs as independent realizations of MJO behavior and compare them jointly (as a 20-year model dataset) with NCEP observations, thereby avoiding biasing the results towards the model's response in one state of ENSO variability. Additionally, we examine differences in MJO behavior in the two extreme ENSO regimes in section 4.

To establish the extreme ENSO regimes, we compute the ENSO Niño 3.4 Index for the 500 years from the CCSM base run monthly mean model output. Then a sliding 10-year window is employed to compute a time-varying variance for these 500 years. The two 10-year periods with highest and lowest variability of ENSO are then identified, as shown in Fig. 2.1. Each case contains roughly 2.5 El Niño to La Niña transitions, with the amplitude of ENSO in the strong case being 2-3 times that of the weak variance case. CCSM4 was reinitialized from the base run CCSM4 for these periods (with perfect restarts) and output was saved as 1-day averages in order to explore the high frequency content of MJO in CCSM4. Saved fields included zonal and meridional winds, vertical velocity, specific humidity, relative humidity, temperature, geopotential, precipitation, and cloud fraction at all levels, plus net longwave, shortwave, latent and sensible fluxes at the surface and large-scale (liquid plus ice) precipitation rate. Hereafter, when necessary, the two 10-year simulations of CCSM4 will be labeled HENSO for the High ENSO variability case and LENSO for the Low ENSO variability case. The combined 20-year run forms the basis for our MJO analysis

2.2.1 Observational data

We validate the MJO characteristics in the 20-year CCSM simulation against the Advanced Very High Resolution Radiometer (AVHRR) Out-going Longwave Radiation (OLR) (Liebmann and Smith, 1996), which is a proxy for convective activity. We use rainfall from the Climate Prediction Center Merged Analysis of Precipitation (CMAP) (Xie and Arkin, 1997) and the Global Precipitation Climatology Project (GPCP) (Huffman et al., 2001). The upper (200 hPa) and lower (850 hPa) tropospheric zonal winds are from National Centers for Environmental Prediction (NCEP) National Center for Atmospheric Research (NCAR) reanalysis data (Kalnay et al., 1996).

2.3   MJO characteristics in CCSM4

2.3.1   MJO diagnostics

The MJOWG has established a set of MJO diagnostics that are accepted by the MJO community as the benchmark of MJO model performance (Waliser et al., 2008). They include 2 levels of MJO diagnostics for both winter (November to April) and summer (May to October), plus the evaluation of mean state variables that have been implicated as being directly related to MJO simulation skill. We adopt this strategy here and compute diagnostics for both boreal summer and winter intraseasonal variability and mean state. The MJO band is isolated by running all fields through a 20-100 day Lanczos bandpass filter, following Waliser et al. (2008).

As an important starting point, the mean state of relevant variables are first validated. We did several comparisons of background state during the 20-year model run versus observed climatology. For example, a comparison of the mean zonal 850 hPa winds in NCEP (observations) with the mean zonal 850 hPa winds for the CCSM runs reveals that the model simulations have structures that are comparable to the observed winds from NCEP. But the magnitude of the mean easterlies in the Pacific is 50% greater than observed and the westerlies over the Maritime Continent are somewhat weaker than observed (Fig 2.2). These results are consistent with those of Zhou et al. (2011a) for CCSM-3.5.

2.3.2   Level 1 diagnostics

Level-1 diagnostics assess the dominant spatial and temporal scales, as well as propagation direction of convection and 850-hPa zonal wind. These diagnostics provide a general evaluation of the broadband intraseasonal variability associated with MJO.

We first consider the winter 20-100 day variance of the zonal 850 hPa winds. The color contours in Figure 2.3, which show the percentage of intraseasonal variance of zonal 850 hPa winds, in NCEP is comparable to that of the model simulation. The structure of the intraseasonal variance pattern in the model is consistent

with MJO characteristics, bearing minima in zonal wind variance along the equator in both the Indian and Pacific Oceans and a maximum variance over the maritime Continent. The total variance of these winds in CCSM4, shown as line contours in Fig. 2.3, is also reasonably consistent with observations. Note, however, that at least at the air-sea interface the Qscat observations suggest that in the equatorial east-Pacific NCEP winds are approximately 30% too weak (Large and Yeager, 2009).

Total OLR variance in CCSM4, shown by the line contours in Figure 2.4, tends to be higher than in observations, especially over the Maritime Continent. The percentage of winter 20-100 day variance in model OLR has comparable values to observations over the Maritime Continent and in the western equatorial Pacific. However, the model has much weaker intraseasonal OLR variance than observed in the central Indian Ocean. Taken together with the zonal wind results, this may be indicative of a weaker coupling between the dynamic fields and convection in the MJO initiation regions of the Indian Ocean.

Hovmöller diagrams for zonal winds (averaged from 5°N to 5°S) are used to visually illustrate the eastward propagation of MJO signals. We chose one year from the model run with strong MJO activity and compared it to one observed year with strong MJOs to highlight the propagation characteristics (Fig. 2.5). These years both included La Niña events, when the western tropical Pacific SST was anomalously warm. In the model, eastward propagation is evident during winter at speeds of roughly about 5 - 7 ms^{-1}, which is comparable to the observed phase speeds. Events in both the model and the observations originate in the Indian Ocean region and propagate around the globe. As also seen in observations, these events tend to weaken over the Maritime Continent and strengthen again in the western Pacific Ocean. Similar to observations, albeit more pronounced, the model MJO eastward propagating activity in summer months is much weaker than in winter.

Power spectra of the wavenumber-frequency characteristics of observed winter MJOs reveal a dominant peak for zonal wavenumber 1 and period 60 days, with a broadbanded structure that extends to zonal wavenumbers 2 and 3 over periods

of 30-80 days (Fig. 2.6). The model contains peaks in this band, but the dominant peak at 60 days is somewhat stronger and more broadbanded than observations and additional peaks occur at higher frequencies that suggest the model MJOs are not as coherent as observations. Overall, CCSM4 contains significant eastward propagating energy in the same frequency range for wavenumbers in the MJO band during the winter season, but the signals have more energy than observations.

2.3.3   Level 2 diagnostics

Level-2 diagnostics assess the coupling between the dynamic and thermodynamic variables. In addition to single variable spectral calculations, cross-spectral calculations are computed to quantify the coherence and phase relationships between different variables. The cross-spectral plots demonstrate that the thermodynamic and dynamic effects are coupled.

Fig. 2.7 shows the coherence squared and phase between equatorial OLR and 850-hPa zonal winds for the symmetric components of the two fields (Hendon and Wheeler, 2008). The symmetric component physically represents the symmetric dynamics about the equator, which is a first-order characteristic of the observed MJO. The left panels show the spectrum across a broad range of scales, while the right panels show a more detailed view of the scales of the MJO.

Observations exhibit a high degree of coherence and an approximately 90-degree phase lag between convection and 850 hPa winds for zonal wavenumber 1-3 in the 30-80 day band (Fig. 2.7 a,b). Although climate models are well known to have difficulty simulating this feature (e.g., Zhang et al., 2006a; Zhou et al., 2011a), CCSM4 exhibits strong coherence in this low-wavenumber band, with lags similar to observations. For wavenumber 1, model coherency peaks at higher frequencies, however, near 30-day periods compared to the 40-day peak for observations (Fig. 2.7 c,d). This modeled coherency relation suggests that convectively coupled MJO's occur in the model for wavenumber 1. The model's spread of coherency into higher frequencies at wavenumber 1, however, suggests that more linear Kelvin wave activity, with a convective signature, is present in CCSM4 than in observations (Roundy, 2008). To distinguish whether the coherency peak at

wavenumber 1 is due to a simple Kelvin wave, Figure 2.8 shows the antisymmetric part of the coherency relationship for the MJO band, which should have no imprint of a linear Kelvin wave. Observations reveal significant coherency (0.15-0.35) for wavenumber 1. The model also has significant coherency (0.05-0.15) in this band, although somewhat weaker than observations. This antisymmetric structure is clearly indicative of convectively coupled MJO behavior at wavenumber 1.

At wavenumbers 2 and 3 in Fig. 2.7 (c,d), CCSM4 has much lower convergence - convection coherency in the MJO 40-80 day period band than observations. Instead, CCSM4 exhibits high convergence - convection coherency for these two wavenumbers at 10 - 15 day periods, which is is indicative of Kelvin waves bearing a convective signature, since the coherence falls along the linear dispersion curves. The antisymmetric part of the model spectrum (Fig. 2.8) has no significant coherence at these periods and wavenumbers, supporting this interpretation. This part of the response is associated with intraseasonal oscillations that travel at speeds of 10-22 m/s, which are faster than the typical observed MJO phase speed of 5 ms^{-1}. This weakly energetic and fast propagation at wavenumbers 2 and 3 in CCSM4 may be associated with a lack of coupling between MJO and oceanic Kelvin waves in the central equatorial Pacific, which Roundy and Kravitz (2009) identified as an important mechanism for slowing and amplifying higher-wavenumber observed MJO in this region.

The faster phase speed of MJO in CCSM is also evident in Fig. 2.9b, which shows the lag correlation between the convection and the dynamic winds for observations and model. Model MJO activity tends to propagate to the Maritime Continent where it breaks up and then reorganizes over the western Pacific and continues propagating across the Pacific slightly faster and even further than observations suggest.

We next use the Wheeler and Hendon (2004), (hereafter WH04) technique to extract the dominant MJO spatial and temporal modes. Combined EOFs (CEOFs), using OLR, U850 and U200, each bandpassed to the 20-100 period band, are computed. This multivariate approach isolates the convective and baroclinic zonal wind signature of the MJO. We specifically focus on the evaluation of the 1)

vertical baroclinic structure in the winds and the lag in OLR and convection with the winds depicting a moving convection and convergence system, 2) evolution of the MJO life cycle in the model simulations, 3) MJO life cycle composite depicting the various phases in the MJO evolution with respect to convection and the convergence zone.

The two leading modes in both model and observations correspond to MJO patterns and timescales. Fig. 2.10 shows the 15°N-15°S average of the CCSM-4 MJO CEOF 1 and 2 for all three variables. Compared to the observed modes shown in Fig. 2.11, Mode 2 from observations corresponds to Mode 1 of the CCSM4. The longitudinal location of the maxima, minima and zero crossings of all three variables correspond well between model and observations. Likewise, observational Mode 1 corresponds well to the structures seen in Mode 2 of the CCSM. The magnitudes of the CEOFs in the model are about 40% smaller than the same in the observed fields. We conclude that in this period band, MJO phasing between physical variables in CCSM4 is remarkably consistent with observations but are weaker in magnitude. The partitioning of variance in the Combined EOF analysis is - OLR (18%), U200(37%), U850(50%) for the first two combined EOFs. The variance explained by the PCs individually are : PC1 - OLR (10%), U200(21%), U850(26%), PC2 - OLR (8%), U200(16%), U850(24%). This too is remarkably consistent with the observed values of Waliser et al. (2008), viz., PC1_obs - OLR (13%), U200(22%), U850(32%), PC2_obs - OLR (16%), U200(24%), U850(23%).

The lag correlation between PC-1 and PC-2 provides a measure of temporal coherency for the eastward propagating MJO. These are calculated for year-round fields for CCSM4 and shown in Fig. 2.12a. The familiar S-shape found in observations occurs (Waliser et al., 2008), with peak correlations of roughly 0.6 occurring at $\pm$ 8 day lags in CCSM4, compared to 0.7 peak at $\pm$ 10 day lags in observations. This indicates the dominant period is roughly 32 days in the model, but roughly 40 days in the observations, consistent with the higher power seen at high frequencies in CCSM4 in the the power spectra of Fig. 2.6. The phase relationship indicates that the multivariate EOF-1 and EOF-2 are a quadrature pair. This pair of leading EOFs represents coherent eastward propagation of MJO. It is a well-known

challenge for GCMs to properly represent this coherent quadrature pair. Further, to verify whether the extracted MJO modes are a physically meaningful mode of variability and are distinct from noise, we project the leading EOFs derived from filtered data onto unfiltered data (after only removing the seasonal cycle). The power spectrum of the unfiltered PCs, shown in Fig. 2.12b, yields a prominent peak at MJO time scales, very similar to Waliser et al. (2008) except for the higher energy in the model spectral "shoulder" at 20-30 day periods. This increases our confidence in the diagnostics that the modes of variability obtained are indeed meaningful.

The two leading multivariate EOFs can also be used to derive a composite MJO life cycle for boreal summer or winter, following WH04. The composite is constructed by selecting full fields of U850, U200 and OLR during the time intervals when MJO is strongly excited. The amplitude of the MJO is defined by $PC1^2 + PC2^2$ after PC1 and PC2 are normalized to unit standard deviation. The time intervals for the composite fields are defined as times when the MJO index exceeds 1.5 (Fig. 3.1). The amplitudes for the MJO Index during the two model time periods HENSO and LENSO are shown in Fig. 3.1. The phase of the MJO is defined as atan(PC2/PC1). For each of eight phases, composites are generated by averaging across all days that exceed the specified amplitude threshold. The composite life cycle for the boreal winter MJO in the CCSM4 simulation is shown in Fig. 2.13. The same for observations is shown in Fig. 2.14.

In general, the CCSM4 generates a realistic succession of phases associated with MJO (Fig. 2.13), very similar to those from observations (Fig. 2.14) in many respects. The model phases differ from those in observations in a few details. The convection in phase 3 in the model composite occurs off the equator rather than over it as in observations (consistent with the variance plots of OLR in Fig. 2.4). From phase 3 to phase 5, westerlies increase in the eastern Indian Ocean and intensify convection over the Maritime continent, but not as strongly as observations. The intensity of the OLR in the model is also lower and more widespread in model phases 3 - 6 compared to those in observations. Compared to a similar composite shown by Zhou et al. (2011a) for CCSM3.5, CCSM4 exhibits

a more realistic OLR pattern over the Indian Ocean region during the initiation phase and more coherent propagating components across the Maritime Continent. Likewise, the phase composites for CCSM4 exhibit much more organized patterns of MJO propagation than found by Zhang and Mu (2005) for CCM3.

We next consider the nature of the precipitation in the intraseasonal band. Fig. 2.15 shows the variance in the intraseasonal precipitation from the model and GPCP observations. The model precipitation variance is about 50% greater than that in the observations, suggesting that the convectively coupled intraseasonal bands of MJO generate excessive precipitation in the model. The intraseasonal variance of the diabatic heating caused by convection parameterized in the model has a spatial pattern that is similar to the variance of the precipitation (Fig. 2.16). This supports the idea that the excessive precipitation in the model is due to large scale convective systems (such as the MJO) in the intraseasonal band. In the Indian Ocean initiation region of MJO, during phase 2 and 3 of the composite MJO, the ratio of large-scale precipitation resolved by the model to the Zhang-McFarlane parameterized precipitation is shown in Fig. 2.17. Roughly 30-35 % of the precipitation during MJO initiation in the Indian Ocean is resolved by the model and hence is consistent with a large scale intraseasonal convective system propagating rather the small-scale convection dominating the precipitation.

In summary, CCSM4 exhibits an energetic eastward propagating signal with MJO-like properties in the 20-100 day period band and 1-3 zonal wavenumber band. The model MJO has somewhat stronger amplitudes and faster propagation speeds than observations. For wavenumber 1, cross-spectral measures of convergence-convection relationships in the MJO period band are similar in strength to observations and indicate convectively coupled MJO is occurring. The more broadbanded coherency in frequency suggests that additional activity associated with Kelvin waves with a convective signature also occur in the model. This interpretation is even more evident for wavenumbers 2 and 3, which exhibit convergence-convection coherency for high frequencies that are outside the MJO band.

Compared to other global coupled models, CCSM4 exhibits relatively high

skill in simulating these intraseasonal oscillations. As compared to the models analyzed by Kim et al. (2009a), CCSM4 has pronounced energy in the MJO band and is comparable to the best models listed, viz., ECHAM4 and SPCAM. Also, the period and energy of the simulated ENSOs in CCSM4 are much improved compared to its previous CCSM versions. As shown by Kim et al. (2009), the period with maximum energy has shifted from 200 days for CCSM3.5 to the intraseasonal period of 70 days for CCSM4. Additionally, the intraseasonal wavenumber peak has broadened to include wavenumbers 1 - 3 from mainly being at wavenumber 1, with intraseasonal spectral power levels increased by about 50% in CCSM4 compared to CCSM-3.5. Besides improved parameterizations, some of the improvement over the results of Kim et al. (2009a) is likely due to the higher resolution used here (1 deg versus 2 deg) and the inclusion of full ocean coupling (rather than prescribed SST).

Since the phase of the OLR and winds in CCSM correspond well with the structure of MJO, the simulations of MJO can therefore be analyzed for relations with other climate phenomena such as the ENSO and the monsoons to attempt to understand their dynamical interactions. We next execute some preliminary attempts at addressing these issues in the following chapter.

2.4   Summary

Simulating and forecasting the MJO is of central importance to the global climate and weather community, especially as models continue to increase resolution and resolve the various processes that contribute to intraseasonal variability. Yet most climate models today fail to simulate even the large-scale features of the MJO. In this study, we evaluate the performance of a 20-year run of CCSM4 in reproducing the primary characteristics of MJO, based on diagnostics established by the MJOWG.

CCSM4 produces coherent, broadbanded and energetic patterns in eastward propagating intraseasonal zonal winds and OLR in the tropical Indian and Pacific Oceans that are generally consistent with MJO characteristics. Strong peaks occur

in coherence spectra with periods between 20-100 days and zonal wavenumbers between 1 and 3. Model MJO's, however, tend to be more broadbanded in frequency than observation, with higher frequencies being associated with zonal wavenumbers in the MJO band. But broadscale patterns, as revealed in combined EOFs of U850, U200 and OLR, are remarkably consistent with observations and indicate that convective coupling occurs in the simulated MJOs.

2.5 Acknowledgements

Figure 2.1: 10-year sliding window variance of monthly-mean Niño 3.4 Index for the 500-year climate simulation of CCSM-4.
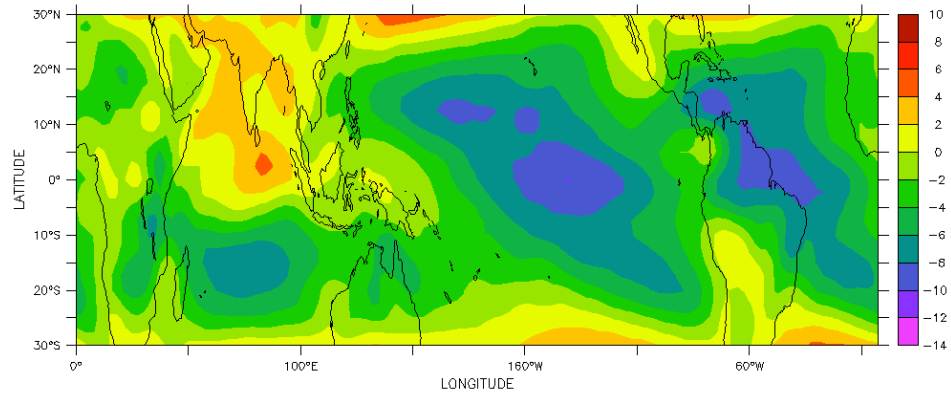
(a) Mean U850 - NCEP
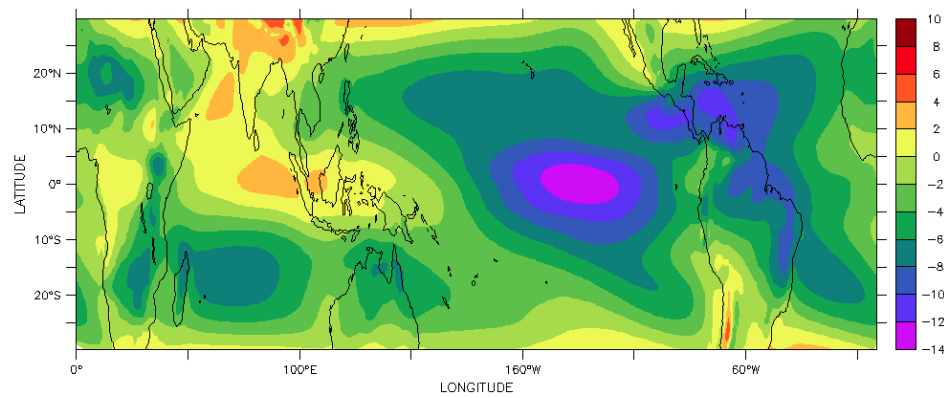
(b) Mean U850 - CCSM4

Figure 2.2: (a) NCEP(20 years) and (b) CCSM4 (20 years) annual mean zonal 850 hPa Winds in m/s. The period used in the calculations for NCEP is 1981-2000. The period used in the model is the 20 years combined from the high ENSO variance (HENSO) and low ENSO variance (LENSO) 10-year runs.

(a) Variance in U850 - NCEP

(b) Variance in U850 - CCSM
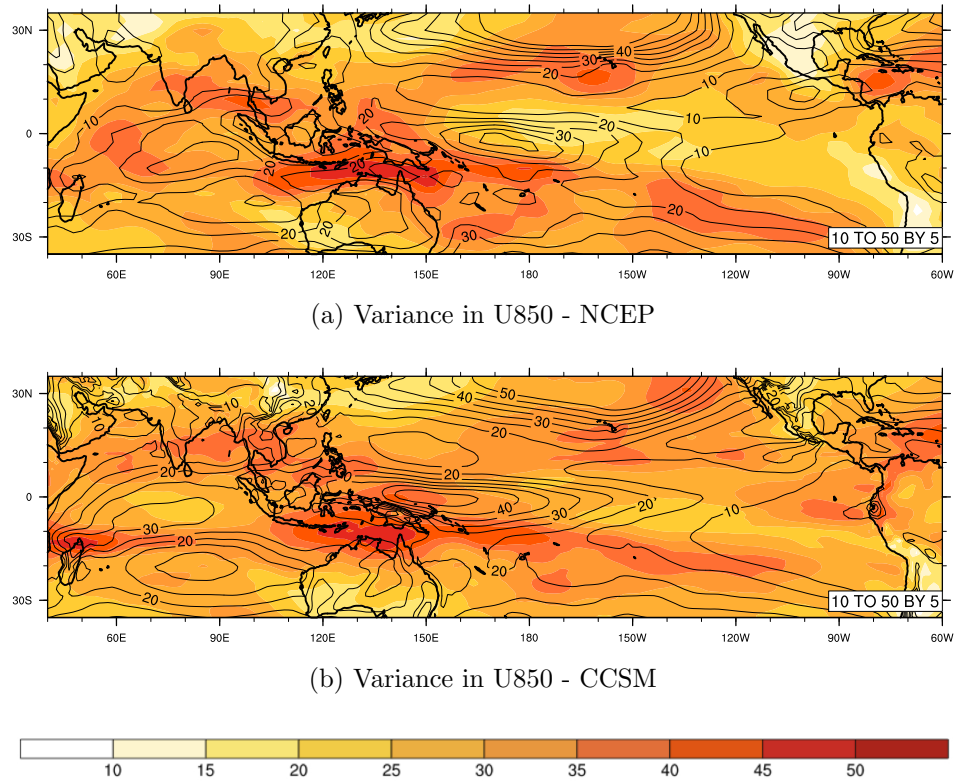
Figure 2.3: (a) NCEP and (b) CCSM4 variance (line contours) in zonal 850 hPa winds in m^2/s^2 and the percentage ratio of the intraseasonal bandpassed (20-100 day) daily fields to the total variance (color contours). The period used in the calculations is 20 yr (1981-2000 for NCEP).

(a) Variance in OLR - NOAA

(b) Variance in OLR - CCSM
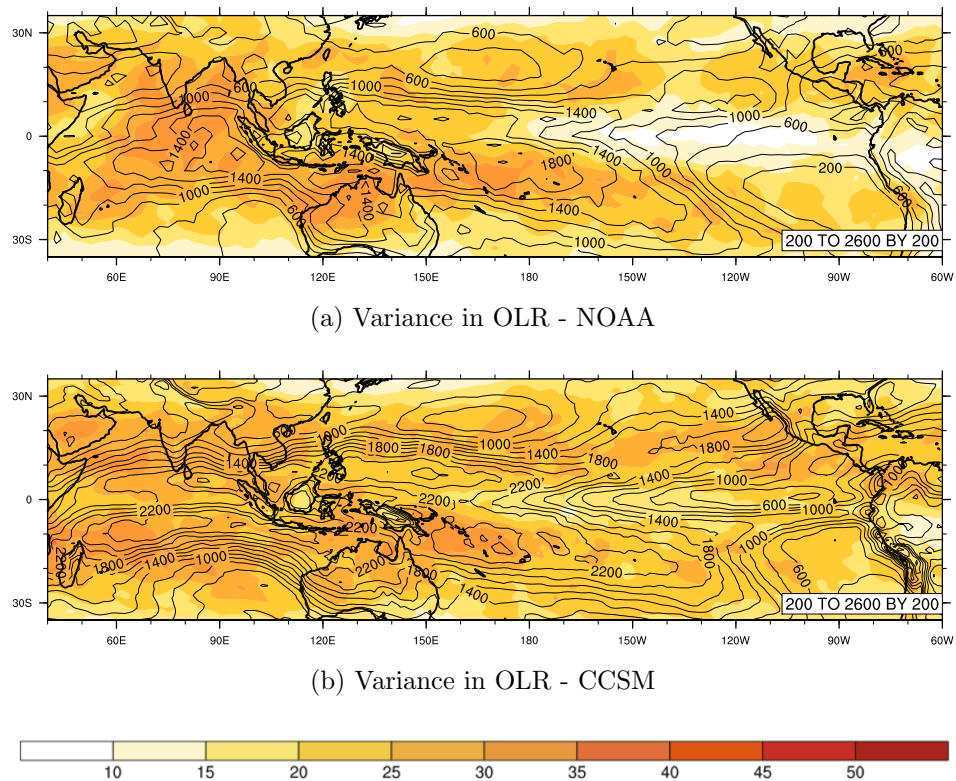
Figure 2.4: (a) NOAA AVHRR satellite OLR and (b) CCSM4 variance (line contours) in Outgoing Longwave Radiation in W^2/m^4 and the percentage ratio of the variance in the intraseasonal bandpassed (20-100 day) daily OLR fields to the total variance (color contours).The period used in the calculations is 20 yr (1981-2000 for NCEP).

(a) 1997 - NCEP 850 hPa U anomalies   (b) Year 3 - CCSM4 850 hPa U anomalies
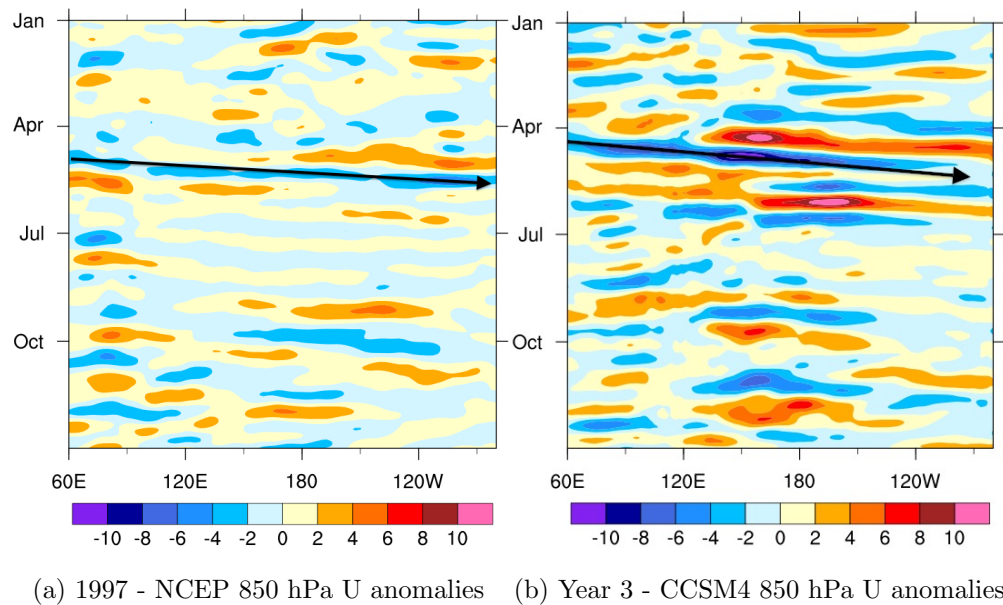
Figure 2.5: Hovmöller plot of the intraseasonal (20-100 day) zonal 850 hPa winds of (a) NCEP in 1997 compared to that of intraseasonal zonal 850 hPa winds of year 3 of the (b) CCSM-4 run. The arrow which is meant to represent 8 ms^{-1} is meant to guide the eye showing eastward propagation.

(a) 2D Power Spectrum - NCEP U850 (b) 2D Power Spectrum - CCSM4 U850

(c) 2D Power Spectrum - NOAA OLR (d) 2D Power Spectrum - CCSM4 OLR
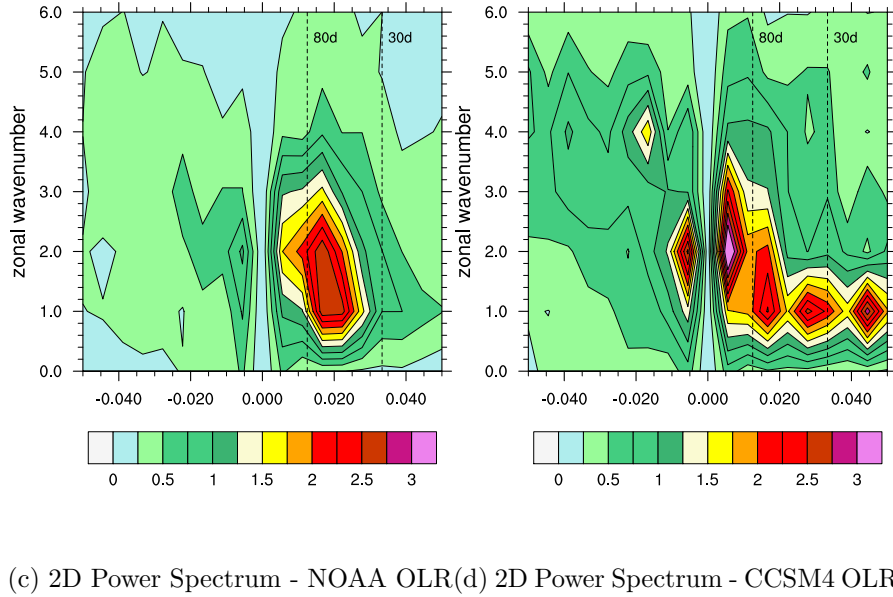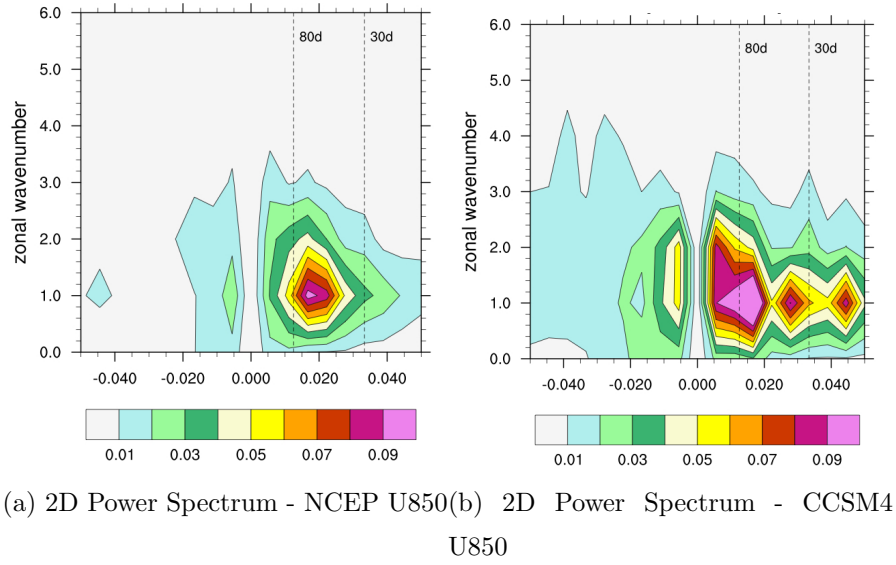
Figure 2.6: November-April wavenumber-frequency spectra of 10^oN-10^oS-averaged daily zonal 850 hPa winds of (a) NCEP (1981 - 2000) and (b) CCSM4 (20 years of HENSO and LENSO run) and daily OLR fields of (c) NOAA Satellite OLR (1981 - 2000) and (d) CCSM4. Individual spectra were calculated for each year, and then averaged over 20 years of data. Only the climatological seasonal cycle and time mean for each November-April segment were removed before calculation of the spectra. Units for the zonal wind spectrum are $m^2\,s^{-2}$ per frequency interval per wavenumber interval. The bandwidth is $(180\ \text{day})^{-1}$

(a) NCEP Winds and Satellite OLR

(b) NCEP

(c) CCSM4 Winds and OLR
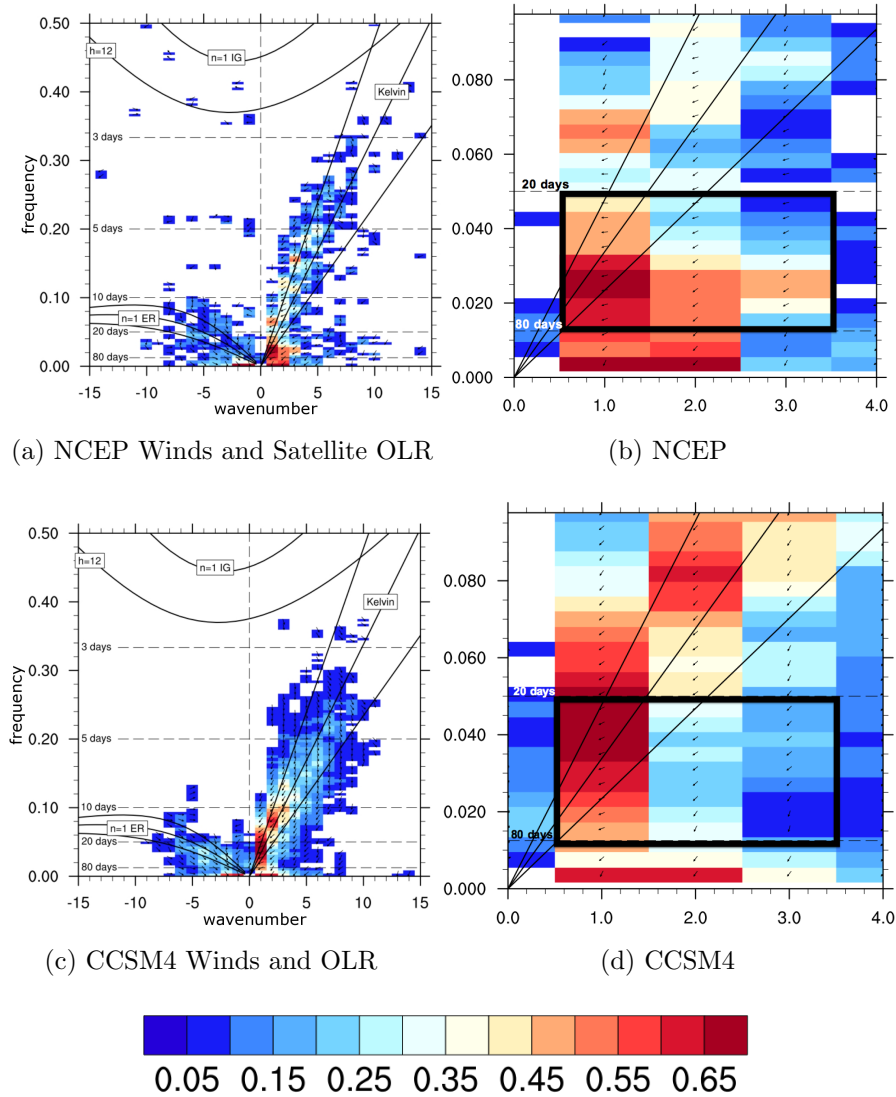
(d) CCSM4

Figure 2.7: Symmetric spectrum of coherence squared (colors) and phase lag (vectors) between zonal winds at 850 hPa winds and OLR are shown for (a) NCEP winds and satellite OLR (c) CCSM4 winds and OLR; (b) and (d) are expanded views of the MJO-relevant parts of the spectra. Cross spectra are calculated using daily data during all seasons on 256-day-long segments, with consecutive segments overlapping by 206 days. A phase of 0° is represented by a vector directed upward. Dispersion curves for the $(n = -1)$ Kelvin, $n = 1$ equatorial Rossby (ER) and $(n = 1)$ Inertia-Gravity waves corresponding to three equivalent depths (h = 12, 25, and 50 m) in the shallow water equations are overlaid (black contours).

0.05 0.15 0.25 0.35 0.45 0.55 0.65
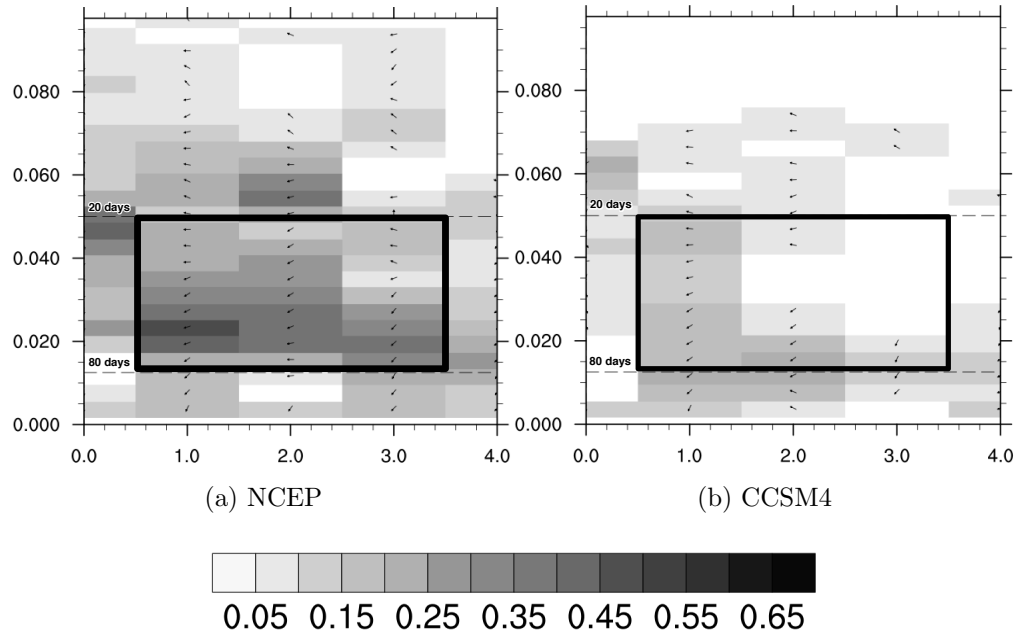
Figure 2.8: Antisymmetric spectrum of coherence squared (colors) and phase lag (vectors) between zonal winds at 850 hPa winds and OLR are shown for (a) NCEP winds and satellite OLR (b) CCSM4 winds and OLR as expanded views of the MJO-relevant parts of the spectra. Cross spectra are calculated using daily data during all seasons on 256-day-long segments, with consecutive segments overlapping by 206 days. Colors represent coherence squared between OLR and U850, and vectors represent the phase by which wind anomalies lag OLR anomalies, increasing in the clockwise direction. A phase of 0° is represented by a vector directed upward. MJO is defined as the spectral components within zonal wavenumbers 1 to 3 and having periods 20 to 80 days as marked by the black box in the right panels.
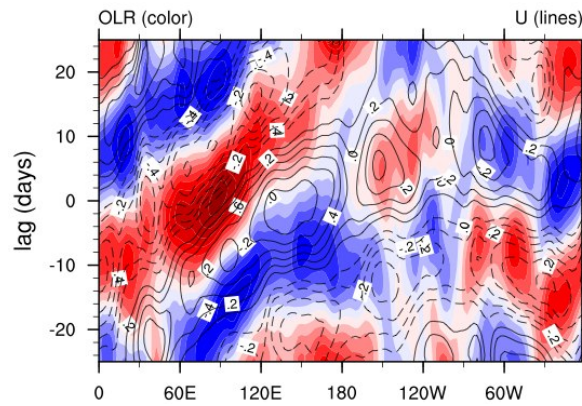
(a) Winter Lag Correlation in NCEP Winds and Satellite OLR
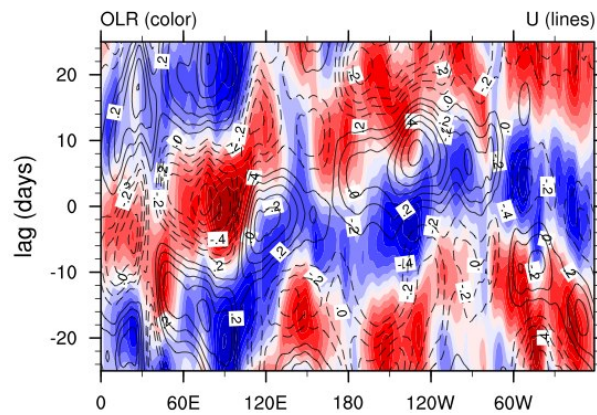
(b) Winter Lag Correlation in CCSM4 Winds and OLR

Figure 2.9: November-April lag-longitude diagram of 10°N-10°S-averaged intraseasonal OLR anomalies (colors) and intraseasonal 850-hPa zonal wind anomalies (contours) correlated against intraseasonal OLR at the Indian Ocean reference box (10°S-5°N, 75°-100°E) for (a) observations and (b) CCSM4.
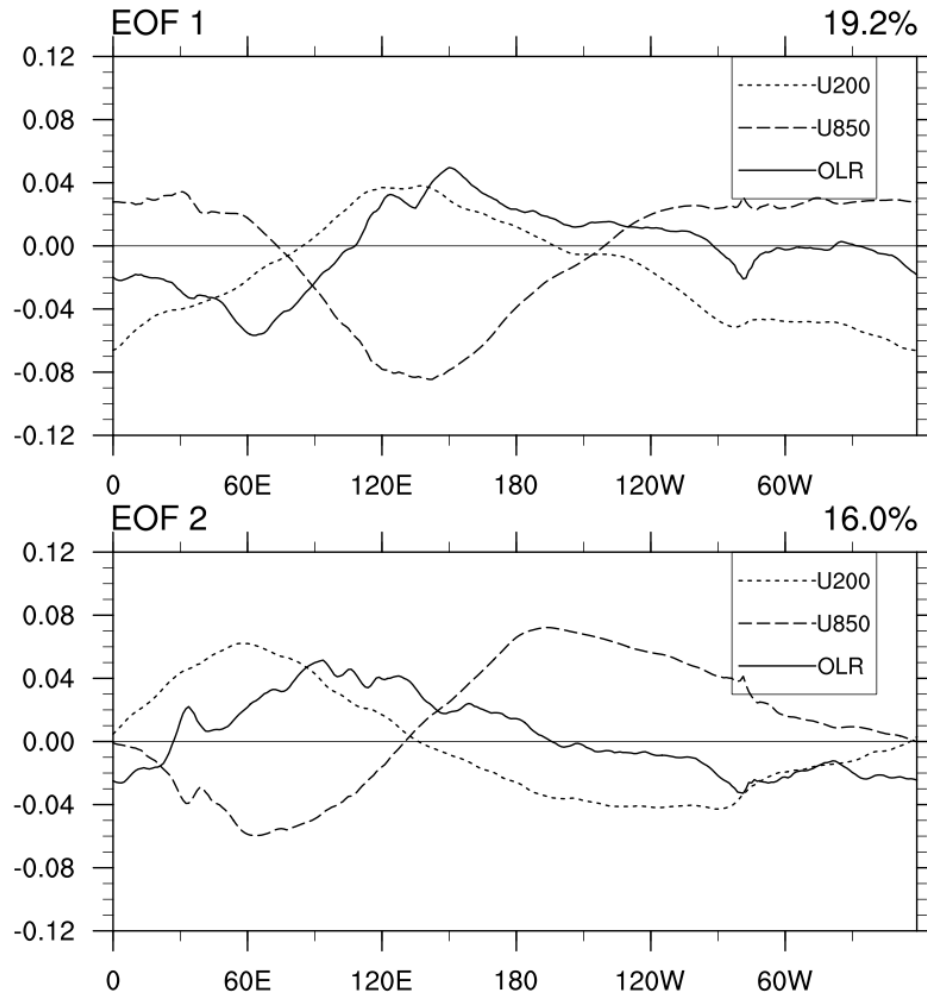
Figure 2.10: All-season multivariate (a) first and (b) second combined EOF (CEOF) modes of 20-100 day 15ºS-15ºN-averaged zonal wind at 850 hPa and 200 hPa and OLR from the 20 yr CCSM4 run. The total variance accounted for by each mode is shown in parenthesis at top of each panel.
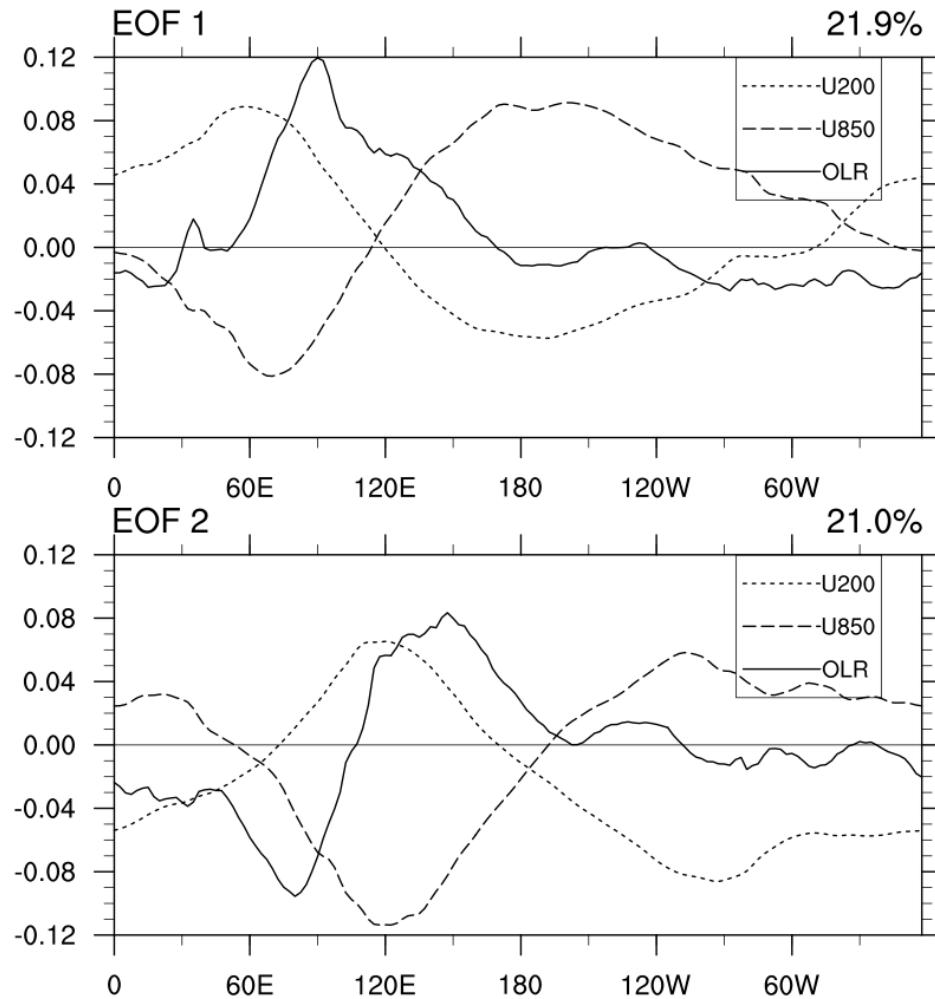
Figure 2.11: All-season multivariate (a) first and (b) second combined EOF (CEOF) modes of 20-100 day 15°S-15°N-averaged zonal wind at 850 hPa and 200 hPa from NCEP and OLR from the NOAA satellite for 1980 - 1999. The total variance accounted for by each mode is shown in parenthesis at top of each panel.
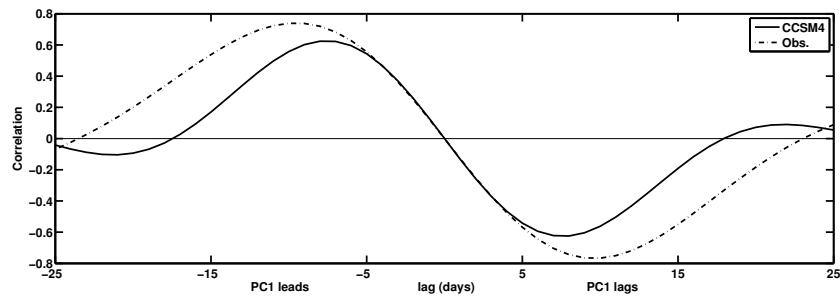
(a) Lag correlation in PC1 and PC2 for CCSM4 run and Observations.
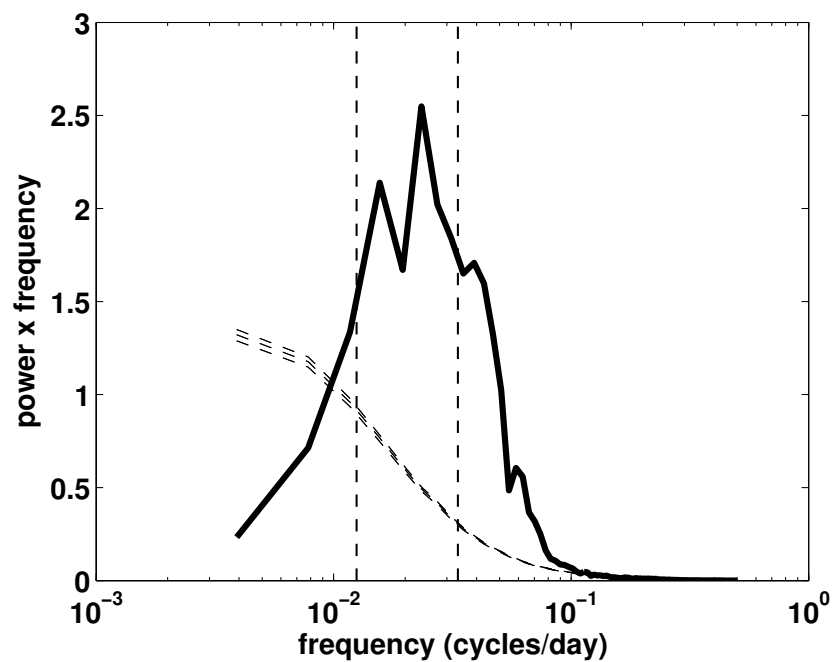
(b) Spectrum of the unfiltered PC derived by projecting CEOF1 onto the unfiltered data.

Figure 2.12: (a) Lag correlation between PC1 and PC2 of Multivariate EOF analysis of the intraseasonal zonal winds at 850 hPa, 200 hPa and intraseasonal OLR anomalies from the CCSM4 run and the Observations. (b) Power spectral density of the CCSM4 PC projected onto the unfiltered data. The dashed lines show the red noise spectrum and upper 90% and 95% confidence limits on this red noise spectrum.
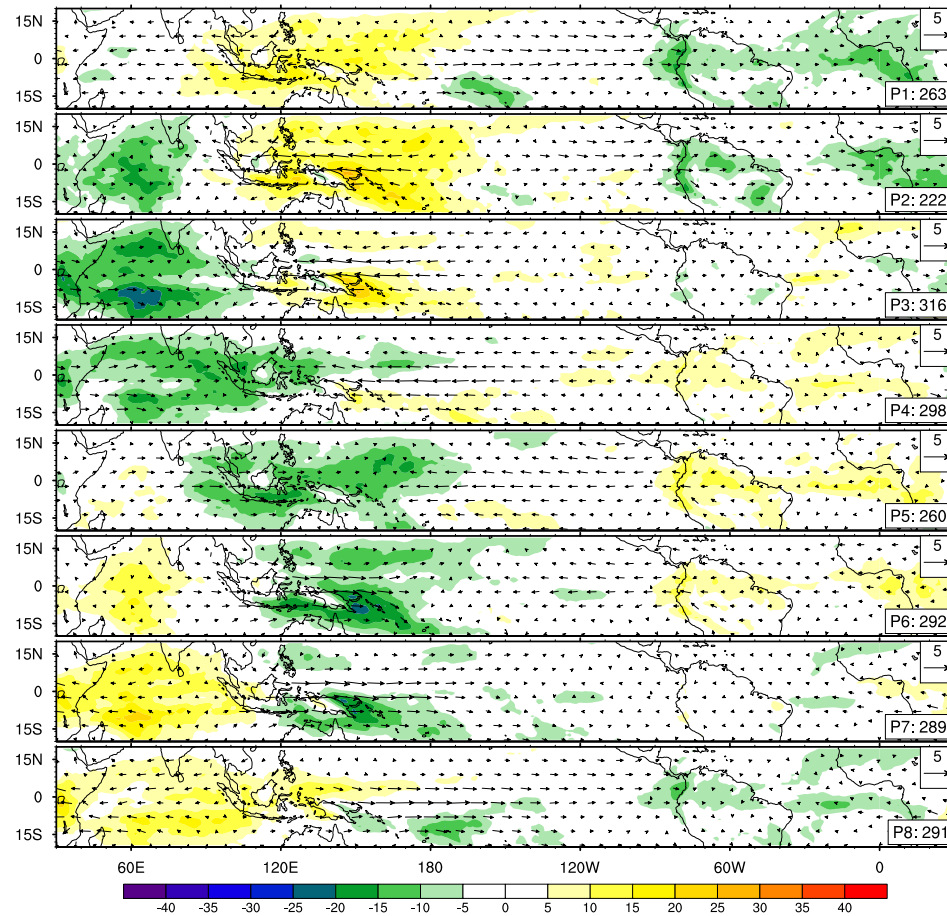
Figure 2.13: Composite November-April 20-100-day OLR (color, in Wm^{-2}) and 850 hPa wind anomalies (vectors) as a function of MJO phase for the 20 year CCSM run. The reference vector in units of m s^{-1} is shown at the top right. The number of days used to generate the composite for each phase is shown to the bottom right of each panel.
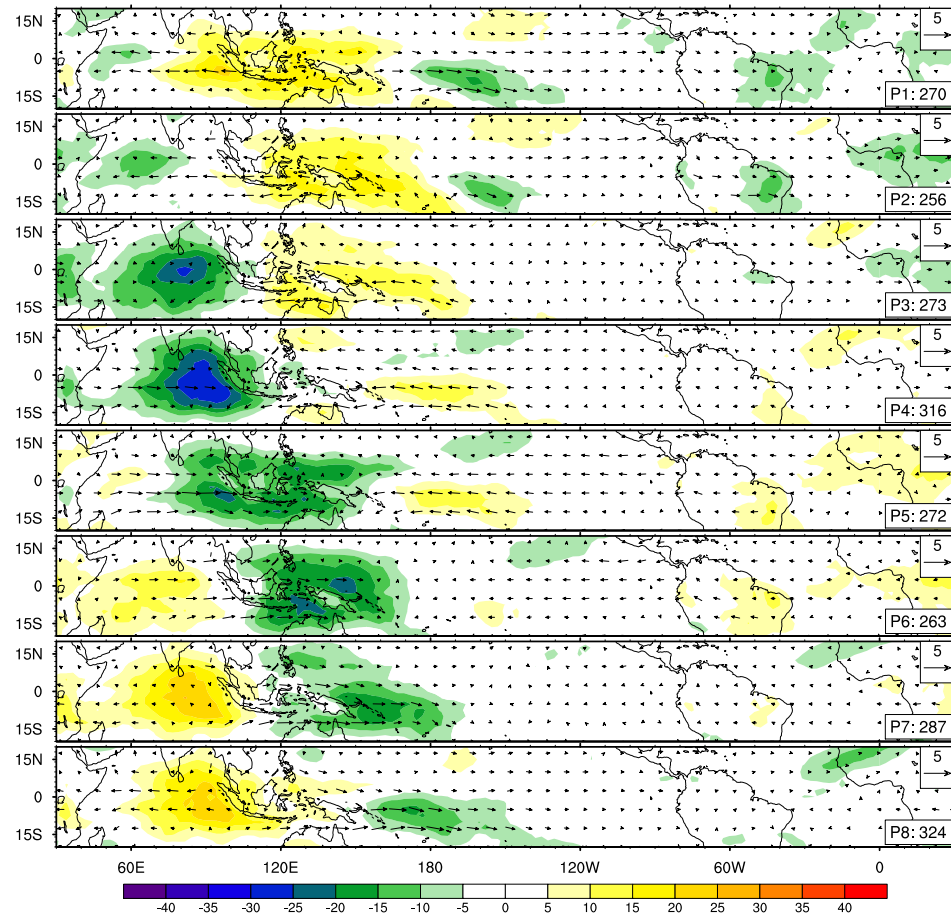
Figure 2.14: Composite November-April 20-100-day OLR (color, in Wm^{-2}) and 850 hPa wind anomalies (vectors) as a function of MJO phase for observations from 1980-1999. The reference vector in units of m s^{-1} is shown at the top right. The number of days used to generate the composite for each phase is shown to the bottom right of each panel.
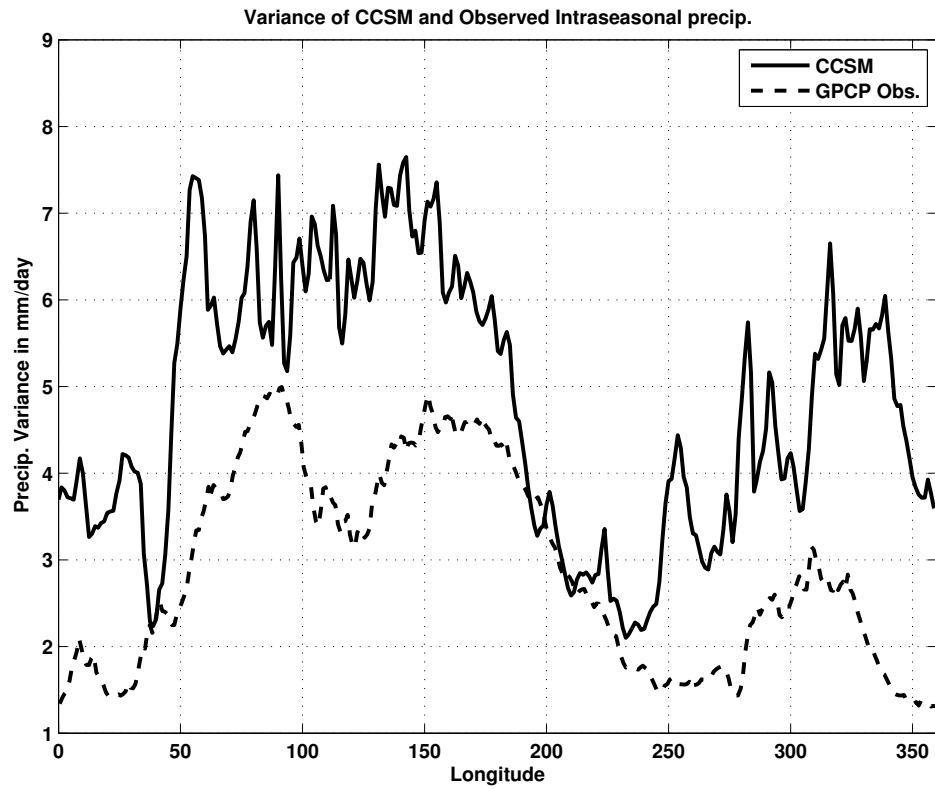
Figure 2.15: Variance in (20-100 day) intraseasonal precipitation averaged over 5^oN to 5^oS for 20 years of the CCSM4 run and GPCP observations (1996 - 2006).
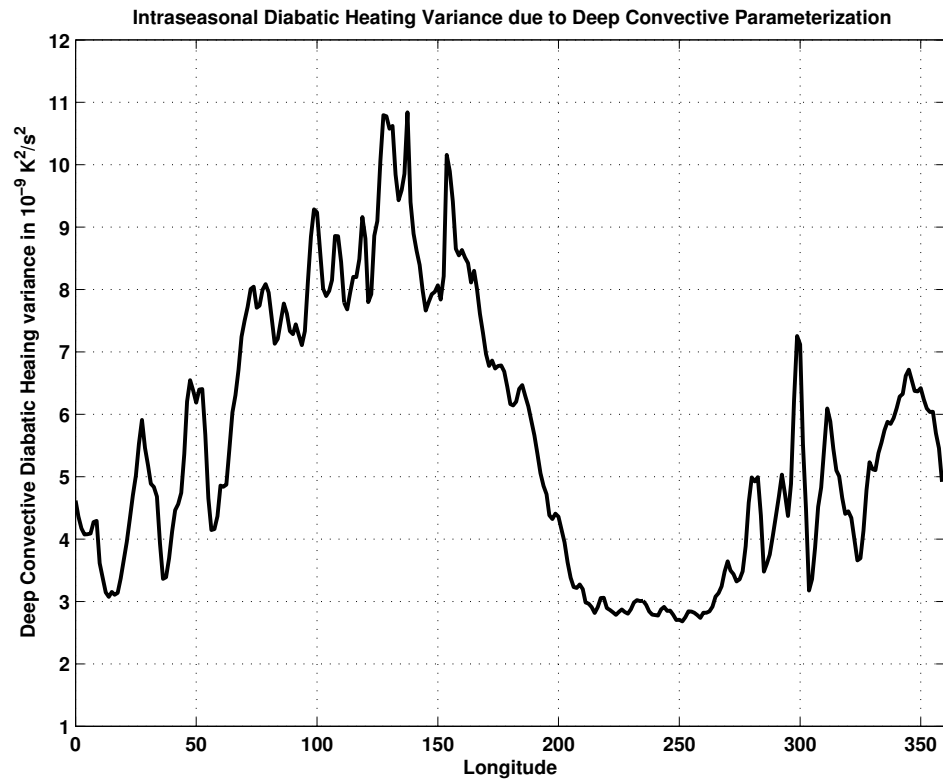
Figure 2.16: Variance in (20-100 day) intraseasonal diabatic heating due to deep convection parameterized by the Zhang-McFarlane scheme in CCSM4 averaged over 5^oN to 5^oS
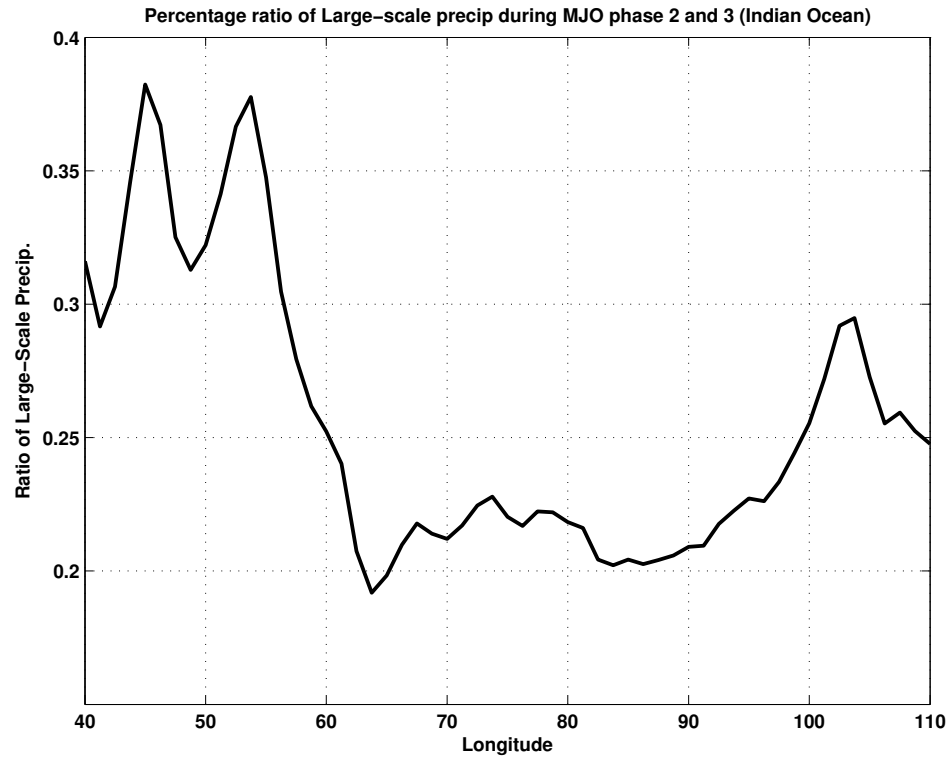
Figure 2.17: Percentage ratio of large scale (non-parameterized) precipitation to total precipitation in CCSM4 averaged over 5^oN to 5^oS during the phase 2 and 3 of MJO when (20-100 day) intraseasonal convection is predominantly in the Indian Ocean

Chapter 3

The MJO and Earth's Climate

The Madden-Julian Oscillation (MJO) is the most prominent form of tropical intraseasonal variability in the climate system. Relations between MJO in the model and its concurrence with other climate states are explored. Higher amplitude MJO activity occurs during weak warm ENSO events and during periods of weak meridional shear and negative zonal shear during the Indian Monsoons. MJO response to anthropogenic climate change is assessed using CCSM4 in a second study. A 50-year model run with the 20th century forcing is compared to a 50-year run with 21st century forcing projection of a 8.5 W/m^2 increase. Observations from other studies suggest that warming in the tropical Indian and Pacific Oceans in recent decades may have contributed to increased trends in the annual number of MJO events. Similar results suggesting an increase in the number of days with higher amplitude MJOs, and also a higher number of active MJO days in the Indian and West Pacific ocean are observed from the model simulation of global warming.

3.1 Introduction

The Madden-Julian Oscillation (MJO) is the most prominent form of tropical intraseasonal variability in the climate system (Madden, 1994; Zhang, 2005b). The influential nature of the MJO has been noted on monsoon systems (Carvalho and Jones, 2002; Carvalho et al., 2002; Lau and Waliser, 2005b), occur-

rences of extreme precipitation (Jones, 2000; Jones et al., 2004b), weather forecast accuracy Jones et al. (2004a,b); Jones and Carvalho (2011), interactions with El Niño/Southern Oscillation (McPhaden, 1999; Lau and Waliser, 2005b), deep ocean variability (Matthews, 2004; Matthews et al., 2007), distributions of tropical cyclones and hurricanes (Maloney, 2000; Kim et al., 2008) and surface chlorophyll variations in tropical oceans and coastal areas (Waliser et al., 2005; Isoguchi and Kawamura, 2006). The oscillation exhibits important seasonal changes and pronounced interannual variations (Jones and Carvalho, 2006, 2011; Pohl and Matthews, 2007).

Since the phase of the OLR and winds in CCSM correspond well with the structure of the MJO, the simulations of the MJO can therefore be analyzed for relations with other climate phenomena such as ENSO and the monsoons to attempt to understand their dynamical interactions. We next execute some preliminary attempts at addressing these issues.

3.2 Relations of MJO to other climate variables

3.2.1 MJO-ENSO relations

El Niño Southern Oscillation is the strongest interannually varying phenomenon in the tropical coupled ocean-atmosphere system. The MJOs are the strongest intraseasonal varying phenomena in the tropical coupled ocean-atmosphere system. Although both these phenomena have most of their energy in widely separated timescales, they have been shown to interact and modulate each other since both of them involve large-scale tropical convection, large-scale atmospheric circulation changes and teleconnections to other global weather phenomena (Hendon et al., 2007; Kessler and Kleeman, 2000; Marshall et al., 2009; Pohl et al., 2010).

The strength of the MJO varies year-to-year and some of this variability has been linked to ENSO (Kessler, 2001; Hendon et al., 2007; Tang and Yu, 2008). In nature, MJOs have been noted to be most active during neutral and weak ENSO years. To address this issue in CCSM4, Figure 3.1 shows MJO amplitude vs ENSO index for both the model run and observations. CCSM4 has a propensity

for stronger MJOs to occur during weak warm event conditions. Both model and observations exhibit the tendency for MJOs to occur more frequently and more energetically during warm conditions. This relation appears to hold for both winter and summer MJO periods. Since the 20 years of model output contains only five El Niño to La Niña transitions, however, the results are only suggestive.

Recent studies by Zhou et al. (2011a) show the importance of the background state of the winds in the tropical Indian Ocean and western tropical Pacific Ocean in the organization of intraseasonal perturbations to the mean background state of convection. The presence of a weak El Niño event establishes favorable conditions for MJOs to propagate further to the east in the western and central Pacific, thereby sustaining MJOs. This effect can be clearly seen in the model simulations, but is not so evident in the observations (Figure 3.1). On the other hand, comparing extreme ENSO conditions, there is a drop-off of the amount of MJO activity in both strong El Niño states and strong La Niña states. This is physically consistent with the idea that a strong reduction in SST in the western Pacific warm pool or the central Pacific can suppress MJO activity (Hendon et al., 2007).

There is also evidence from other studies that MJO influences the ENSO cycle (Kessler and Kleeman, 2000; Marshall et al., 2009; Lau, 2005). These studies have shown that the MJOs do not cause El Niño or La Niña, but they can change development and intensity of El Niño and La Niña episodes by significantly altering the low-level wind field that in turn, can result in variations in the ocean sub-surface conditions and later sea surface temperature (Newman et al., 2009). In our model runs, most of the MJO events were during weak warm events, which indicates that the strong ENSO events do not contemporaneously occur with strong MJOs and hence do not influence each other simultaneously.

We studied and compared the two 10-year model cases with high ENSO variance (HENSO) and low ENSO variance (LENSO), but the MJO variability in these two runs was not significantly different. The mean fields of the zonal winds, meridional winds and OLR were nearly indistinguishable. Minor differences were found in the variance of 850 hPa zonal winds, which tended to peak in the Maritime

Continent and the Central Pacific region during the HENSO period whereas during the LENSO episode the peak is constrained to the Maritime Continent. The Indian Ocean zonal winds and OLR had somewhat weaker intraseasonal variance during LENSO as compared to the HENSO period. The power spectral density of the zonal 850 hPa winds in the Indian Ocean contained higher peaks in the 20-100 day band in the HENSO case. In the western Pacific region, the power spectral density of the zonal 850 hPa winds contained broader and higher peaks in the LENSO case. The wavenumber frequency spectra revealed more power in the 30-40 day winds in the LENSO case, and less power in the 60-100 day winds. The phase speed of propagation of the MJO along the equator, gauged by the lag correlation plots of OLR and U850 as in Fig 2.9, was closer to that observed for HENSO. But our results for high and low ENSO variance cases did not appear to be statistically significant, given the short 10-year record length and small number of ENSO events that occurred within them.

3.2.2 MJO-Monsoon relations

MJOs interact considerably with the circulation and variability of Asian summer monsoon (Annamalai and Slingo, 2001; Waliser et al., 2003)). In the monsoon season, intraseasonal disturbances associated with the MJO tend to propagate in a northeast direction and strongly influence the active and break monsoon rainfall cycles over the South and East Asian continent (Yasunari, 1979; Annamalai and Slingo, 2001), including the genesis of synoptic systems (Goswami et al., 2003). Although it is still an area of research whether most of the intraseasonal variability associated with the northward propagating ISOs are independent of the MJOs or are generated by them, it is known that the MJOs during boreal summer do influence other weather phenomena in the South Asian region such as generating hurricanes (Camargo et al., 2009; Bessafi and Wheeler, 2006). Since the early work of Yasunari (1979), our knowledge about the MJO influence on the boreal summer monsoon has been enhanced many fold due to the availability of satellite data.

Indices have been defined to quantify Monsoon variability such as the precipitation indices averaged over the subcontinent and the dynamical monsoon in-

dices Webster-Yang Index (U^*_{850}-U^*_{200}, where U^* is the zonal wind anomaly, averaged over the region from 40^oE to 110° E, 0° - 20^oN) (Webster and Yang, 1992) and the Monsoon Hadley Index (V^*_{850}-V^*_{200}, where V^* is the meridional wind anomaly, averaged over the region from 70^oE to 110° E, 10^oN - 30^oN) (Goswami et al., 1999). These two indices measure the variability in the dynamical zonal shear and meridional shear over the North Indian Ocean respectively.

The possible relationships between MJO Index vs the strength of the meridional shear are explored by relating the time periods when MJO index exceeds 1.5 to three states of the MHI depending on whether the MHI is greater than 1, between 1 and -1 or less than -1 for the positive, neutral and negative states respectively. Fig. 3.2 shows these results for both model and observations, along with (a) the percentage of time MJO is *active* during the MHI states and (b) the average *strength* of MJO during the MHI states when MJO is active. The results, for both model and observations, show that MJO preferentially occur during negative MHI conditions. MJO amplitudes does not show any consistent relationship with MHI state in either model or observations. We also explored the relation between MJO Index and strength of the zonal shear, based on the WYI, but no consistent relation occurred between the model and observations in the results (Table 3.1).

The reason for the stronger activity of MJO during periods of negative meridional shear (northerly winds aloft and southerly winds below) is likely due to the enhanced vertical motion in the Hadley circulation over the Indian Ocean (Annamalai et al., 2003). In this situation, MJO is sustained and energized by the anomalous updrafts and convection over the warm equatorial Indian Ocean waters. Positive meridional shear, in contrast, implies increased subsidence and reduced convective activity, which suppresses MJO generation.

The role of Indian Ocean SST anomalies on the South Asian Monsoons has been a topic of several studies (e.g. Yuan et al., 2008; Krishnamurthy and Kirtman, 2003; Goswami and Mohan, 2001). Indian Ocean variability is known to be strongly seasonal and is related to ENSO variability. Many studies have focused on the role of the Indian Ocean Zonal Mode (IOZM) and its potential effect on the Asian monsoon (Saji et al., 1999; Webster et al., 1999; Annamalai

et al., 2003). The IOZM defined in Annamalai et al. (2003) is shown to correlate significantly with the Asian summer monsoon in a few studies (Behera et al., 1999; Yuan et al., 2008). Yet it is still an area of intense debate. Studies show that the IOZM is most significantly correlated with the Local Hadley cell which influences the Asian monsoons (Slingo and Annamalai, 2000). The IOZM has been noted to influence MJO activity, as well (Rao et al., 2007; Ajayamohan et al., 2008). Kug et al. (2009) showed that the high frequency atmospheric variability in the Indian Ocean is modulated by IOZM events and that MJO and synoptic eddies become significantly energetic during negative IOZM events.

The possible relationships between MJO and IOZM states are explored here by relating the time periods when MJO index exceeds 1.5 to three states of IOZM index (positive, neutral and negative phases when the IOZM index is greater than 1, between 1 and -1 and less than -1 correspondingly), defined by Annamalai et al. (2003), as shown in Fig. 3.3. Both the model and observations reveal a tendency for higher MJO activity during negative IOZM states. The model also has higher amplitude MJO during these times, but this aspect of the relationship is not found in the observations. These results are consistent with the idea that a negative IOZM event, which has anomalously warm ocean surface in the eastern and central Indian Ocean, would set up anomalous westerlies in the equatorial Indian Ocean and enhanced convection in the eastern Indian Ocean. Both of these processes sustain and support strong MJO activity (Inness et al., 2003; Zhou et al., 2011a; Waliser et al., 2008). However, since the run is of limited duration, this result is only suggestive of the dynamic interplay between MJO and IOZM, and it motivates further research on the issue.

After looking at contemporaneous relationships between the MJO and other climate phenomena such as the monsoons, ENSO and IODZ, the change in MJO activity due to global warming is studied using the CCSM4. The next section presents a preliminary discussion on this change.

3.3 MJO in a global warming scenario

While progress to understand the mechanisms of the MJO has improved over the years, global climate models still do not realistically reproduce all characteristics of the MJO (Zhang, 2005b; Lin et al., 2006b). Therefore, the question of how global warming will further impact the MJO has not been explored. The objective of this note is to show projections of possible changes in the activity of the MJO under one particular climate warming scenario.

There have been numerous studies of Tropical dynamics which are likely to be affected by global warming (Schneider, 2009; Vecchi et al., 2006; Soden, 2007; Allan and Soden, 2008). The physical changes such as increasing the heat content of the Tropical oceans, expansion of the Hadley cell and increase in volume of the global water cycle must necessarily impact MJO and intraseasonal dynamics in the Tropics eventually. Understanding how and when this impact will be realized is not often discussed in the context of global climate model results. While progress to understand the mechanisms of the MJO has improved over the years, global climate models still do not realistically reproduce all characteristics of the MJO (Zhang, 2005b; Lin et al., 2006b; Kim et al., 2009b). Therefore, the question of how global warming will further impact the MJO has not been explored.

The objective of this note is to show projections of possible changes in the activity of the MJO under one particular climate warming scenario. We look at two CCSM4 simulations of the MJO in two greenhouse forcing scenarios. One is in the present climate and the other is in an extreme global warming climate. The extreme global warming climate is defined as the Representative Concentration Pathways (RCP) 8.5 scenario which reflects the socio-economic pathway that reaches a radiative forcing of 8.5 W/m^2 by the year, 2100 [CMIP5 Report]. Here, the new version of the NCAR Community Climate System Model (CCSM4: Gent et al. 2011), with its improved representation of 20th century tropical variability (Deser et al., 2011), provides a case study for the MJO response to climate change.

3.3.1 Changes to Mean Circulation

The atmospheric overturning circulation is expected to weaken in response to climate change (Vecchi et al., 2006; Held and Soden, 2006) due to an imbalance between increases in the evaporative flux and convective precipitation. A similar signal of a weakening atmospheric circulation is seen in CCSM4. Figure 3.4 shows that the Inter-Tropical Convergence Zone (ITCZ) strengthens somewhat in the RCP8.5 simulation relative to the 20th century, especially in the southern branch South Pacific CZ (SPCZ). Figure 3.5 show the changes to wind stress magnitude: there is a strengthening of τ at 5^oN and S, which comes primarily from increased meridional wind stress. Reductions in τ are roughly 5-10% of the 20th century trade wind strength along the equator (Figure 3.5). Note the strong hemispheric asymmetry in the Pacific trade wind shifts, with the Northern Hemisphere trades (between 10-20°N) reduced by 2-3 times as much as their Southern Hemisphere counterparts, possibly due to the higher air-sea contrast created by the larger Northern Hemisphere land masses. The trade wind asymmetry is consistent with the hemispheric asymmetry in overall warming, which has been shown to be 2-3x stronger in the Northern Hemisphere in CCSM4. From geostrophy, a stronger reduction in the meridional temperature gradient in the Northern Hemisphere will in turn lead to a greater weakening of the trade winds.

Changes to ocean surface temperature are shown in Figure 3.4. Warming is most pronounced along the equator, consistent with predictions of enhanced meridional SST gradients from previous analyses (Gastineau and Soden, 2009; Liu et al., 2005; Xie et al., 2010). Stronger warming is seen in response to CO_2 increases in the eastern Pacific than in the west, which has been seen in multi-model experiments (DiNezio et al., 2009) as well as stabilized climate experiments with the CCSM3.5 (Stevenson et al., 2011). The mean zonal winds at 850 hPa do not change significantly in both the simulations as seen in Figure 3.6. The main change is witnessed as a decrease in the westerlies in the Indian Ocean indicating a weaker atmospheric circulation as shown by Vecchi et al. (2006) and Held and Soden (2006). The mean OLR decreases spatially in both the eastern and western Pacific Ocean indicating a weaker circulation over the region in a warmer Tropics.

A decreased east-west gradient in zonal surface temperature as seen in Figure 3.4 also indicates this weakening in zonal overturning in the atmosphere. The rest of the Tropics have similar mean OLR magnitudes for the two forced runs as seen in Figure 3.7. A weaker Tropical zonal circulation would mean weaker easterlies and stronger westerlies, which is a favorable background mean condition for the MJOs to initiate and propagate as shown in several previous studies (see Biello and Majda (2005) and references therein).

3.3.2   Trends in MJO amplitude

Trends in MJO amplitude and change in phase is studied in this section. The changes in the variance in zonal 850 hPa winds, precipitation and amplitude of MJOs in the two forced runs are studied and presented. The MJO is the most important mode of tropical intraseasonal variability. Observational studies based on reanalysis data indicate that the MJO shows regime changes on low-frequency time-scales (i.e. variations longer than 2 years) (Jones and Carvalho, 2011). In addition, the MJO exhibits a long-term trend in activity (Jones and Carvalho, 2006) including a trend toward greater event frequency after the mid-1970s (Jones and Carvalho, 2006; Pohl and Matthews, 2007). These changes in the MJO coincide with the long-term warming in the Indian Ocean and western Pacific warm pool. A possible linkage between increased MJO activity and warming in the tropical oceans is in agreement with the study of Slingo et al. (1999), although dynamical mechanisms remain to be demonstrated. Slingo et al. (1999) performed general circulation model experiments forced with observed SSTs and partially reproduced the positive trends in tropical intraseasonal amplitudes since the mid-1970s.

One significant challenge in the development of a comprehensive theory of the MJO has been to determine what dynamical mechanisms control the initiation of the oscillation. Kemball-Cook and Weare (2001), for instance, analyzed radiosonde data in the Indian Ocean, maritime Continent and western Pacific Ocean to investigate three possible mechanisms of MJO initiation: (i) extratropical triggering, (ii) tropical circumnavigating triggering and (iii) recharge - discharge. They used an instability index defined as moist static energy (h) at 1000 hPa minus that

at 500 hPa. (h = c_pT + Lq + gz; c_p = specific heat at constant pressure, T = temperature, L = latent heat of condensation, g = gravity acceleration, z = geopotential height). They showed that the instability index was well correlated with convective available potential energy (CAPE) and found support for the recharge - discharge mechanism. In this case, the initiation of organized convection during the MJO is initiated by a combination of low-level moist static energy build-up and concurrent drying of the mid-troposphere associated with subsidence from a previous cycle of MJO convection. Thus, a possible hypothesis for the observed positive trend in MJO activity is that warming of the tropical Indian Ocean and western Pacific increases the background CAPE necessary for triggering MJO events.

Hence it is important to mention other possible impacts that global warming might have on the MJO. These might include changes from longitudinal gradients of SST in the tropical Indian and Pacific Oceans, modifications in the mean state (Slingo et al., 2003) or changes in extratropical stochastic forcing on the MJO (Ray and Zhang, 2010). Lastly, it is relevant to note that this study investigated one aspect of a very complicated problem. Additional studies need to be developed to examine likely modifications in structure and differences in mechanisms associated with primary and successive MJO events.

Jones and Carvalho (2006) show that the activity of the MJO is lower in years prior to the mid-1970s, suggesting that the MJO may indeed become more active as tropical SSTs become warmer with implications for the effects of global warming on the coupled tropical atmosphere-ocean system. Zveryaev (2002) also notes interdecadal changes in intraseasonal variability during the Asian summer monsoon. Slingo et al. (1999) analyzed the NCEP/NCAR reanalyses and present very similar results to those obtained from the ECMWF 40-year reanalysis (ERA-40) adding more validity to the decadal variability identified by Zveryaev (2002).

The total variance in the zonal 850 hPa winds seen as line contours in Figure 3.8 shows a small decrease in the RCP8.5 forced run in the Pacific Ocean region. This would again indicate a weaker variation in the overturning circulation in the equatorial Pacific Ocean region.The intraseasonal variance in the zonal winds explains a higher percentage of the total variance indicating the strength

of the ISO winds to be either the same or slightly stronger in the warmer atmosphere than in the present day climate. Analysis of the intraseasonal precipitation shows a much stronger net increase in the variance of the total precipitation and also an increase in the percentage variance explained by ISOs (Figures 3.9,3.10). This shows that the wet events in present day climate are likely to be wetter in the warmer atmosphere and also dry spells are likely to be drier. This not only happens in the total precipitation but also in the intraseasonal events. This was the strongest indication of amplification of the water cycle in a global warming scenario in CCSM4 which has been studied earlier in idealized GCMs and climate models (Allan and Soden, 2008; Schneider et al., 2009; Schneider, 2009, 2010).

Computing the MJO Index for both the forced runs, the frequency of MJO amplitude occurrence in the 20th century and the RCP8.5 forced case is presented in Figure 3.11. The number of days of high MJO amplitude events in the global warming scenario is significantly higher than the 20th century run. The weaker MJOs of about the amplitude 2 (mean amplitude for both the periods) decreases in the global warming scenario. This is consistent with previous studies showing that the extreme events are amplified in a more active hydrological cycle due to a warmer atmosphere (Allan and Soden, 2008; Schneider et al., 2009). The changes in the MJO active days (when the MJO amplitude is greater than 1) in different regions around the world (identified from the MJO phases) are shown in Figure 3.12. The mean amplitude of the MJO events in different phases in the RCP8.5 case is always greater than the mean amplitude in the 20th century climate. A significant increase in the number of active MJO days is also seen in the Indian Ocean region, where the mean amplitude increases by 0.1, and the number of days increases by about 500. This is consistent with the large increase in variance of the intraseasonal precipitation observed in the Indian Ocean in the RCP8.5 case. There is a net decrease in the number of active MJO days over the Maritime Continent. The number of active MJO days in the Western Pacific also increases by about 100 days. This indicates higher amplitude MJO events occurring mostly in the Indian Ocean and some of them also propagating over into the W. Pacific. A detailed study of the propagation and structural changes in the MJOs between

the two climates is beyond the scope of this study and is proposed as future work.

3.4   Conclusion

The mechanism involved in the intiation, propagation and non-periodicity of the MJO continue to present a major challenge to develop a complete theory of the oscillation. Many previous studies have improved our understanding of the characteristics of the MJO on seasonal to interannual time scales. In contrast, the behavior of the MJO on time scales longer than interannual has been unknown, largely due to a lack of data records long enough to resolve intraseasonal variations. Only climate modeling studies which are yet to resolve very good MJO characteristics or reanalysis products are useful tools currently for such analysis. The reanalysis products are still developing in terms of having a good long term continuous time series overcoming the large data shortage in the early part of the previous century. Only now have climate models improved their skill in simulating MJOs sufficiently that they can be used for studies such as long term variability of the MJO reasonably.

Relations between MJO and other climate phenomena were explored as well, but no overwhelmingly strong links between ENSO state, Monsoonal flow or Indian Ocean Dipole mode were identified. In these short, 20-year runs, a tendency for MJO to be more energetic during weak warm ENSO conditions, negative Monsoon Hadley flow, and positive zonal shear, was noted. But longer runs and more detailed dynamical analysis will be needed to better understand what processes control MJO and what climate processes respond to MJO in CCSM4.

Increase in variance of precipitation and especially the variance in the intraseasonal precipitation indicates a more active hydrological cycle in global warming scenarios as seen in several previous studies. A histogram plot of the MJO amplitude and number of days shows an increase in the higher amplitude MJO active days and also in the very low or no MJO days. The net number of days with average MJO amplitude reduces in the global warming scenario. This is consistent with previous studies showing extreme precipitation events amplify in a

warmer atmosphere (Allan and Soden, 2008). It is also observed that the model MJOs are active (with amplitude greater than one) for significantly higher number of days in the Indian Ocean and W. Pacific with higher amplitudes in the warmer atmosphere.

The results from this study raise some important questions that deserve future investigation. Since summer and winter MJO activity involves significant feedbacks between convection and large-scale circulation, one can expect that low-frequency changes in the basic state will change the intraseasonal oscillations such as MJOs. Further studies with idealized GCMs and climate scale models need to be done to tease out the dynamical mechanisms forcing regime changes in the MJO. Links between regime changes in the MJO and other low-frequency modes of the coupled ocean-atmosphere system (ex: ENSO and Pacific Decadal Oscillation) need to be investigated further.

This study was based on a 100 year simulation of the MJO in a 20th century forcing scenario and a RCP8.5 forcing scenario. Ideally, a much longer data record would be necessary to reach definitive conclusions on the behavior of the MJO on long time scales. Unlike other phenomena such as ENSO, proxy records do not provide enough temporal resolution to resolve intraseasonal variability which vary at timescales of months. Hence studies of low-frequency changes in MJOs from proxy data records are not possible with current understanding and treatment of proxy records. Hence, coupled ocean-atmosphere simulations with numerical models that realistically represent the MJO might be able to provide further insight on the low-frequency variations in the MJO. Since the MJO is a critical component in modulating weather variability in the Tropics and extratropics of both hemispheres, knowledge of the long-term behavior of the MJO is very important in having a good understanding of future global climate change scenarios.

3.5 Acknowledgements

(a) MJO Index shaded by the intensity of the Nino 3.4 Index in CCSM4

(b) MJO Index shaded by the intensity of the Nino 3.4 Index in Observations

Figure 3.1: Daily MJO Index and ENSO Niño 3.4 Index in the (a) 20 years simulations compared to (b) observed MJO Index and ENSO Niño 3.4 Index (from NOAA). Warm(cold) events are defined as being persistently above(below) 0.5(-0.5) for atleast 3 months. During the observation period there were a total of 2400 El Niño days (1299 MJO active days), 3390 neutral days (1593 MJO days), 1410 La Niña days (646 MJO days). During the 20 years of CCSM4 simulations, there were a total of 1950 El Nino days (1437 MJO days), 3420 neutral days (1646 MJO days), 1830 La Nina days (784 MJO days).
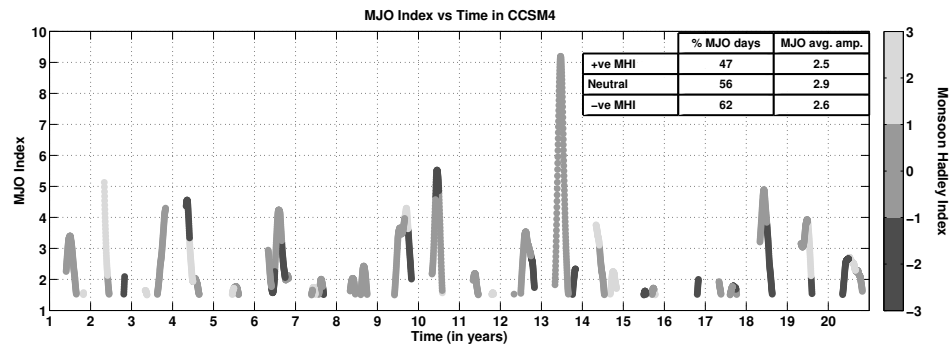
(a) MJO Index shaded by the intensity of the Monsoon Hadley shear Index in CCSM4
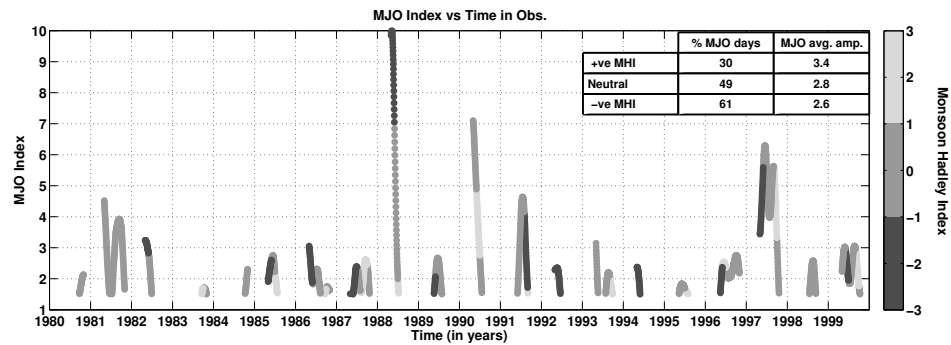
(b) MJO Index shaded by the intensity of the Monsoon Hadley shear Index in Obs.

Figure 3.2: MJO Index shaded by the intensity of the Monsoon Hadley Index in (a) CCSM4 in the 20 years simulations and in (b) Observations from 1980 - 2000. The shades indicate periods corresponding to different MHI states as indicated by the colorbar. The neutral periods are when the absolute value of the MHI index is less than 1.
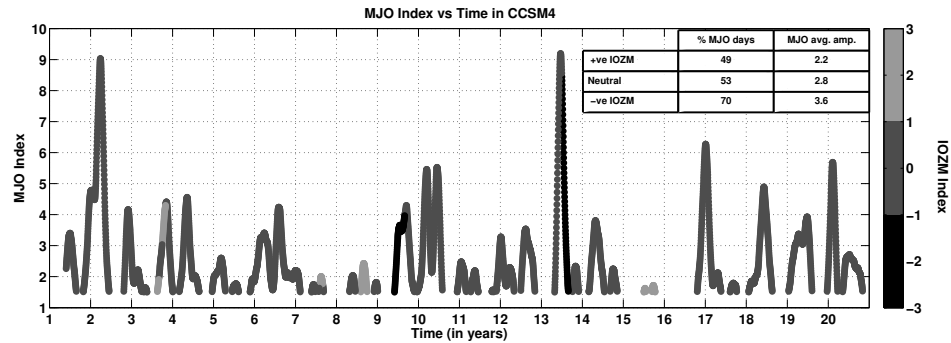
(a) MJO Index shaded by the intensity of the Indian Ocean Zonal Mode Index in CCSM4
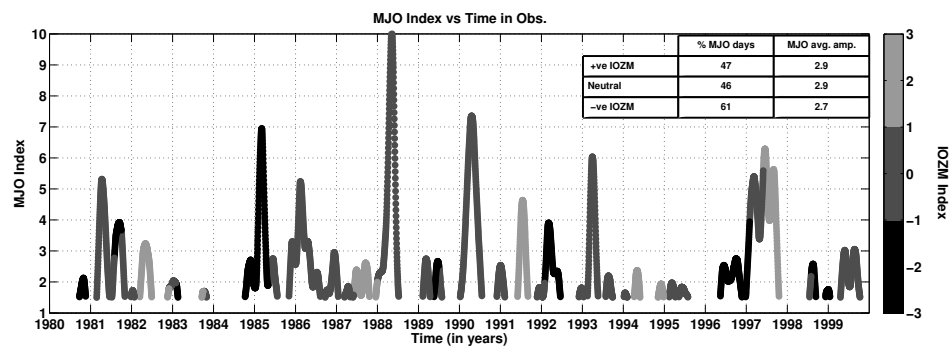
(b) MJO Index shaded by the intensity of the Indian Ocean Zonal Mode Index in Observations (1980 - 2000)

Figure 3.3: MJO Index shaded by the intensity of Indian Ocean Zonal Mode Index in (a) CCSM4 in the 20 years simulations and in the (b) observations (1980 - 1999). The shades indicate periods corresponding to different IOZM states as indicated by the colorbar. The neutral periods are when the absolute value of the IOZM index is less than 1.
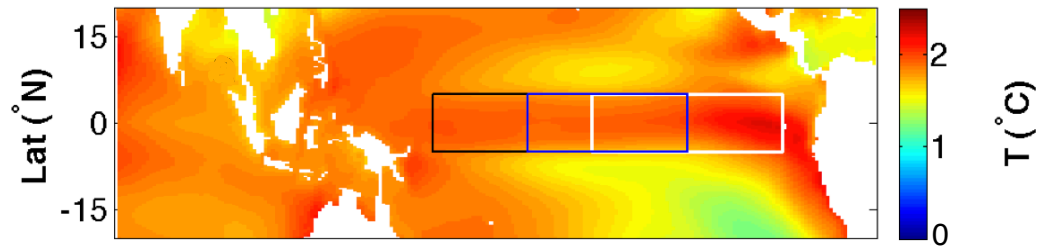
Figure 3.4: Surface Temperature change of RCP8.5 - 20th century simulation in CCSM4 (deg C) (Stevenson et al., 2011)
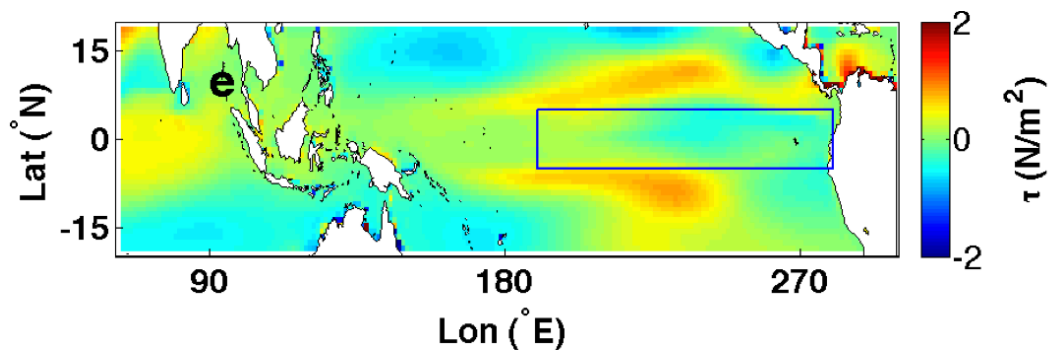
Figure 3.5: Change in wind stress of RCP8.5 - 20th century simulation in CCSM4 (N/m^2) (Stevenson et al., 2011)
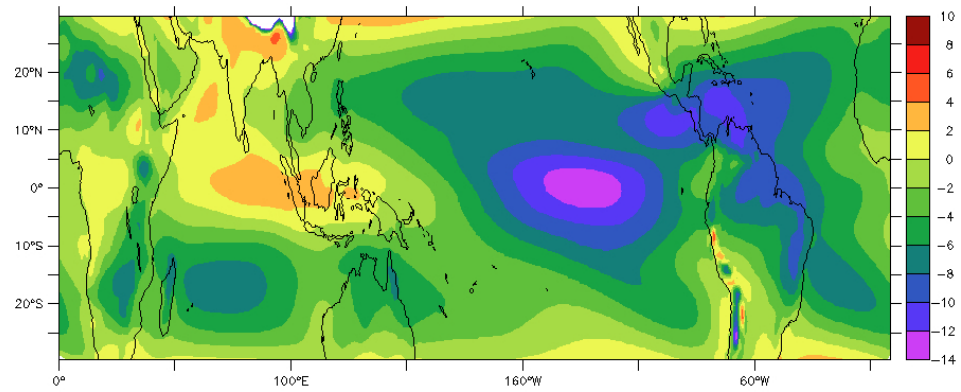
(a) 20th century forced CCSM4 run
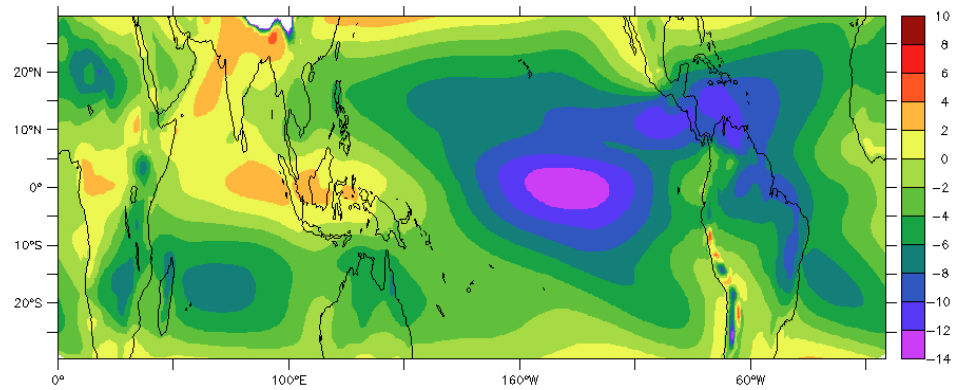
(b) RCP8.5 21st century forced CCSM4 run

Figure 3.6: Annual mean zonal winds at 850 hPa for (a) the 20th century forcing simulation and (b) RCP8.5 21st century simulation. The period used to calculate for both cases were the last 50 years from each century.
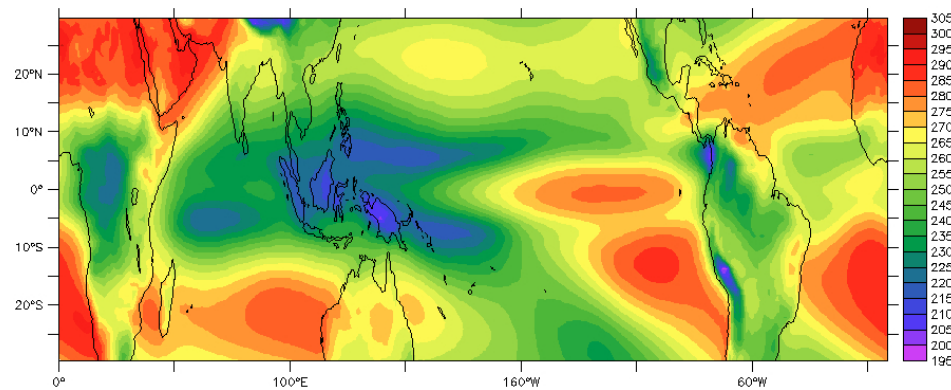
(a) 20th century forced CCSM4 run
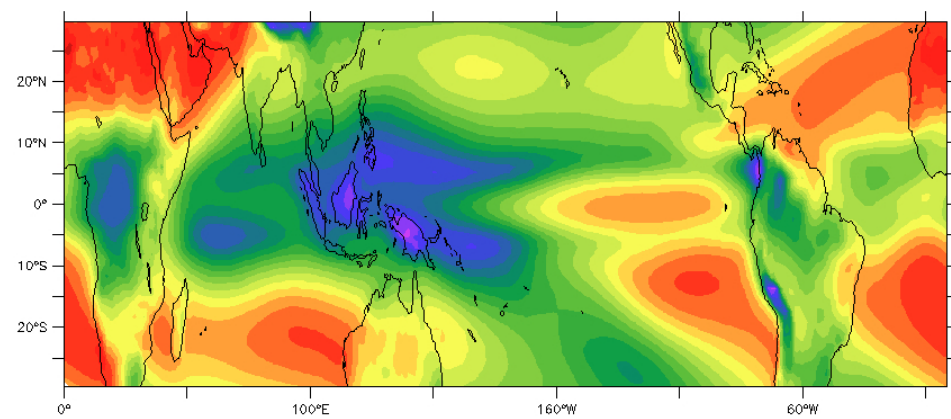
(b) RCP8.5 21st century forced CCSM4 run

Figure 3.7: Annual mean Outgoing Longwave Radiation for (a) the 20th century forcing simulation and (b) RCP8.5 21st century simulation. The period used to calculate for both cases were the last 50 years from each century.
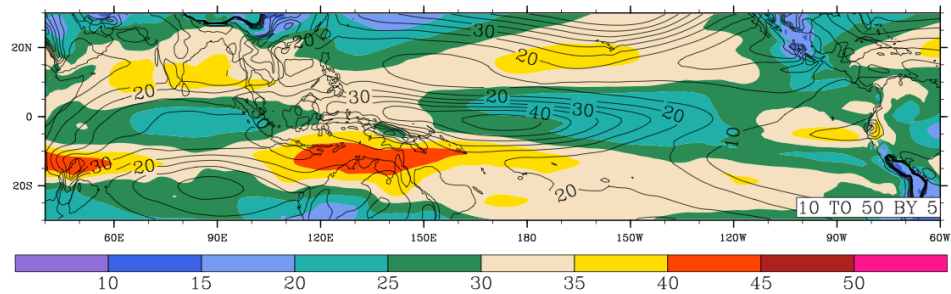
(a) 20th century run
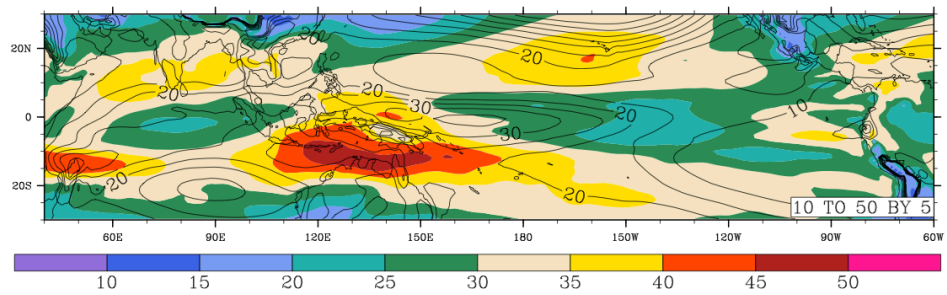
(b) 21st century run

Figure 3.8: Total variance in the zonal 850 hPa winds (line contours) and percentage variance explained by the Intraseasonal Oscillations (color contours) for (a) the 20th century simulation and (b) the 21st century simulation.
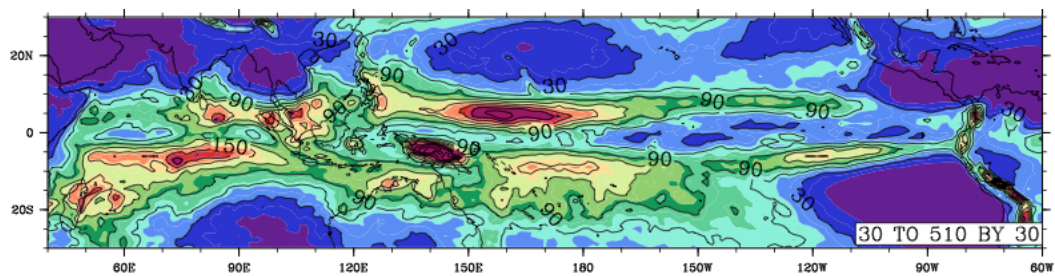
(a) 20th century run
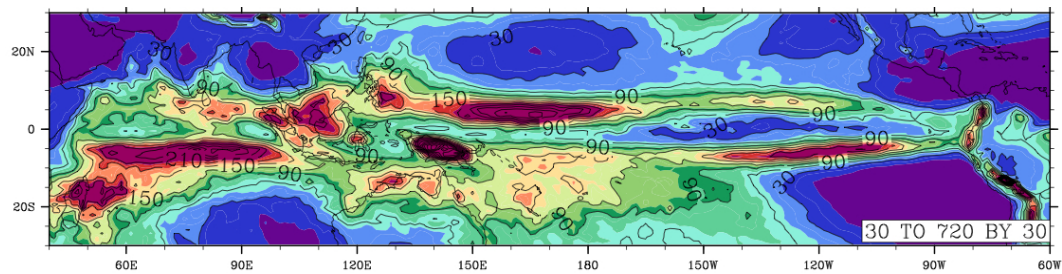
(b) RCP8.5 21st century run

Figure 3.9: Total precipitation variance for 50 years of (a) 20th century simulation (b) 21st century simulation (RCP8.5 case).
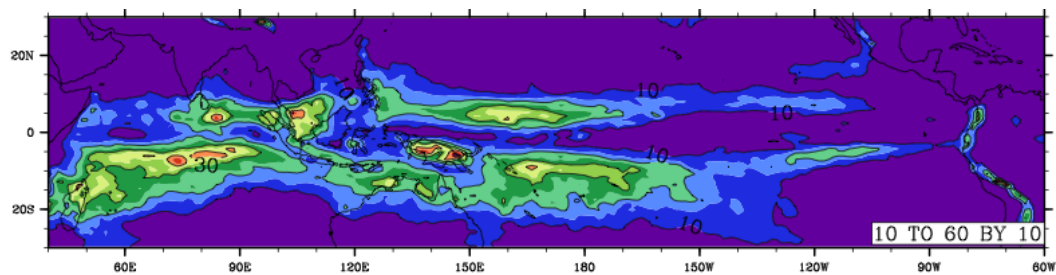
(a) 20th century run
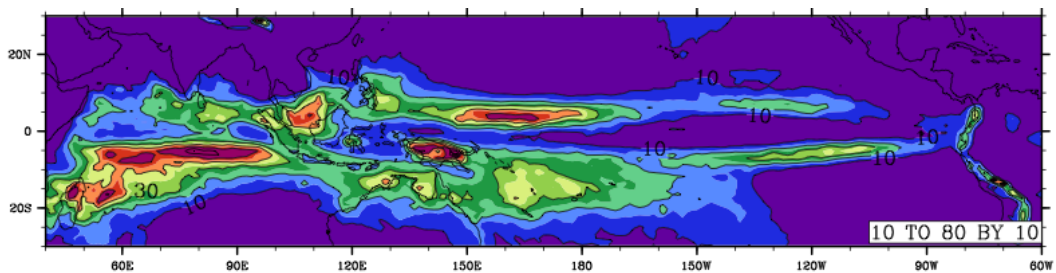
(b) 21st century RCP8.5 run

Figure 3.10: Percentage variance of Intraseasonal precip in the (a) 20th century run and (b) 21st century run. The contours are drawn for every 10 % increase in variance explained by the intraseasonal precipitation.
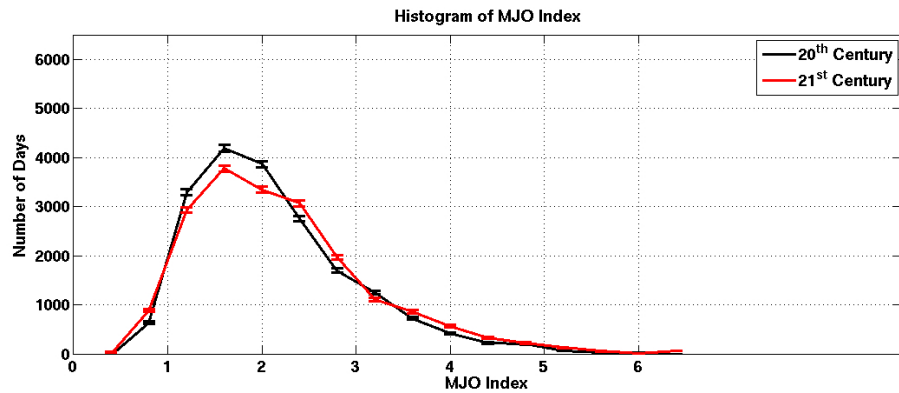
(a)
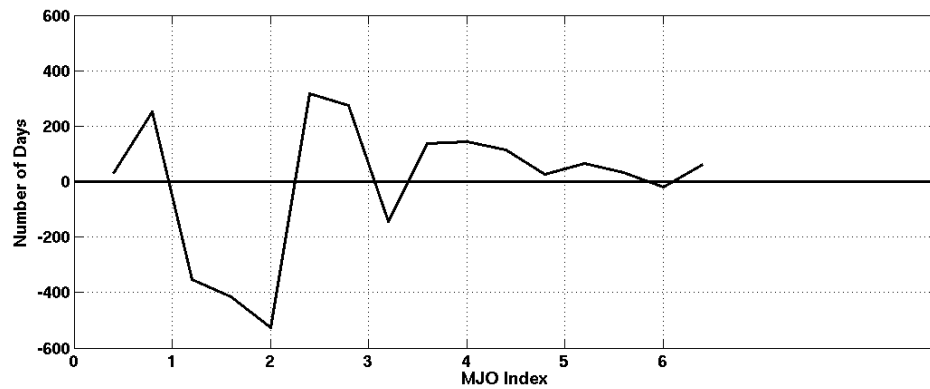
(b)

Figure 3.11: MJO Activity in the present vs future climate of RCP8.5 scenario. The number of days that the MJO is active at a certain MJO amplitude is plotted as a line histogram in (a). The difference between the Present and Future MJO active days for each amplitude is plotted in (b).
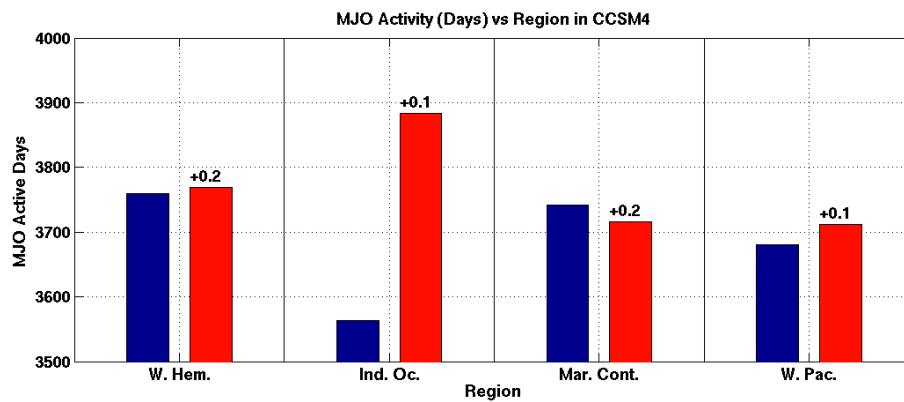
(a) Number of MJO active days in CCSM4 (blue : present climate , red : future climate)

Figure 3.12: Number of MJO active days in CCSM4, present climate (blue) compared to the future climate (red). The difference in mean amplitude (RCP8.5 - 20th century) is indicated on top of the red bars. The change in amplitude is always positive indicating that the average amplitude of the MJO is increasing in the future climate.

Table 3.1: Percentage of days of active MJO during different phases of the zonal shear (quantified by Webster-Yang Index) in the Northern Indian Ocean and the average amplitude of the MJO is shown during these different phases.

	% MJO Days (CCSM4)	(Obs.) (Obs.)	MJO avg. amp. (CCSM4)	(Obs.) (Obs.)
Positive WYI	48	58	2.9	3.0
Neutral	40	36	2.7	2.7
Negative WYI	65	51	2.7	2.8

Table 3.2: Regression coefficient for MHI and Nino 3.4 and WYI and Nino 3.4

	Reg. Coeff. (CCSM4)	(Obs.)	Intercept (CCSM4)	(Obs.)	R^2 (CCSM4)	(Obs.)
MHI	-0.4	-0.2	0	0	0.4	0.3

Chapter 4

State Estimation applied to the Oceanic Mesoscale in the South East Pacific

This chapter builds the background for the second half of this thesis and discusses the development of assimilation methodologies in physical oceanography. It presents the mathematical recipe of the assimilation method adapted in the present study and also illustrates the implementation of assimilation of observed data over the oceans in a general circulation ocean model (ROMS). The Peruvian Current system plays a key role in the climate variability of the Eastern Tropical Pacific and also has teleconnections to other regions of high climate impact like the Tropical Pacific. The oceanic circulation is characterized by strong eddy activity with short zonal scales. Mesoscale eddies generated in the upwelling regions in the South East Pacific are studied in an ocean data assimilation framework. Data assimilation of the sea state observations from satellites and ships for a period of a month in 2008 is achieved by using the inverse Regional Ocean Modeling System (iROMS), a 4D-variational data assimilation system. The 15-day ROMS I4D-VAR simulations successfully improve the state estimation by adjusting the initial conditions and the surface forcing. The normalized absolute misfit between the observations and the corresponding model states is reduced close to the observational error range. Other statistical measures comparing model with observations are also improved.

4.1 Introduction

"Assimilate" is a word that conjures up diverse meanings ranging from physiological metabolism to absorption of knowledge into the mind. Its usage in all contexts is in the sense of absorption of knowledge/nutrients external to the system into the present state of the system. In recent years, interest in data assimilation into ocean models has increased dramatically after the increase in available observational data of oceanic fields and the concomittant development of more accurate ocean general circulation models. In this new age sophisticated theories about ocean circulation developed up till now from very little field information, will be tested against the incoming data, new theories will be developed to explain the varied phenomena transpiring from the more plentiful data and increased understanding of ocean circulation will be translated into prediction. The concept of data assimilation was developed in meteorology about 50 years ago as the methodology in which observations are used to improve the forecasting skill of operational meteorological models. In operational meteorology, all the observational data available at a given time are assimilated into numerical prediction models by melding them with the model-predicted values of the same variables in order to prepare initial conditions for the forecast model run.

In the ocean state estimation context, the term "data assimilation" has acquired a much broader meaning. Data assimilation in ocean state estimation pertains to various different methodologies, originating not only from meteorology but also from solid earth geophysics inverse theories and in engineering control theories. All these methods attempt to constrain a dynamical model with the available data. Oceanographic data assimilation has three main objectives. One goal is to quantitatively use the data in order to improve the ocean model parameterizations of subgrid scale processes, boundary conditions, etc. A second goal is to obtain a four-dimensional realization of the oceanic flow that is simultaneously consistent with the observational evidence and with the dynamical equations of motion. This realization can be used for detailed process studies of ocean dynamics of a region. A third major motivation of ocean data assimilation, the closest to the meteorological one, is to provide initial conditions for predictions of the oceanic circulation.

In this chapter, we intend to illustrate the data assimilation scheme used in the study of this thesis along with certain illustrations of the landmarks in the development of ocean data assimilation. The data assimilation scheme used in this study is termed as Incremental Strong-constraint 4 Dimensional Variational (IS4DVAR) assimilation. Our main focus here is the mathematical framework based on which the IS4DVAR methodology was developed and the objective of using data assimilation in a ocean general circulation model. Two major differences still prevent the simple "borrowing" of techniques from meteorology. The first is the motivation for oceanic data assimilation which is not as narrowly focused towards short term prediction as are most meteorological efforts. The second reason resides in the major differences between the meteorological and oceanographic data sets. The available oceanographic data are sparse in the interior of the ocean where as the surface measurements of oceans are much more spatially dense. This is not the same in the case of meteorological observations. This implies that the assimilation methodologies, far from being blindly applied to oceanic dynamical problems, must be revisited and sometimes profoundly modified to make them feasible and successful for physical oceanography.

4.2   Historical Perspective

The first data assimilation methods were called the "objective analysis" (Cressman, 1959). The idea of applying objective analysis was first proposed by Kibel. In a lecture in 1949, Kibel pointed out that calculations of barometric and thermal tendencies according to the forecasting scheme developed by him at that time could be carried out quiet conveniently, provided the pressure and temperature fields were first represented by polynomials. In subsequent works, Kibel made use of formulae which described a plane field by means of a quadratic and third order polynomials, on the basis of the method of least squares and using data from points on a square grid.

At the end of 1949, Panofsky's article (Panofsky, 1949) appeared, in which the term "objective analysis" was apparently used for the first time. He used a

technique of fit by least squares in two dimensions. This technique consists basically in expanding the fields (variables), which are to be analyzed, in a series of polynomials about the observation point, minimizing the square of their differences with the observed values. The expansion coefficients are then determined by inverting a matrix.

The studies described above were carried out before numerical prediction by means of electronic computers began to be used in meteorology. The introduction of the latter provided a powerful stimulus to the developement of objective analysis methods. Consequently, the main attention began to be focused just on obtaining values of the analyzed elements at regularly spaced grid points (values to be used afterwards as initial data for the numerical prediction) rather than on a construction of the whole field.

This was followed by the developement of two fundamentally different methods of objective analysis for the purpose of numerical weather prediction. One was developed by American investigators Gilchrist and Cressman (Cressman and Gilchrist, 1954) and the other by Bergthorsson and Döös (Bergthorsson and Döös, 1955). Gilchrist and Cressman developed a polynomial interpolation scheme termed as "successive correction scheme". It achieves its results by forcing convergence of data to observed, interpolated values using multiple iterations.

Swedish investigators Bergthorsson and Döös developed a completely different method of objective analysis. The information used in this method includes not only observational data but also the results of a numerical prediction for the given time and the average climatological values of the analyzed elements.

The breakdown in the field of data assimilation was achieved independently by Ed Lorenz (1956) and L. S. Gandin (1965) who introduced the "statistical interpolation" (or "optimal interpolation") method. This method is a 3D data assimilation scheme and is a kind of "regression analysis", which utilizes the information about the spatial distributions of covariance functions of the errors of the "first guess" field (previous forecast) and "true field". These functions are never known. However, different approximations were assumed.

The optimal interpolation algorithm is the reduced version of the Kalman

filtering algorithm, when the covariance matrices are not calculated from the dynamical equations, but are pre-determined in advance.

When this was recognised, the attempts to introduce the Kalman Filtering algorithms as a 4D data assimilation tool for Numerical Weather Prediction models were tried. However, this was (and remains) a very difficult task, since the full version of Kalman Filtering algorithm requires solution of the enormous number of additional equations. In connection with that, the special kind of Kalman Filtering algorithms (sub optimal Kalman Filtering) for Numerical Weather Prediction models were developed (Dee, 1991a).

Over the past 25 years or so, since the initial efforts to develop three dimensional ocean circulation models (Bryan, 1969), ocean modeling has made a very significant progress. In parallel, oceanic observational techniques have been thoroughly revolutionized. However, the lack of a single focusing motivation of oceanic data assimilation such as provided by the need for Numerical Weather Prediction (NWP) in meteorology, caused ocean models and observational techniques to develop quiet independently from each other. When oceanic models and observations started converging, it happened in different paths, depending on the specific objectives of each effort (Emery and Thomson, 1998).

The early days of oceanography saw dynamic calculations as the main quantitative tool to combine data (temperature and salinity) with the then present ocean models. From this modest beginning, relying on highly simplified models and on no formal assimilation procedure, the next step was to introduce a formal least square inverse methodology imported from solid earth geophysics and add the tracer conservation constraints in order to solve the problem of level of no motion (Wunsch, 1977; Wunsch and Grant, 1982). This was done in the framework of coarse resolution box models whose dynamics were still very simple although the inverse methodology used was very general. Much of the work done at present on the combination of OGCMs and data stems from the experience obtained in the pioneering work on oceanographic box inverse models.

As the complexities of the models grew, equally more sophisticated assimilation methods needed to be developed. Efforts towards this began with the

diagnostic models in which temperature and salinity data were simply inserted into the dynamical equations of fairly complex ocean models in order to evaluate the velocity field (Holland and Hirschman, 1972). The results were very poor due to model-data-topography inconsistencies, and at the next stage, a very simple assimilation methodology was introduced into OGCMs and became known in the oceanographic context as the "robust diagnostic" approach (Sarmiento and Bryan, 1982). The same approach had actually been introduced earlier in meteorology as the "nudging" technique (Anthes, 1974) and the term "nudging" has by now become commonly used in oceanography as well. In this approach, there is no effort to introduce least-square optimality, and the data are just used to nudge the model solution towards the observations at each time step through a relaxation term added to the model equations. The result is far superior to simple diagnostic models, but leaves much to be desired due to the inability to use the information about data uncertainty or to estimate the errors in the solution obtained (Holland and Malanotte-Rizzoli, 1989; Malanotte-Rizzoli and Tziperman, 1996; Malanotte-Rizzoli and Young, 1995; Lermusiaux and Robinson, 1999; Lu and Browning, 1998).

As the objectives of modeling and observational oceanography began to converge, more formal least-square methods taken from meteorology were also used in ocean models, in particular the Optimal Interpolation (OI) method (Mellor and Ezer, 1991; Derber and Rosati, 1989; Ezer and Mellor, 1994). OI may be viewed as a nudging technique in which the amount of nudging of the model solution towards observations depends on the data errors, while also allowing to make error estimates for the solution. This approach, developed in meteorology for NWP, is not capable of improving model parameters or parameterizations, nor is it capable of fitting the entire four dimensional distribution of observations simultaneously to the model solution.

Carrying the least squares approach for a time dependent model to its rigorous limit, leads to the "Kalman filter/smoother" assimilation methodology, which is capable of assimilating data into a time dependent model while assuring least-square optimality, full use of a priori error estimates, and calculation of the

covariance error matrix for the model outputs. Apart from the fact that the Kalman filter is a formally optimal technique in the least-square sense only for linear models, its high computational cost limits its use at present to simple models, or very coarse OGCMs. Recent developements are directed at developing efficient, even though sub optimal, variants of the Kalman filter that allow the use of a full nonlinear OGCM with this method (Lewis et al., 2006).

The ultimate goal of combining a formal least-square optimization approach with a full complexity OGCM requires the simultaneous solution of hundreds of thousands of coupled nonlinear equations (the model equations at all grid points and all time steps), and therefore requires an efficient approach which can be found in the "optimal control" engineering literature.

The development of assimilation methods in physical oceanography has always seemed to trail behind meteorology by a few years. This lag is in spite of the fact that the ocean and atmosphere, even though characterized by some important differences, are at the same time similar enough that they can be treated with the same theoretical approaches and methodologies. It is important, therefore, for the ocean modeler to try and understand the reason for this difference in rate of developement of data assimilation methodologies in order to be able to isolate potential obstacles for their future use in oceanography.

Clearly, a primary reason for the delayed developement of oceanic data assimilation was the lack of urgent and obvious motivation such as the need of forecasting the weather and of producing better and longer forecasts as in meteorology. This situation has changed rapidly over the last few years with the role of oceans in the climate being understood better which entailed a better ocean state estimation. This in turn necessitated a systematic model improvement. This has become the main motivation to develope a robust data assimilation platform for ocean models. The need for ocean prediction is also arising now on various temporal and spatial scales, from climate change predictions, through regional forecasts of the large scale ocean climate variability, e.g. of the North Atlantic thermohaline circulation (Carton and Hackert, 1990; Gordon, 1986) or El Nino in the Pacific Ocean, to a few weeks regional mesoscale ocean forecasts in frontal regions

such as the Gulf Stream system that are required for example by various Naval applications.

The most profound limitation on the developement of oceanic data assimilation may have been, however, the lack of adequate data sets. The number of available oceanographic observations is far smaller than the number of meteorological observations, especially when the different temporal and spatial scales are considered. It is estimated, in fact, that the number of presently available oceanographic observations is smaller that its meteorological counterpart by several orders of magnitude (Ghil et al., 1997; Ghil and Malanotte-Rizzoli, 1991).

New oceanographic data sets, nearly comparable to the meteorological one, i.e. synoptic and with global coverage, are however becoming available. This oceanographic observational revolution of the 90's has been made possible by the advent of satellite oceanography. A second worldwide major source of oceanographic observations is the World Ocean Circulation Experiment and the Argo project that, through basin wide hydrographic sections, meridional and zonal, should provide us with a picture of the large scale global circulation in the World Oceans in the 90's and the first decade of the 21st century.

Thus, the increased availability of observational data and increased need for data assimilation has necessitated and expedited the process of developing advanced data assimilation techniques to reap the full benefits of the data sets and models combinedly (Bennett, 1992; Anderson et al., 1996; Malanotte-Rizzoli and Tziperman, 1996; Anderson and Willebrand, 1988; Tziperman et al., 1992; McIntosh, 1977).

4.2.1   Objectives of Oceanographic Data Assimilation

The three main objectives of combining data and complex OGCMs are: model improvement, study of the dynamical processes through state estimation, and, finally, ocean/climate forecast. Each of these objectives has been met with relevant assimilation methodologies respectively. Even the highest resolution ocean circulation models cannot resolve all of the dynamically important physical processes in the ocean, from small scale turbulence to basin scale currents. There

will always be processes that are not represented directly, but rather are parameterized. These parameterizations are sometimes simple, often complicated, and always uncertain both in form and in the value of their tunable parameters. The models are very sensitive to even small changes in these parameterizations. A few examples of such parameterizations are that of the small scale vertical mixing in the ocean interior (Bryan, 1987), the mesoscale eddy parameterizations in coarse ocean models used in climate studies, of mixed-layer dynamics (Mellor and Yamada, 1982), and of deep water formation (Schott and Send, 1994). Another set of uncertain yet crucial parameters corresponds to the poorly known surface forcing by wind stress, heat fluxes and evaporation and precipitation, all of which are subject to typical uncertainties of 30-50% (Trenberth, 1989; Trenberth and Solomon, 1993).

One of the most important goals of ocean data assimilation is to use available observations of the oceans systematically and quantitatively in order to test and improve the various uncertain parameterizations used in OGCMs. A good estimate of these parameters would allow the models to predict the ocean state more accurately in the absence of available data, which is the ultimate goal of ocean models: To be able to forecast the ocean state in the absence of any available observational data during forecast runs.

Improvement of internal model parameters and boundary conditions via data assimilation can be complemented by the state estimation of the ocean via data assimilation (Killworth et al., 2001). In ocean state estimation via data assimilation, the model deficiencies are compensated for by using data to force the model nearer to observations during the model run (Woodgate and Killworth, 1997).

4.2.2 The data assimilation model

Data assimilation of the VOCALS-REx cruise time intervals will be achieved using the Incremental Strong-constraint 4D-variational (IS4DVAR) data assimilation system for high-resolution basin-wide and coastal oceanic flows (Moore et al., 2004). The assimilation is performed under the perfect model assumption (strong

constraint) as we intend to diagnose physical balances during the VOCALS cruise survey period. IS4DVAR has been tested by Di Lorenzo et al. (2007) in an idealized 3D double gyre circulation and in a realistic application for the geometry and bathymetry of the Southern California Bight (SCB), a region characterized by strong mesoscale eddy variability like the SEP. Synthetic data for sea surface height, upper ocean (0-500m) temperatures, salinities and currents were assimilated over a period of 3 days. The model first guess, prior to assimilation, was initialized using climatological conditions. The assimilation solution for the strong constraint experiment successfully reduced the initial model observation misfit by 75% and improves the model fields also at locations where observations are not assimilated.

The goal is to, in a least-squares sense, perturb the circulation to minimize the difference between the observations and model circulation in the new estimated state of the ocean. IS4DVAR produces a new state by correcting the initial conditions. The evolution of the model state is seen to be close to the observations in the assimilation window and to be dynamically consistent at the same time. In order to get the new initial ocean state, $\mathbf{x}(0) = \mathbf{x}_b(0) + \delta\mathbf{x}(0)$, we first define the cost function in terms of $\delta\mathbf{x}(0)$, which is the combination of two terms; changes in the initial model states (J_b) and residuals from observations (J_o). It is defined below.

$$
J(\delta\mathbf{x}(0)) = \underbrace{\frac{1}{2}\sum_{i=1}^{N}(\mathbf{H}_i(\mathbf{x}_b(0) + \delta\mathbf{x}(0)) - \mathbf{y}_i)^T \mathbf{O}_i^{-1}(\mathbf{H}_i(\mathbf{x}_b(0) + \delta\mathbf{x}(0)) - \mathbf{y}_i)}_{J_o} +
$$

$$
\underbrace{\frac{1}{2}\delta\mathbf{x}(0)^T \mathbf{B}^{-1}\delta\mathbf{x}(0)}_{J_b}, \tag{4.1}
$$

where $\mathbf{B}$ is the background error covariance matrix, vector $\mathbf{y}$ is observations, $\mathbf{H}$ is the tangent linear model which integrates the states linearly and then projects to the observational space, $\mathbf{O}$ is the observational error covariance matrix and N is the number of observation time steps.

The solution will minimize the cost function. This means that it will make

both the residuals and the changes in the initial states small. The optimal solution for $\delta \mathbf{x}(0)$ satisfies

$$\nabla_{\delta \mathbf{x}} J = \mathbf{B}^{-1} \delta \mathbf{x}(0) + \sum_{i=1}^{N} \mathbf{H}_i^T \mathbf{O}_i^{-1} \left(\mathbf{H}_i \left(\mathbf{x}_b(0) + \delta \mathbf{x}(0) \right) - \mathbf{y}_i \right) = 0. \qquad (4.2)$$

This solution of $\delta \mathbf{x}(0)$ will give us the optimal initial condition that can be used to derive the model state evolution with the least misfit with observations.

4.3   Ocean dynamics in the Southeast Pacific

The dynamics of mesoscale ocean eddies in the SEP region are explored in this modeling study which will aid in the diagnosis of the VOCALS observations and will help us to understand the mechanisms that control the interactions of the variability of the ocean eddy fields and heat fluxes in the VOCALS domain. Observed mesoscale oceanic surveys of the VOCALS campaign are used in data assimilation experiments to diagnose the dynamics and sensitivities of the ocean circulation fields. Data assimilation fits of the VOCALS hydrographic surveys (and concomitant data) will provide crucial dynamically consistent diagnostics of the circulation for interpreting the relation between physical variables, atmospheric variables and biology.

This research focuses on the mesoscale dynamics of the ocean in the South East Pacific (SEP). Mesoscale eddies generated in the upwelling regions along the west coast of South America, which affect the distribution of sea-surface temperature (SST) in the SEP are studied in an ocean data assimilation framework.

The Andes mountains channel strong southerly winds along the coast generating vigorous coastal upwelling (Garreaud and Muñoz, 2005). Complicated ocean currents, eddies, and waves re-distribute the cold water more than a thousand kilometers offshore. The cool water helps maintain the low-level clouds, whose shade helps keep the waters cool (Klein and Hartmann, 1993). The cloud formation depends on aerosols, which are produced both by ocean biology (which is dependent on upwelled, recycled and transported nutrients) and by human industrial

activities along the coast (Bretherton et al., 2004). Some of these feedbacks are common to other subtropical stratocumulus regions, such as the California Coast. But these feedbacks are of particular interest in the SEP because of this regions importance in controlling the mean and transient properties of equatorial climate, and its consequent teleconnections to midlatitudes (Xie et al., 2007). Indeed, the climate biases that occur in global coupled climate models are especially severe here in the SEP. For example, warm biases of 2-4K occur along the west coast of South America in the NCAR CCSM3 (Fig 4.1), and similar biases occur in other eastern boundary currents regions. Our imperfect understanding of these feedbacks and of how to represent them in large-scale numerical models affects the skill of climate predictions on all time scales (Mechoso et al., 1995).

4.4   Model configuration and experimental setup

The Regional Ocean Modeling System (ROMS) four-dimensional variational data assimilation (4DVAR) system (Moore et al., 2011) was used to estimate the ocean states for August to November 2008. The model domain covers 13S to 27S and 67W to 90W with an approximately 7km grid interval. Figure 4.2 shows bathymetry in the domain with a tall ridge in the middle of the domain that makes the water depth as shallow as 1500 - 2000 m. The model has 32 terrain-following vertical levels that are concentrated more at the surface as shown in the Figure 4.2. Background initial were extracted from the ocean model data set by Combes et al. (2009), for August 2008 and the lateral boundary conditions were given from the OCCA data set (Forget, 2010). The surface boundary conditions were given from ECMWF Interim air-sea flux data using bulk formulation (Fairall et al., 1996) and QuikSCAT wind data, which has a resolution of 25 km.

The ROMS 4DVAR collects observations over a defined assimilation time window and can adjust the initial condition, surface forcing, boundary condition and model itself with given errors. In this experiment, data assimilation has been done using SST data from the 10 km resolution blended Advanced Very-High-Resolution Radiometers (AVHRR) on the Polar Operational Environmental Satel-

lite (POES) and Advanced Microwave Scanning Radiometer (AMSR-E) on Aqua, SSH anomaly data produced by Ssalto/Duacs and distributed by AVISO, hydrographic T and S from the VOCALS program CTD casts (Figure 4.3), Argo profiles. The fit is achieved by adjusting the initial condition and surface forcing to allow the model simulation to fit the observed data in a least square sense.

We set the assimilation window to be two fifteen day periods, which guarantees a dynamically balanced ocean state for the experiment time period. The 4DVAR in most realistic atmospheric and oceanic models uses iterative methods to find the optimal states because the size of dimension often prohibits the matrix inverse calculation in the solution. In these experiments, we used 45 iterations total, and this was adequate for the convergence of the solutions. Figure 4.4 shows the reduction of the cost function after each loop (outer and inner) during the two 15 day fits respectively. Normalized absolute error (NAE) reduction for the total assimilation period is shown in Figure 4.5. If the NAE is one, it means the misfit between the observation and the interpolated model states is the same as the observational error. This would mean that the model state at the observation locations is indistinguishable from the observations within its error bar. In the Nov 15 - Nov 30th 2008 ocean state estimate the mean NAE became roughly one after ROMS 4DVAR system decreased the normalized misfit by 70% on average.

4.5 Observational data

Remotely sensed data

Sea Surface Temperature (SST) data are obtained from the 10km resolution blended product which combines Japan's Advanced Microwave Scanning Radiometer (AMSR-E) instrument, a passive radiance sensor carried aboard NASA's Aqua spacecraft, NOAA's Advanced Very High Resolution Radiometer, NOAA GOES Imager, and NASA's Moderate Resolution Imaging Spectrometer (MODIS) SST data set. Those satellites measure the SST twice a day, but the exact time of the measurement is obscured after the merging process. The minimum of the estimated observational error is set as 0.01^oC. Sea Surface Height (SSH) anomaly

observations are obtained from the data set produced by Ssalto/Duacs and distributed by AVISO. In the experiments, the assimilation efforts go to SSH anomaly correction for eddy activities instead of adjusting SSH. Thus, the along-track SSH anomaly data are added to the mapped temporal mean dynamic topography from the model. Then, the spatial mean of the observation is set to be the same as the model spatial mean. If the estimated observational error is smaller than 0.01m, it is fixed to 0.01m.

Hydrographic data

The subsurface temperature (T) and salinity (S) data are provided by CTD casts from the VOCALS cruise (Wood et al, 2008), and figure 4.3 shows the spatial coverage of the subsurface observations. The VOCALS program has measured T and S from the surface down to about 3500m or to the bottom if the ocean depth is shallower than 3500m for about 38 days. The measurement occurs roughly along the 20 S latitude with meridional cross sections in some places. The Continuous Underway CTD measures T and S at the same time. Argo floats can measure T and S from the surface down to 2000m. The horizontal distributions of the Argo floats keep changing as the floats drift freely in the currents. Except for the Argo floats that have their own error estimation, the observational errors for T are estimated in the same manner as the SST data. The observational errors for S are also one-quarter of the size of the model standard deviation, but the minimum value is set as 0.01 psu.

Processing of observations

If the observations have features whose scales are smaller than the model can represent, the reduction of the misfit may not be achieved through data assimilation. Hence, all observations inside of a certain number of grid cells are averaged with respect to the errors if they occur in the same time period. This super observations process eliminates all small-scale features in the observations that cannot be resolved by the model. Both super observations agree well with large-scale patterns in the SST with similar observation coverage, although the sharp

SST changes are only shown in the super observation with 1 x 1 grid cell. This also enables the assimilation window to be extended, because the highly nonlinear features by small scales are omitted in the fitting.

4.6 Assimilation results

Linearity

The ROMS 4D-VAR system is based on the tangent linear approximation. Thus, the length of the assimilation window is determined as the period when the linear assumption is valid. One of the possible tests for validation is to compare two model states: one is when δz is integrated by a tangent linear model M, and the other is the difference between two trajectories when z and z + δz are integrated by a fully nonlinear model. If these two states are near, the tangent linear approximation is valid. As expected, the smaller δz is, the longer the assimilation period that can be achieved (Veneziani et al., 2009b). Another possible test is to compare the cost function of the final inner-loop and the nonlinear cost function of the following outer-loop. If the system is linear, those two cost functions are identical. Figure 4.4 shows the changes in the cost function with iterations from the data assimilation experiment. The cost function $J(n)$ at nth iteration is normalized by the initial cost function $J(1)$. Although J_{NL} are higher than J at the previous iteration in all assimilation periods, the degree is negligible compared to the reduction of the cost function. The cost function converges. This indicates that the model state is close to the solution for the optimization problem. Hence, an additional iteration after the convergence of the cost function does not give much improvement.

Normalized absolute error reduction

The normalized absolute error (NAE) is useful to evaluate the ROMS I4D-VAR performance. It is a quantity to measure the distance between the observations and the model states normalized by the errors in the observations. If the NAE is below one, it means that the distance between the observation and the model

state is within the observational error range. It is worth noting that the optimal solution can have NAE > 1, because the solution is determined by the relative weight of the model and observation errors. The NAE changes for each variable are plotted in figure 4.5. The reductions of the NAE is shown in all variables from the assimilation experiment. The percentages of the reduction averaged over all variables are different in this period and is about 50 - 30 % for the variables. In general, the reductions of the NAE are greater when the initial errors are bigger . The SST has the biggest NAE both before and after the assimilation for the first 15 days and the SSH has the biggest error in the second 15 days. NAEs for other variables are reduced to approximately the observational error level. The updated model trajectory by ROMS I4D-VAR yields the least square-error over time and the variation of NAE should reduce after DA loops.

Taylor diagram

Taylor diagrams (Taylor, 2001) offer a way to compare the performances of several models with respect to the observations by showing their standard deviation, correlation, and the centered root-mean-square (RMS) difference. The centered RMS difference E' is given by

$$E' = \left[1/N \sum (f_n - \bar{f}) - (r_n - \bar{r}) \right] \tag{4.3}$$

$n = 1$ where N is the total number of observation, r and f are the observation state and model state at the observations location respectively. $\bar{f}$ and $\bar{r}$ represent the mean of f and r, respectively. If the model represents the observed states perfectly, it should have the same standard deviation as the observations. Also, the correlation between the model and the observation should be one, and the difference in RMS should be zero. Figure 4.6 shows the changes in normalized statistics for SSH, T and S on the Taylor diagrams for each assimilation period. In the diagrams, the observations are placed at the bottom of the diagram where the correlation coefficient is 1 and the normalized standard deviation is 1. The arrows indicate the changes in normalized statistics after data assimilation with the start of the arrow indicating the initial model state and the end of the arrowhead at the

location of the final model state after assimilation. SSH, T and S are shown with arrows in red, black and blue, respectively. The statistics for the background states show a few patterns that are consistent in both periods. The standard deviations of SSH and S are smaller than the ones in the observations, while the standard deviation of T is greater than the one in the observations. SSH has the smallest correlation coefficient in all periods. T and S have correlation coefficients higher than 0.8 in all periods. The RMS differences are smaller than 1 for all variables in all periods with the greatest value in SSH. The data assimilation improved the statistics for all variables in all periods. The arrows for all variables head to the observation point, meaning the statistics of variables become more similar to the observations. The improvements are obvious in the correlation coefficient and the RMS difference. In all cases, the correlation coefficients approach 1. The correlation coefficients for T and S are greater than 0.95 after data assimilation in all cases. The improved correlation coefficient for SSH is close to 0.9. The RMS difference improvements are also clearly seen in all cases. After data assimilation, the RMS differences for T and S are reduced to under 0.25 in all cases. Similar to the case of correlation coefficient, the improvements of RMS difference in SSH are not as great as in other variables, and the final normalized RMS differences are greater than 0.5. The standard deviations of the data-assimilated variables approach 1 in most cases, meaning their variabilities are similar to those of the observations. The standard deviations of T become close to 1 in both assimilation periods. The improvements of the standard deviation for S are seen in all periods. SSH standard deviation was improved in second half of the cruise period more than in the first half. It is interesting to observe that the final statistics for each variable have similar patterns in all cases independent of the background statistics.

4.6.1 Corrections to ocean state after assimilation

The previous sections showed the reduction in misfit of the model from observations through statistical quantities. Here a few figures depict the change in state after assimilation. Figure 4.7 and Figure 4.8 show the reduction in the misfit between the assimilated model and observations on the right panels compared to

the misfit of the initial model state before assimilation (shown on the left panel). The upper panels show the model temperature at the observation locations for the initial run without assimilation (left top panel), the observations (top middle panel) and the model temperature at the observation locations for the model run after assimilation. It can be seen that the upper level temperatures, especially close to the surface are improved much more than the ones below. This could be due to the increased constraint at the surface from surface observations too.

Figure 4.9 shows the improvement in the SSH and SST for Nov 10th, 2008 of the ocean state estimate after assimilation (on the bottom panels) compared to the initial state before assimilation. The SSH features, especially eddy-like sea level anomalies are changed drastically after assimilation. The ocean state before assimilation has much smaller features and eddies at different places compared to the observations. After assimilation, the negative and positive sea level anomalies in the model are roughly in the same place as in the observations. This indicates a marked change in dynamics of the ocean state estimate after assimilation. The SST features are also changed to reveal cooler SSTs over the low sea level anomalies in the assimilated ocean state estimate indicating cold core cyclonic eddies which are co-located along the same longitude and latitude as the ones in satellite altimetry. The SST after assimilation in the region of the cruise doesn't correlate very well with observations, since this temperature is also constrained by the subsurface profiles from the cruise tracks. The SST observations in this region, specifically derived from Infrared satellites are very sparse and have higher error in them due to the persistence of the stratus deck in the region preventing infrared measurements of SST. Hence, the ocean model is constrained more to the subsurface temperature data where both SST and subsurface temperature profiles are available.

4.7 Discussion

The powerful ROMS DA packages perform data assimilation on both model and observation space. The ROMS I4D-VAR used in fitting two 15-day periods in assimilation experiments searches for the solution of the optimization problem

in the primal space. Although dual space assimilation provides more diagnostic tools, the I4D-VAR allows us to do more effective computation as it has proven to give faster convergence of the cost function (Moore et al., 2011c).

15 day DA experiments over the PCCS have been successfully conducted for Nov 2008 using the observations from both remotely sensed data and in situ data. ROMS I4D-VAR reduced the normalized absolute error (NAE) near the observational error level for all variables except for the upper level temperature. The statistical information of SSH, T and S plotted in the Taylor diagram showed the improvement of the correspondence between the data-assimilated model states and observed states.

Data-assimilated ocean states have several applications. DA provides the estimations of the variables that cannot be measured directly. The estimations are from the dynamically balanced states and are expected to be more accurate than the one from the simulation without data assimilation. For instance, the heat transport, which has extreme importance in understanding the global heat budget, or the upwelling rate that significantly affects the ecosystem are both easily computed using the data-assimilated data set.

We assimilated the data from the VOCALS-REx cruise into a regional ocean model to derive an ocean state estimate of the structure of cyclonic and anticyclonic eddies in the SEP. VOCALS-REx UCTD profiles, Argo profiles, and satellite data were assimilated to derive an ocean state estimate during the cruise period.

Long term data assimilation fits have to be achieved for a more robust statistical study of the heat balance in the region. With only about 2 score CTD casts and 240 UCTD casts, constraining the whole 3 dimensional ocean for a long period was not feasible. We had to break up the one month of November 2008 into 2 15 day periods since the model does preserve linearity for the period of a month. Future assimilation experiments should consider having more subsurface observations available over a long time period to achieve a reliable long term ocean state estimate. This data set can then be used to look at eddy statistics and ocean heat balance and derive a more concrete result than achieved in this study.

Acknowledgments

Figure 4.1: Mean SST differences from observations for a) CCSM4 1° 1850 control, b) CCSM4 2° 1850 control and c) CCSM3 T85 1870 control. [Gent et al., 2011]
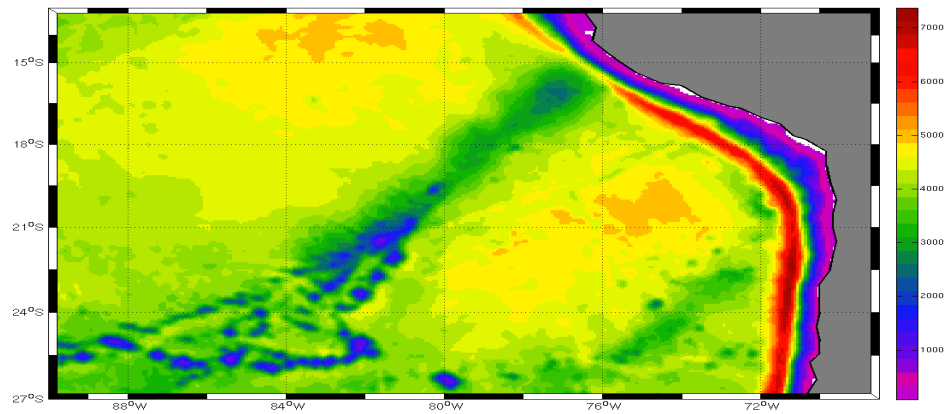
(a) Bathymetry
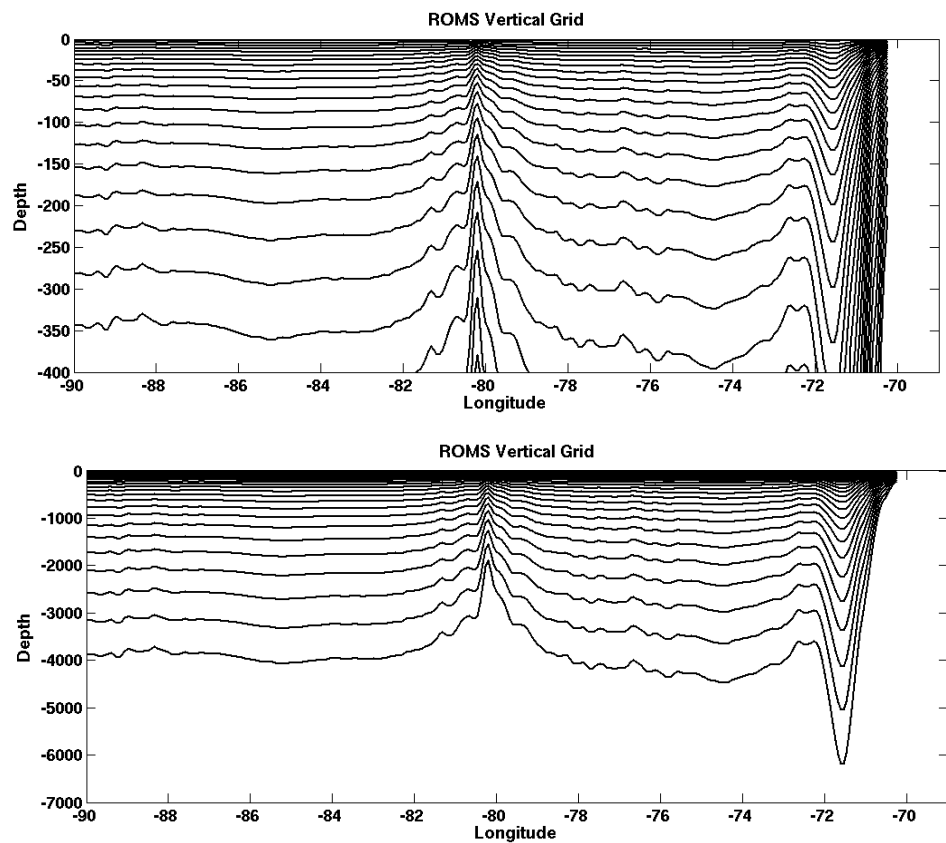
Figure 4.2: (a)Horizontal domain with the model bathymetry used for this experiment. (b) Vertical ROMS grid along 20 S in the domain with the upper panel showing a zoom in until 400 m and the lower panel showing the grid all the way to the bottom.
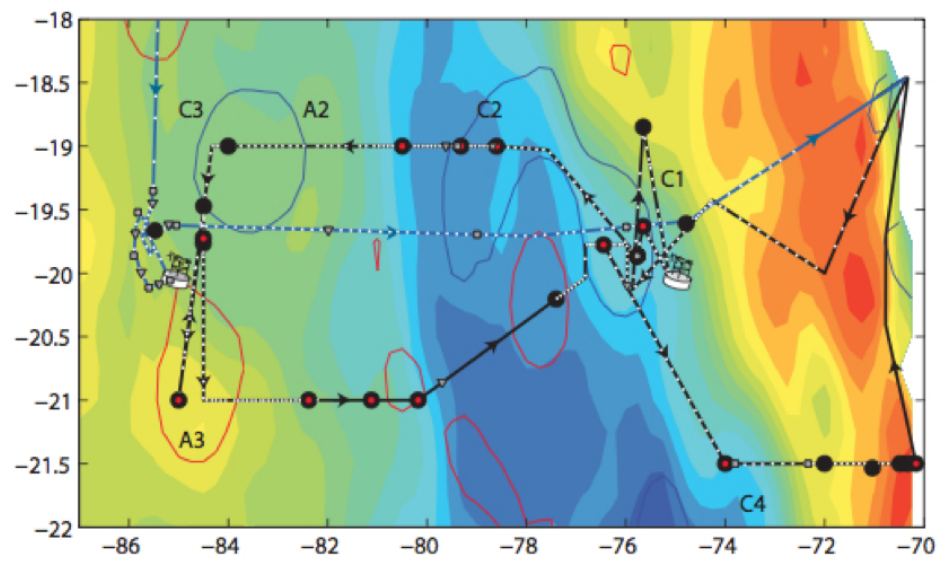
(a) Ron Brown Cruise track and SST

Figure 4.3: SST from merged satellite product during VOCALS cruise period.
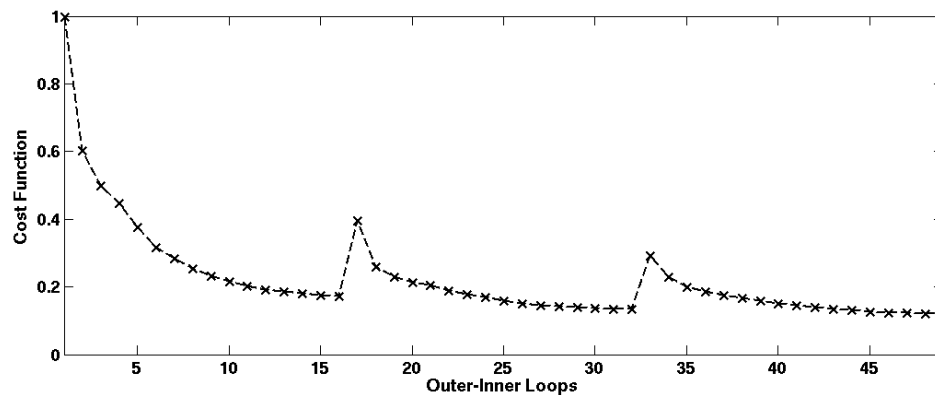
(a) Nov 1 - Nov 15
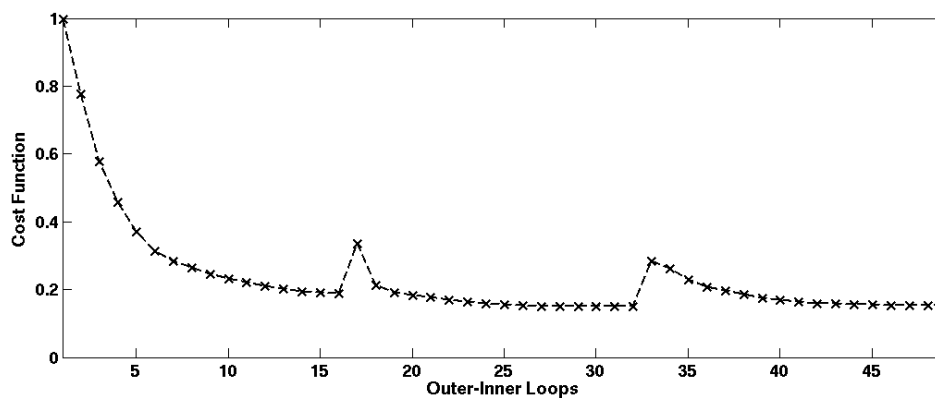
(b) Nov 16 - Nov 30

Figure 4.4: Cost Function for convergence for the two 15 day assimilation fits. (a) For the first 15 day fit for Nov 1 - Nov 15, 2008. (b) For the second 15 day fit for Nov 16 - Nov 30, 2008
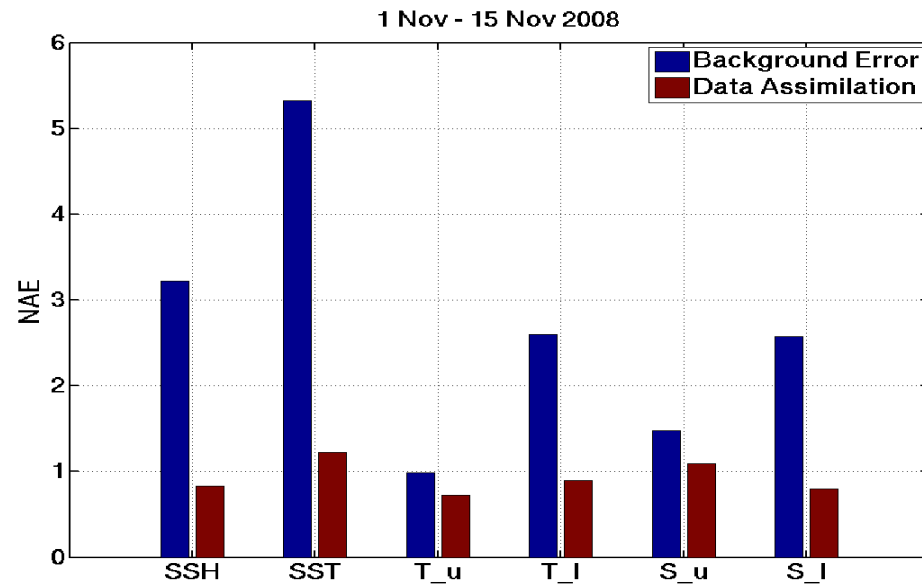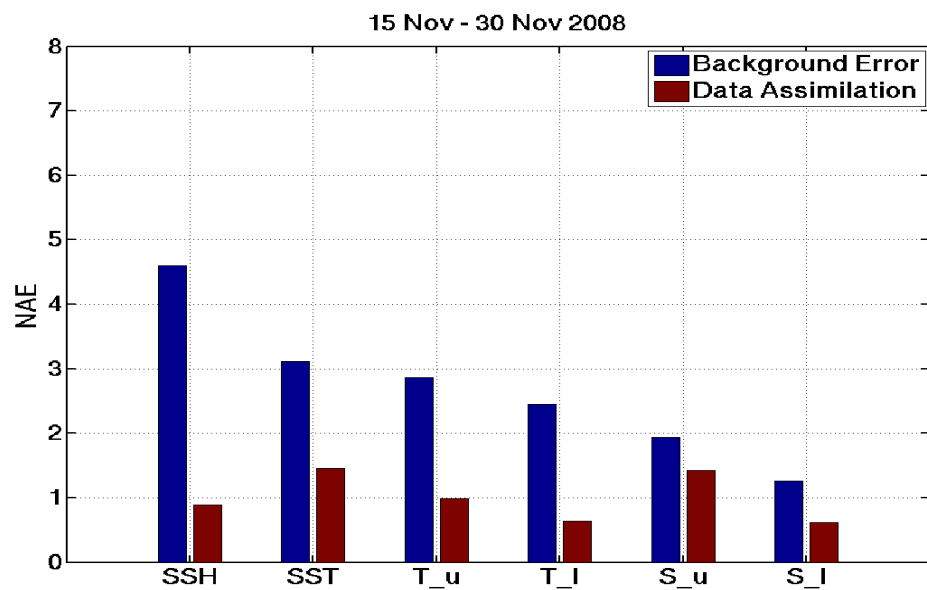
(a) Nov 1 - Nov 15

(b) Nov 16 - Nov 30

Figure 4.5: Normalized Absolute Error for the two 15 day assimilation fits. (a) For the first 15 day fit for Nov 1 - Nov 15, 2008. (b) For the second 15 day fit for Nov 16 - Nov 30, 2008
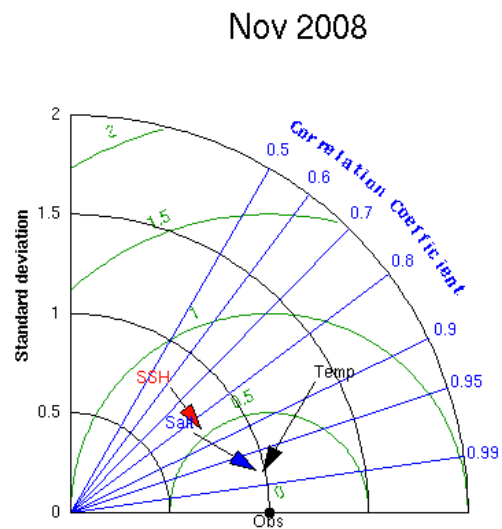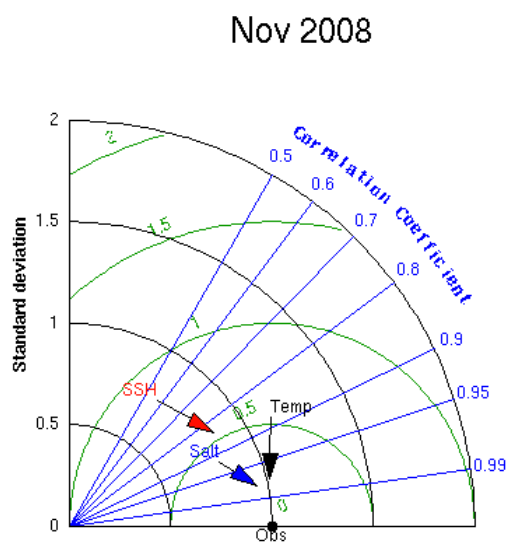
(a) Nov 1 - Nov 15

(b) Nov 16 - Nov 30

Figure 4.6: Taylor Diagram for the two 15 day assimilation fits. (a) For the first 15 day fit for Nov 1 - Nov 15, 2008. (b) For the second 15 day fit for Nov 16 - Nov 30, 2008

(a) Initial Profile Temp. in ROMS

(b) Observed CTD profiles of Temp.

(c) Final Profile Temp. in ROMS

(d) Initial Misfit in Temp. Profiles in ROMS

(e) Horizontal positions of Profiles

(f) Final Misfit in Temp. Profiles in ROMS
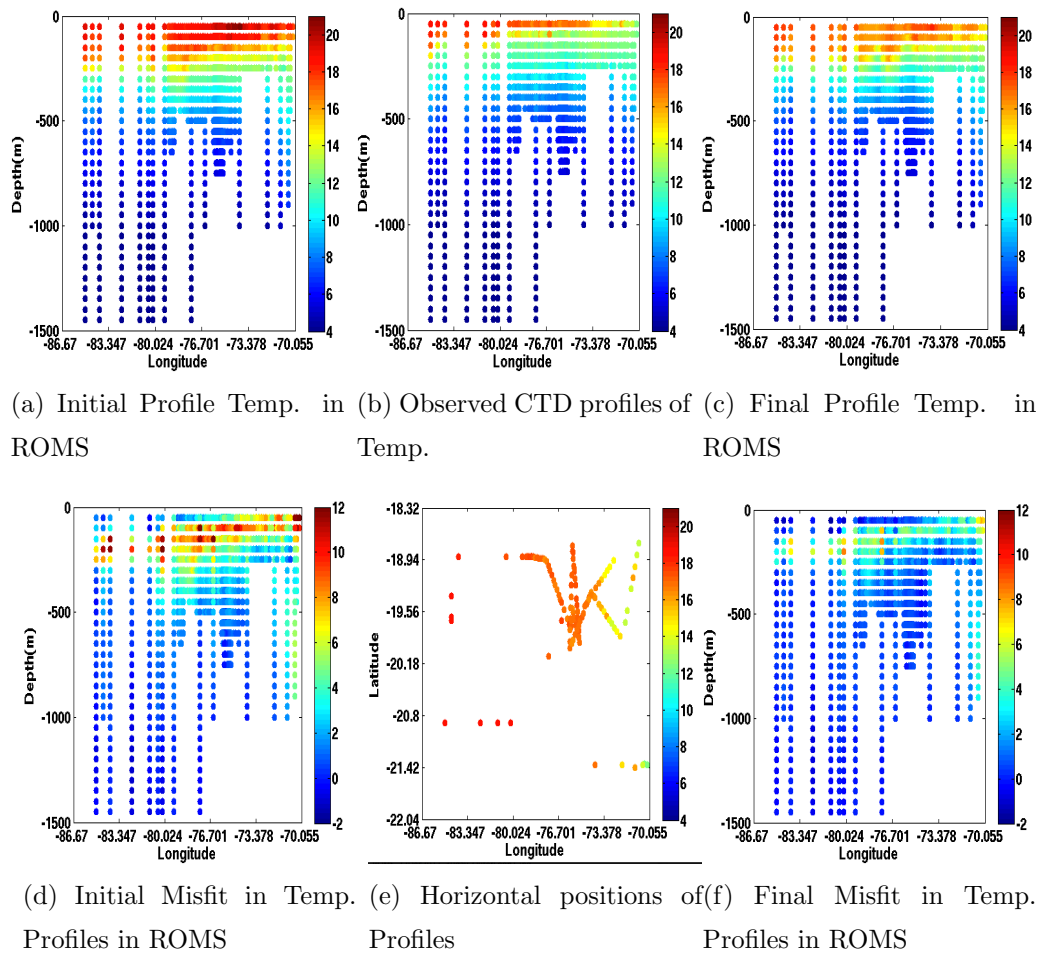
Figure 4.7: Initial and Final Model temperature values before and after assimilation compared to the assimilated profiles of temperature.
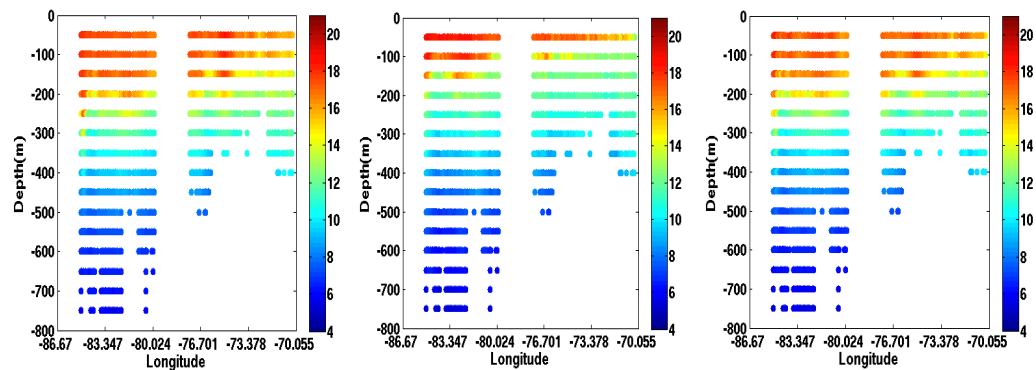
(a) Initial Profile Temp. in ROMS
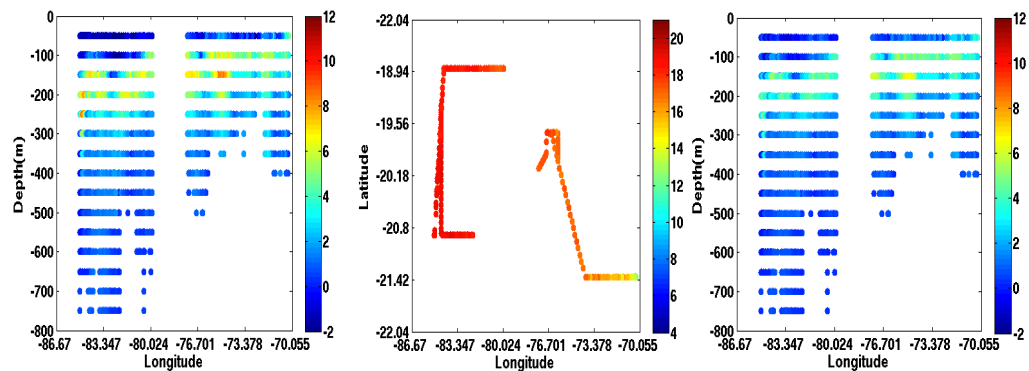
(b) Observed CTD profiles of Temp.

(c) Final Profile Temp. in ROMS

(d) Initial Misfit in Temp. Profiles in ROMS

(e) Horizontal positions of Profiles

(f) Final Misfit in Temp. Profiles in ROMS

Figure 4.8: Initial and Final Model temperature values before and after assimilation compared to the assimilated profiles of temperature.

(a) SLA Before Assim.

(b) SST Before Assim

(c) SLA Observations

(d) SST Observations

(e) SLA After Assim.
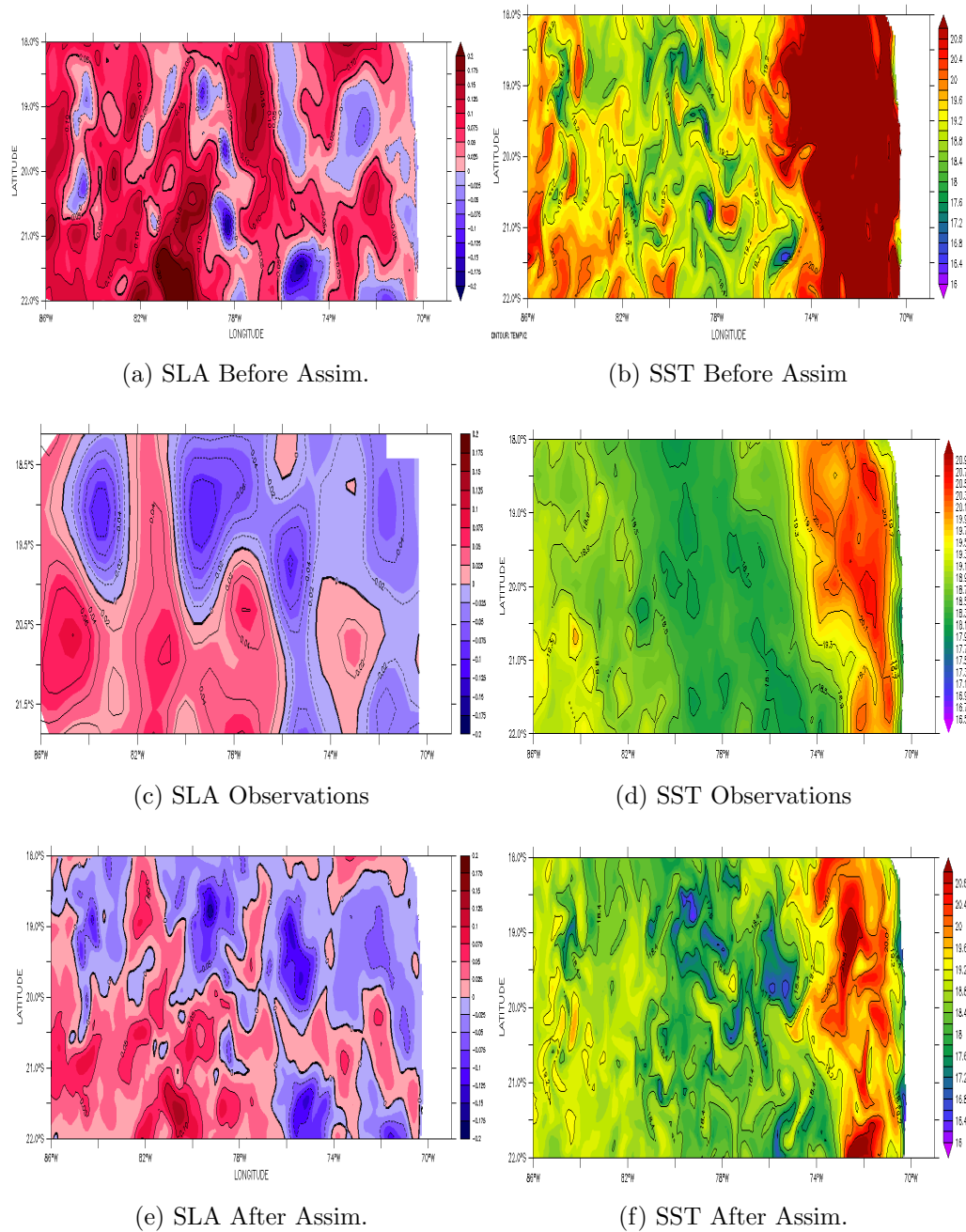
(f) SST After Assim.

Figure 4.9: Initial and Final Model Sea Level Anamoly (SLA) and Sea surface Temperature (SST) values before and after assimilation compared to the assimilated maps of Observed SLA and temperature.

Chapter 5

Structure and properties of eddies and a heat budget analysis in the Southeast Pacific ocean during VOCALS-Rex

Eddies are identified from the ocean state estimate along the track of the VOCALS-Rex cruise of 2008 and studied for their hydrography and velocity structure. Anticyclonic eddies (sea level anomaly highs) are characterized by depressed isopycnals within the eddy (in the upper 300m) and a warmer core in temperature than the surrounding waters. Cyclonic eddies (sea level anomaly lows) are characterized by shoaling isopycnals in the upper 300 m, colder temperature cores and a shallower salinity minima. An intensively surveyed cyclonic eddy was observed to have a subsurface velocity core diameter of about 50 km, as well as a cooler, salty core at a depth of about 150 m. The net temperature anomaly of the eddy was negative, including an anomaly of approximately -1 deg C at 100 m depth due to the doming of isopycnals within the eddy. A relationship between the eddy SLA and upper ocean temperature was sought from the model eddies during the cruise period. It is observed that all the model cyclonic eddies, the cores are significantly cooler than the anticyclonic eddies. It is also observed that the water mass prop-

erties of the core of the eddy has similar properties to that in the undercurrent close to the coast. Measurements and analyses show a mean net warming heat flux from the atmosphere to the ocean of 40-80 W m^{-2} over a wide cross-shore swath in the Southeast Pacific, and this warming has to be compensated by cooling since this region has one of the coldest temperatures at comparable latitudes around the globe. A heat budget analysis for the period of the cruise reveals that the advection is the predominant process that balances the surface heat flux and temperature tendency. Vertical diffusion is the second highest term balancing the heat budget with the horizontal diffusion being an order of magnitude smaller.

5.1 Introduction

The climate in the Southeast Pacific (SEP) near the coast of Peru and Chile is controlled by complex upper-ocean processes, marine boundary layer and land processes and their interactions. Coupled ocean-atmosphere processes involved in this tightly coupled system, and their variations have significant impacts on the global climate (Ma et al., 1996b; Miller, 1997; Gordon et al., 2010; Xie, 2004; Wood et al., 2011). For example, strong winds parallel to the coast generate intense coastal upwelling, bringing cold water to the ocean surface. This cool upper ocean water helps to maintain the persistent stratus/stratocumulus cloud decks by stabilizing the lower troposphere. These persistent stratus decks have a substantial impact on the surface energy budget in the tropics and subtropics by reflecting sunlight back to space.

Coupled atmosphere-ocean general circulation models (CGCMs) are well-known to have systematic errors in the SEP region, including a warm bias in SST and too little cloud cover (Mechoso et al., 1995; Ma et al., 1996b; Miller, 1997; Gordon et al., 2010; Kiehl and Gent, 2004; Large and Danabasoglu, 2006; Lin, 2007). These biases have important impacts on the simulated earth's radiation budget and climate sensitivity. Zheng et al. (2011) found that all 19 GCMs used in the Intergovernmental Panel on Climate Change (IPCC) Fourth Assessment Report had warm SST biases in the SEP. This bias limits models' abilities to simulate Earth's

climate. These biases are likely due in part to poor model representation of both upper-ocean heat transport and the surface heat budget (Large and Danabasoglu, 2006; de Szoeke et al., 2010; Zheng et al., 2010; Colas et al., 2011).

The main feature in the Southeast Pacific region is the Peru-Chile Current System (PCCS), also known as the Humboldt Current System. It is relatively complex, exhibiting several surface and subsurface currents. Its dynamics are principally controlled by the atmospheric South Pacific Anticyclone through Sverdrup dynamics. Near the South American coast, persistent equatorward winds drive upwelling cells leading to the highest biological productivity of the world ocean in terms of fish (Wood et al., 2011). Over the continental shelf, the upwelling of relatively cold deep water also gives rise to intense thermal fronts which separate, over short distances, cold coastal water from warmer and saltier subtropical water of the offshore ocean (Wyrtki, 1967; Strub et al., 1998). The PCCS is also characterized by two major subsurface poleward currents (Figure 5.8): the Peru-Chile Countercurrent and the Peru-Chile Undercurrent (PCU) which have been both traced back to the equatorial current system (McCreary Jr, 1985; Lukas, 1986; Tsuchiya, 1985; Strub et al., 1998; Montes et al., 2010a). The PCU which transports relatively warm and salty equatorial sub-surface water from the eastern tropical Pacific to at least 48^oS (Montes et al., 2010b) along the continental slope and shelf is a major source of the coastal upwelling off Peru and northern Chile (Leetmaa et al., 1987; Montes et al., 2010a). The oceanic circulation along the South American coast is also characterized by energetic mesoscale structures, the oceanic cyclonic and anticyclonic eddies (CEs and AEs, respectively). Such eddies have been mostly observed from altimeter data (Chelton et al., 2007; Chaigneau et al., 2008, 2011a), but they also have a signature in color satellite images (Correa-Ramirez et al., 2007) or in surface-drifter trajectories (Chaigneau and Pizarro, 2005). In the PCCS, CEs and AEs, which have a typical diameter of 150-300 km, are principally formed near the South American coast where they locally impact the heat and salt budgets through lateral turbulent fluxes (Chaigneau and Pizarro, 2005; Colbo and Weller, 2007). Then, CEs and AEs, which acquire a water mass structure typical of their formation region, propagate seaward with

translation velocities of few cm s^{-1} owing to a combination of mean flow advection and self-propagation. In this new environment, eddies appear as anomalous water masses with surface or subsurface temperature and salinity anomalies (Johnson and McTaggart, 2010) which are progressively redistributed to surrounding water during eddy decaying phase (Swart et al., 2008).

Although the main horizontal structure and kinematic properties of the PCCS eddies were investigated during the last decade, very little is known about their vertical structure and their impact on the heat and salt transports. Chaigneau and Pizarro (2005) have briefly examined the vertical structure of a particular CE sampled by the World Ocean Circulation Experiment (WOCE) P19 hydrographic section along 88°W, showing that the subsurface CE core have typical temperature and salinity anomalies of around ≈1°C and ≈0.1psu, respectively. More recently, Johnson and McTaggart (2010) used Argo float profile data to characterize AEs of the PCCS, showing that their core is located in the subthermocline and contains anomalous signature of the Equatorial Subsurface Water originating from the PCU.

5.2   Eddies in SEP: VOCALS Observations and Model Results

Data from the VOCALS-REx field program were used to characterize the hydrographic and velocity structure of the eddies. Anticyclonic eddies (sea level anomaly highs) are characterized by depressed isopycnals within the eddy (in the upper 300 m), deepened salinity minimum layer (SML), and low stratification beneath the mixed layer. Cyclonic eddies (sea level anomaly lows) were characterized by shoaling isopycnals in the upper 300 m, shoaling SML, and higher stratification beneath the mixed layer (Wood et al., 2011). An intensively surveyed cyclonic eddy was observed to have a subsurface velocity core diameter of 50 km, as well as a warm, salty, and highly stratified anomaly at its core at about 150 m depth. The net temperature anomaly of the eddy was negative, including an anomaly of approximately -1°C at 100 m depth due to the doming of isopycnals within the eddy. A relationship between eddy SLA and upper-ocean temperature was sought

in a variety of in-situ and remote sensing data, including VOCALS-REx profiles, Argo profiles, drifter observations, and satellite fields. In all of the data sources cyclonic eddies were significantly colder than anticyclonic eddies. The magnitude of the mean temperature signal was of opposite sign but equal magnitude for each type of eddy.

Figure 5.2 shows the Sea Level Anomaly (SLA) for days Nov 10th and Nov 20th during the cruise period for satellite observations and model results. The top two panels compare the satellite SLA with the model SLA showing similar large scale features in both. The model has finer scale structures due to a higher resolution than satellite observations. It can be seen that the intensively surveyed eddy at 76 W and 19.5 S has a low SLA signature evident in both observations and model. The currents from the model plotted as vectors also reveal a cyclonic eddy at this location and much finer scale structures around it. Figure 5.3 shows the SST on Nov 10th and 20th during the Ron Brown cruise period. During the month of November, SST in this region increases as the rate of upwelling decreases. Figures 5.2 and 5.3 reveal considerable mesoscale eddy variability qualitatively similar to that observed. SSH is a good surrogate for surface geostrophic currents and reveals eddy structures of length scale of 30 - 80 km. These can be considered the smallest well resolvable mesoscale features, and they are analyzed further in the following sections. Figure 5.4 shows the temperature at 250 m for 3 days , Nov 10th, Nov 14th and Nov 20th during the middle of the cruise period.

Many methods have been used in the past to detect eddies from satellite altimetry and infrared imagery. One such method is to use closed contours of vorticity. This has restrictions in geographical locations such as boundary layers where large ambient vorticity not associated with eddies is present (Isern-Fontanet et al., 2003). Another method is to search for geometric properties from sea surface height, such as extrema points and closed isolines, and then detect areas of zero geostrophic velocity; but for an eddy embedded in a background flow this is not invariant. The Okubo-Weiss (O-W) parameter (Okubo, 1970; Weiss, 1991) describes the relative dominance of strain and vorticity, and bypasses the two problems listed above. It is defined as:

$$W = S_n^2 + S_s^2 - \zeta^2, \tag{5.1}$$

where S_n, S_s, ζ are the normal and shear components of strain and the relative vorticity of the flow respectively. These components are defined as:

$$S_n = \frac{\partial u}{\partial x} - \frac{\partial v}{\partial y}, S_s = \frac{\partial v}{\partial x} + \frac{\partial u}{\partial y}, \zeta = \frac{\partial v}{\partial x} - \frac{\partial u}{\partial y} \tag{5.2}$$

The O-W parameter separates 2-D flows into different regimes (McWilliams, 1984): elliptic (OW < -OW$_0$), hyperbolic (OW > OW$_0$) and a background field ($|OW| \leq$ -OW$_0$), where OW$_0$ is a small threshold magnitude (Pasquero et al., 2001). A threshold for OW must be set so as to distinguish coherent structures from the background field. Previous studies with satellite altimetry data have used OW$_0$ = 0.2σ OW where σOW is the spatial standard deviation of OW. In an elliptic regime rotation dominates deformation (and vice versa for hyperbolic). Eddy cores can therefore be identified as connected regions with negative values of OW. This criteria for eddy identification has been used successfully with data from sea level altimetry maps (Isern-Fontanet et al., 2003; Morrow et al., 2004).

The last panel on Figure 5.4 shows the SLA with the contours of the Okubo-Weiss parameter plotted over it. The Okubo-Weiss parameter is a measure of vorticity vs shear in the fluid flow and hence closed contours of this parameter indicate closed circulating cells like eddies in the flow. This also highlights the eddy at 76 W which was measure intensively during the VOCALS-REx cruise. It also highlights the two CEs at 80 W and 84 W albeit not as strong as the one at 76 W. Closed contour structures with length scales greater than 10 - 20 km are indicative of eddy like structures. The 250 m temperature shows the doming of the isotherms beneath the cyclonic eddies. This is consistent with previous studies of eddy structure in this region (Chaigneau et al., 2011a; Holte et al., 2012).

Figure 5.5 shows eddy kinetic energy averaged for a week during the cruise period when the eddy was surveyed. The top panel overlays the SLA contours from satellite altimetry and the bottom panel shows the contours of model SLA overlaid on the same. It again reveals the intensity of the eddies (cyclonic and anticyclonic) showing that the CE at 78 W 18.5 S was the strongest and then the one at 84 W

19 S. The cyclonic eddy at 76W 19.5 S is of medium strength compared to the other eddies in this region. Figure 5.6 shows the snapshot of meridional velocity as a function of depth along 20 S revealing the doming isopycnals at 76 W and the strong positive and negative velocities on either side of the core of the eddy. The velocities are strongest at a depth of 200 m, showing a similar subsurface core cyclonic eddy as evident in previous studies of CEs in this region (Chaigneau and Pizarro, 2005; Chaigneau et al., 2011a). Figure 5.7 reveals the zonal velocities along 20S overlaid on salinity color shading. This shows the subsurface salinity minima layer within the eddy and the velocities being strongest at 200 m depth.

Observations of the PUC suggest that the undercurrent is narrow (10-40 km), flowing poleward over the continental slope, with peak speeds of 0.3-0.5 m s^{-1} in the depth range 100-300 m. Figure 5.8 shows the undercurrent meridional velocities in the model. The model undercurrent peaks at about 500m which is deeper than the observed peak range. A shallow salinity minimum layer (SML) characteristic of the Eastern South Pacific Intermediate Water (ESPIW), exists below the surface layer and shoals towards the shore. This feature has been long been observed and studied in profiles from the SEP (Tsuchiya and Talley, 1998). This low salinity water is formed in the eastern South Pacific from the subantarctic surface waters subducting below higher salinity waters to the north (Reid, 1973; Schneider et al., 2003; Karstensen, 2004).

5.3   Cyclonic and anticyclonic eddies along 19S

In this section we analyze the properties of the eddy at the surface and subsurface, identified from the ocean state estimate during the VOCALS-REx period. A detailed description of eddy properties is provided. Eddy properties such as velocities and hydrographic structure for both surface and subsurface levels are presented. Eddies form near the coast and propogate westward (Chaigneau and Pizarro, 2005; Johnson and McTaggart, 2010). Eddies have been linked to high sardine catches off of northern Chile due to increased nutrient supply to the surface layer (Hormazabal et al., 2004; Yáñez et al., 2001).

5.3.1 Horizontal and vertical structure

Eddies show a strong tendency for westward propagation, with cyclones exhibiting a poleward deflection and anticyclones exhibiting a equatorward deflection from their due west path, as noted in previous studies (Morrow et al., 2004; Chelton et al., 2007, 2011). This meridional deflection arises mainly from the beta effect and self-advection (Mcwilliams and Flierl, 1979). To study the westward propagation characteristics, only the cyclonic eddy and its propagation direction is considered.

We also analyzed the salinity (S) anomaly to study the water mass properties of eddies. The cyclonic eddy tracked at the subsurface shows a well defined S minima between 100-200 m, with two maxima of 0.031 psu at 150 m and 0.024 psu at 500 m. This positive anomaly, although weak, clearly shows that these eddies have their origin in the undercurrent or from the subantarctic subducting water with its salinity minima. In the composite of the actual S field, the eddy core is only visible as a general doming of isohalines (Figure 5.8c). This is likely due to the undercurrent water mixing with surrounding water during their journey. A similar tilting in isohalines in cyclonic eddies is observed in the California Current system (Reed and Halpern, 1976) and the undercurrent-generated eddies in this region do not always have a well defined S signature (Cornuelle et al., 2000). The cyclonic eddy intensively observed during the VOCALS-REx cruise has a salinity minima in its core at around 150 m which is anomalously fresher than any of its surrounding waters. The salinity in the core is similar to that in the cold fresher water flowing from the southern boundary and subducting below the salty warm water from the equator. The high gradients of S over the PCCS domain considered here make the S signatures less visible in Figure 5.8c. A recent study using Argo profiling floats in the eastern south Pacific also shows similar salinity structure for undercurrent generated anticyclones (Chaigneau et al., 2011b). The high-S core of the undercurrent off Chile is well distinguishable with low-S water above and below it.

5.4   Upper Ocean Heat Budget

In the PCCS, as in other eastern boundary regions, the mean flow is weaker than its mesoscale eddy velocities, and the eddy fluxes are cited to be important contributors to momentum and tracer balances (Marchesiello et al., 2003; Capet et al., 2008). As yet few modeling studies have covered the entire PCCS with a horizontal resolution high enough to resolve the mesoscale. In this section, a regional heat balance in a high-resolution ocean state estimate is studied of the PCCS circulation for a period of a month. The methodology and results are extensions of previous PCCS simulations by (Penven, 2005; Colas et al., 2011). Xie et al. (2007) and Toniazzo et al. (2009) are recent coupled-model simulation studies of the PCCS with marginal eddy resolution (i.e., 0.5 in a large-regional domain and 0.33 in a global domain, respectively). Zheng et al. (2010) is an oceanic simulation study with high resolution (i.e., $< 1/12^o$ in a nearly global domain).

Measurements and analyses show a mean net warming heat flux from the atmosphere to the ocean of 40-80 W m^{-2} over a wide cross-shore swath in the Southeast Pacific, and this warming has to be compensated by cooling through oceanic lateral transport. At an offshore buoy site (20^oS, 85^oW), Colbo and Weller (2007) estimate that the oceanic eddy flux divergence has an important contribution to the heat balance, comparable to the cooling by large-scale advection that includes Ekman transport, which by itself is insufficient for equilibrium balance. The time-mean oceanic heat balance integrated over the upper ocean is

$$\int_{z_0}^{\eta} \rho_0 C_p \partial_t \overline{T} dz = -\int_{z_0}^{\eta} \rho_0 C_p \nabla \cdot \overline{\mathbf{u}T} dz + Q_{net} - \rho_0 C_p \overline{\kappa_\nu \partial_z T}|_{z_0} - \int_{z_0}^{\eta} \rho_0 C_p \kappa_h \nabla^2 T,$$

$$(5.3)$$

where Q_{net} is the net surface heat flux, C_p is the specific heat of seawater at constant pressure, ρ_0 is the density of seawater, $\mathbf{u}$ is the total velocity vector, T is temperature and κ_ν and κ_h are the subgrid-scale horizontal and vertical eddy diffusivity parameters. The first term on the left hand side is the rate of temperature change (or temperature tendency), the first term on the right-hand side is the tem-

perature advection followed by the terms for net surface heat flux and horizontal and vertical diffusion, respectively. In this study, we mainly focus on the discussion of horizontal advection and diffusion terms balancing the temperature tendency of the upper ocean. Colbo and Weller (2007) suggest that the divergence of the eddy heat flux, horizontal advection and the horizontal and vertical diffusion terms are significant and are the dominant terms that are in mean balance.

Although a heat balance in long term steady state is not achieved due to the relative short periods of the data assimilation fits, the ocean state estimate can still be analyzed to understand the key mechanisms which are in balance during the period of the cruise. The solution is integrated until 400 m depth and hence, the vertical advection from below this layer is assumed to be small, due to very small vertical velocities at this level. Hence, the advection term in the heat balance equation vertically integrated is dominantly the horizontal advection term.

5.4.1   Spatial distribution of the upper-ocean heat budget

In this section, the spatial distribution of major contributing terms, discussed in the previous section, is examined for region around the VOCAL-REx cruise track. We explore how advection and diffusion terms contribute to the upper-ocean heat budget by analyzing the model output around the 20° S region. We also analyze the structure of the heat advection terms with respect to the location of the eddies in the model and qualitatively assess the importance of eddies for the horizontal advection. Previous modeling studies have shown that the eddy heat flux divergence is not spatially coherent, so eddies likely do not impact the heat budget in the southeast Pacific contrary to the findings of Colbo and Weller (2007) (Zheng et al., 2010).

The spatial pattern of each term of equation 5.3 in the model heat balance for the period during the which the eddy was observed intensively is shown in Figure 5.9. The advection term is the dominant term with an order of magnitude similar to that of the temperature tendency. The pattern of the mean sea level anomaly during the period is plotted as contours over the advection color contours in Figure 5.9b. Around the cyclonic eddies, to the south of the eddy, it advects

cold water from the south to the warmer waters to the north and hence has a net cold advection. Similarly to the northern boundary of the eddy, it advects warmer water from the north towards the colder waters in the south and hence advects warm water southward. As the eddy evolves and mixes with the surrounding water, it would eventually warm up the cold core it is carrying within from the undercurrent or subantarctic water. Yet this is estimated to happen at a much longer timescales (of the order of 90 - 150 days) than can be observed with short term assimilation fits. In this model heat balance, the eddy does not have a net effect on the heat advection when averaged over space and time. The vertical diffusion term seen in Figure 5.9c, is three times smaller than the temperature advection term or the temperature tendency term. The vertical diffusion term has a net cooling effect over the entire domain. The horizontal diffusion term has a smaller magnitude and has much smaller spatial scale structures than the vertical diffusion as seen in Figure 5.9d and mainly is seen to play a role in smoothing strong gradients of temperature across fronts from eddy boundaries or nonlinear fronts. Unlike the theory expounded by Gill and Niller (1973) of large-scale heat balance in the ocean being such that the heat input is mainly stored locally and horizontal advection by the mean flow not playing an important role, it appears that the horizontal advection is the dominant term in the coastal PCCS region and the vertical diffusion, which would store the heat input from the surface in the deeper ocean layers, plays a smaller role albeit not insignificant in cooling the surface.

5.5   Summary and Discussion

This study examines the upper-ocean processes in the stratus cloud deck region explored during the VOCALS-REx cruise of 2008 using the eddy-resolving ROMS ocean state estimate after data assimilation of cruise track CTD casts. The structure and properties of eddies in the upper-ocean during this period is examined using the eddy-resolving ROMS and observational data. A comparison of eddy activity in ROMS with that derived from satellite observations (i.e.,

AVISO) indicates that ROMS is capable of simulating the realistic eddies in the stratus cloud region. A substantial amount of data in the upper ocean and atmospheric boundary layer had been collected in the southeast Pacific during the VAMOS Ocean-Cloud-Atmosphere-Land Study (VOCALS) Regional Experiment (Wood et al., 2011).

Eddy properties in the PCCS are studied with a high-resolution (dx = 7 km) regional model ocean state estimate and an altimetry analysis, using eddy tracking methods. Eddy identification is made using a closed contour method on the SSH anomaly field (SSH method).

The major properties of the PCCS eddies from the model eddy analysis are the following:

The analysis of model eddies show that eddy signals penetrate to 800-1500 m in depth. Cyclonic eddies featured a shoaling salinity minimum layer (SML), doming isopycnals near the surface. Anticyclonic eddies were characterized by a depressed SML and depressed isopycnals in the upper ocean. An intensively surveyed cyclonic eddy was characterized by high salinity as predicted by Johnson and McTaggart (2010). The eddy had an average temperature anomaly of approximately -0.4^{o}C over a depth range from 100 - 700 m and features a cold anomaly of approximately -1°C near 150 m depth. The net temperature anomaly of the eddy depends on the depth to which it is integrated, though it is negative overall. The cold near-surface anomaly, caused by the doming of near-surface isopycnals, is likely more relevant than the net anomaly for assessing the effect of eddies on upper-ocean temperature, as it is more likely to be incorporated into the mixed layer. The vertically-integrated heat content of anticyclonic eddies determined from the ocean state estimate is only slightly different from that of cyclonic eddies.

The ability to identify and track eddies in space and time opens up many new possibilities in the study of mesoscale eddies, in the context of PCCS and other similar eddy active regions, too. In the present study we address only the general properties (e.g., radius, shape, propagation characteristics, nonlinearity, and vertical structure) of the PCCS eddies. Many aspects of the PCCS eddies

have yet to be explored. For example, with space-time information about eddies, estimates of offshore heat and mass transport by mesoscale eddies can be made more precisely. A study in this direction by Treguier et al. (2003), shows that transport estimates by Agulhas rings using a conventional method (perturbation to the time-mean flow) and by an eddy method (based on the water trapped inside the eddy) show significant differences, with the latter always being higher. The role of mesoscale eddies in various biological processes in the PCCS, like injection of nutrients into the euphotic zone and offshore transport of biogenic material, can be better addressed with physics-biology coupled models and eddy tracking tools. The PCCS region is known to exhibit strong interannual variability (e.g., El Niño - Southern Oscillation) and hence is expected to have a signature in eddy activity, too.

A relationship between eddy SLA and upper-ocean temperature was computed. Cyclonic eddies (SLA < -5 cm) were characterized by cooler upper-ocean temperatures relative to mean conditions and anticyclonic eddies (SLA > 5 cm) were characterized by warmer upper-ocean temperatures in all of the data sources. T-tests performed on the eddy temperature distributions confirmed that the mean temperature anomalies of cyclonic and anticyclonic eddies were significantly different. The cooler surface temperatures associated with cyclonic eddies could be due to the uplift of isopycnals near the eddy cores. The SML coincides with a large vertical temperature gradient. In cyclonic eddies, this temperature gradient is raised toward the surface, allowing for easier entrainment of deeper, colder waters into the mixed layer. Any ocean feature that uplifts the SML and its associated temperature gradient could result in colder surface temperatures. In anticyclonic eddies, the SML is depressed, isolating the mixed layer from the colder water at depth. The observed uplift of near-surface isopycnals in cyclonic eddies is not necessarily due to eddy transport at that depth; rather, it could be due to deformation of the near-surface isopycnals caused by eddy transport in deeper levels. Cyclonic and anticyclonic eddies are observed to occur with similar frequency and have opposite effects on the surface layer temperature; because of this symmetry, we conclude that eddy temperature transport likely has minimal net effect on the upper-ocean

temperature in the SEP.

The heat balance for the period of the cruise from the ocean state estimate reveals that the mean horizontal advection is the dominant term that balances the temperature tendency of the upper layer of the ocean. The vertical diffusion is secondary and is about 30% of the advection magnitude. One of the major sources of cooling that balances the positive surface heat fluxes is advection dominated by geostrophic transport. These results are partially consistent with those from observations described in Colbo and Weller (2007). Major terms of the heat equation in the upper 400 m were also calculated over the region of the cruise. The heat transport produced by geostrophic transport is one of the primary sources of cooling in the entire stratus region because of its spatial coherence (Zheng et al., 2010).

5.6   Acknowledgements

Figure 5.1: Locations of the 438 UCTD profiles collected during VOCALS-REx (black dots). The underway ADCP velocities (black arrows) are averaged over 50 - 650 m depth. The background colored contours represent the mean SLA during the cruise; the ± 5 cm SLA contours are highlighted by black contours. The locations of three cyclonic eddies (C1,C2, and C3) and two anticyclonic eddies (A1 and A2) are labeled. The bathymetry is plotted at 1000-m intervals (black contours). (Holte et al., 2012)
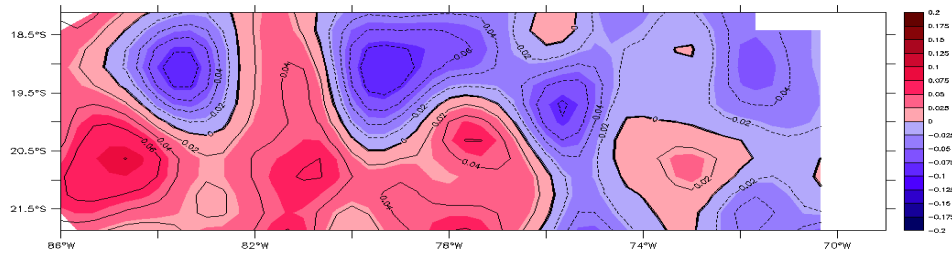
(a) Obs: Nov 10th
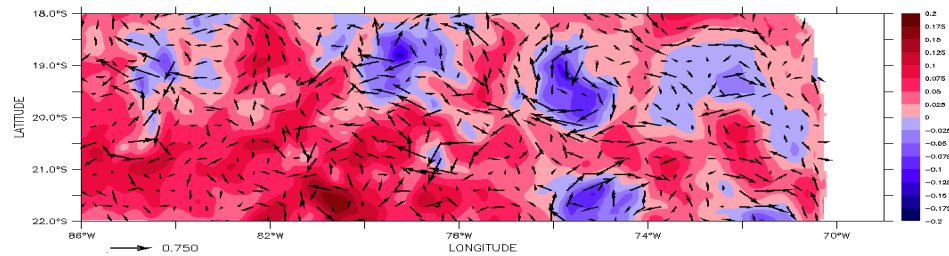
(b) ROMS: Nov 10th
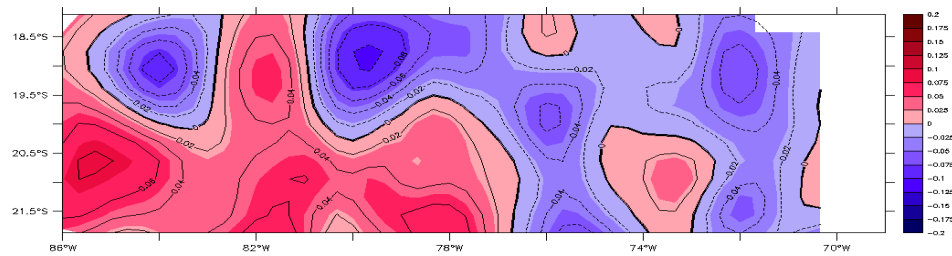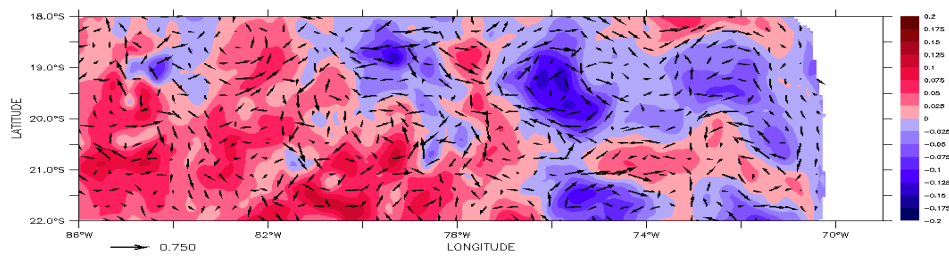
(c) Obs: Nov 20th

(d) ROMS: Nov 20th

Figure 5.2: Sea level anomaly from AVISO mapped fields in the panels (a) and (c) and from the ROMS ocean state estimate in panels (b) and (d). The velocities from the model are overlaid the sea level anomaly contours to reveal cyclonic and anticyclonic eddies.
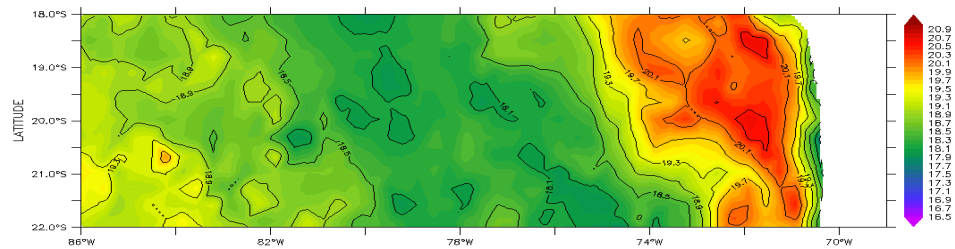
(a) Obs: Nov 10th
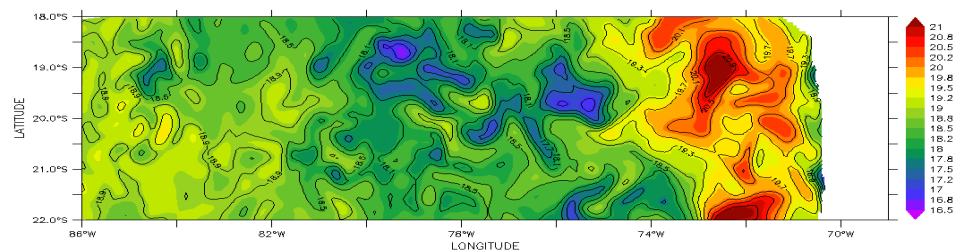
(b) ROMS: Nov 10th
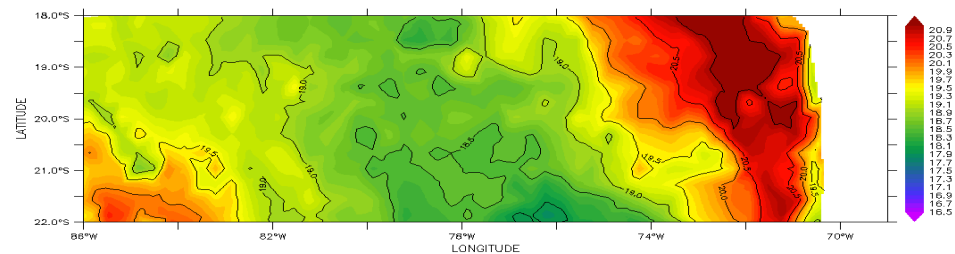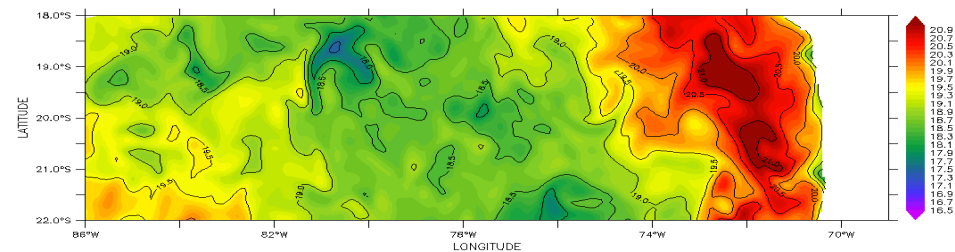
(c) Obs: Nov 20th

(d) ROMS: Nov 20th

Figure 5.3: SST from NOAA Optimally Interpolated observations in panel (a) and (c) and SST from ROMS with the model velocities overlaid for the days 10th Nov and 20th Nov
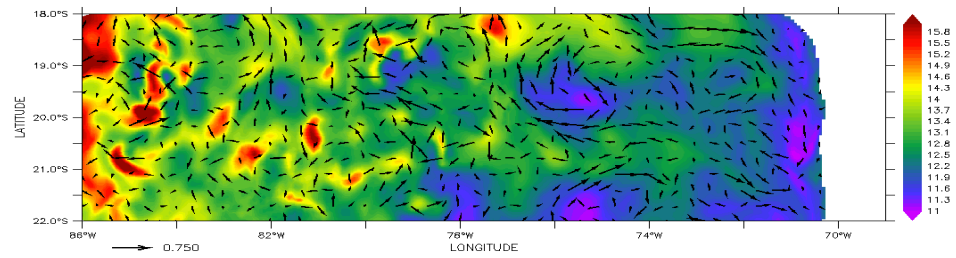
(a) ROMS:10th Nov
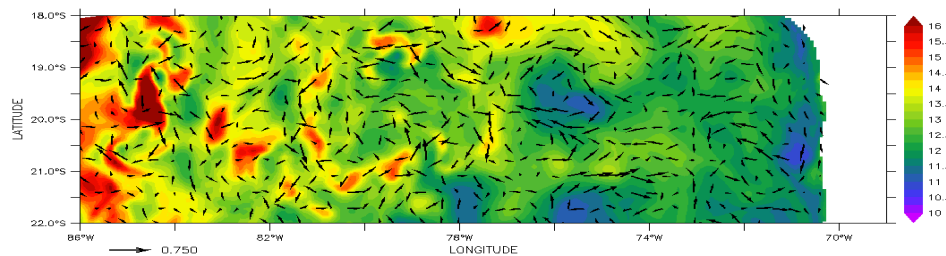
(b) ROMS:14th Nov
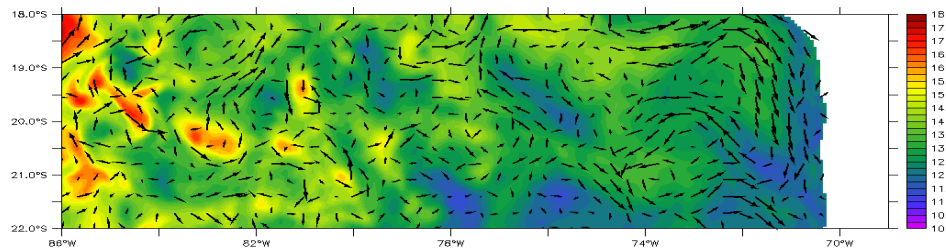
(c) ROMS:20th Nov
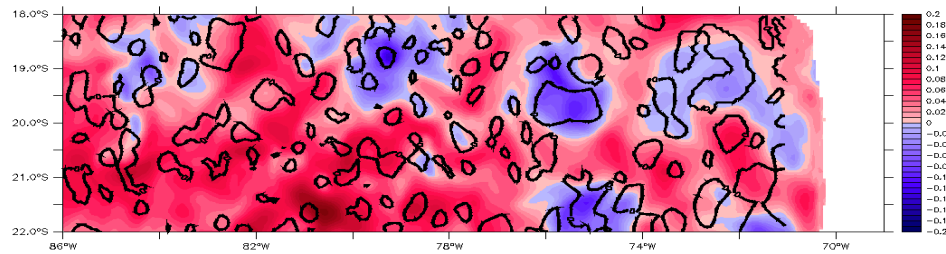
(d) ROMS SSH:10th Nov

Figure 5.4: Temperature at 250 m Depth in the ocean state estimate for three different days (a) 10th Nov, (b) 14th Nov and (c) 20th Nov showing the evolution of the eddy in time in the model. The last panel (d) is the color contours of SLA with the Okubo-Weiss parameter overlaid on top to show eddy like structures.
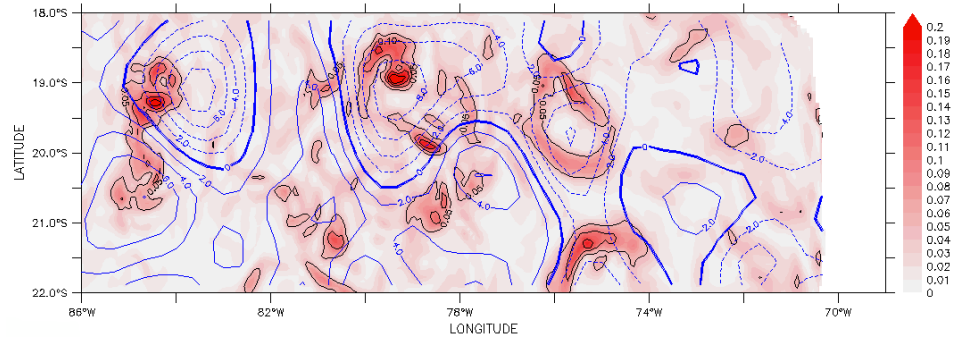
(a) EKE with Obs. SLA Contours for Nov 1 - 15th
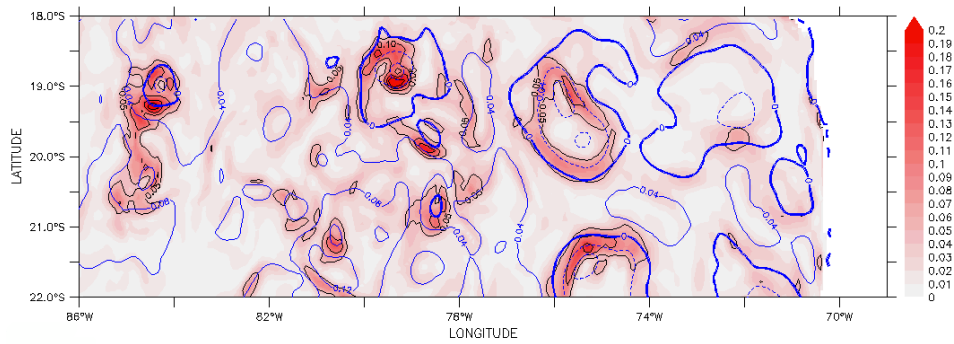
(b) EKE with ROMS SLA Contours for Nov 1 - 15th

Figure 5.5: Eddy Kinetic Energy averaged for the first two weeks of November from the model overlaid with the (a) AVISO SLA and (b) ROMS SLA.
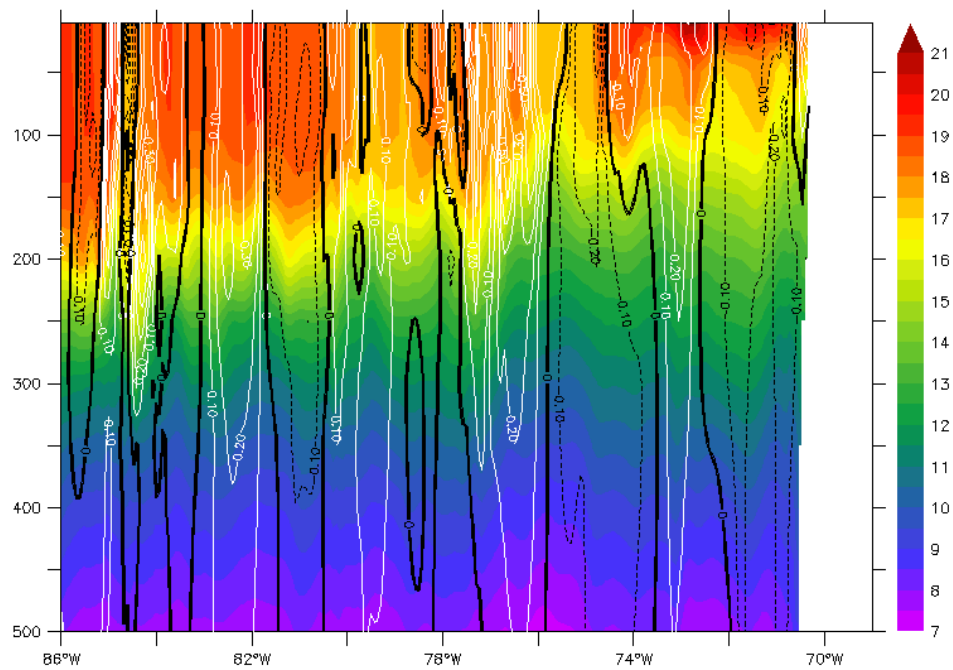
Figure 5.6: Vertical temperature profiles (color) and meridional velocity (line contours) for Nov 10th revealing the eddy structure in depth. The profile is plotted at 20° S from 86 ^{o} W to 69°W

Figure 5.7: Zonal velocities of eddy at 20 S on the same day Nov 10th with the color contours showing salinity. The cross-section is from 20S to 19 S.
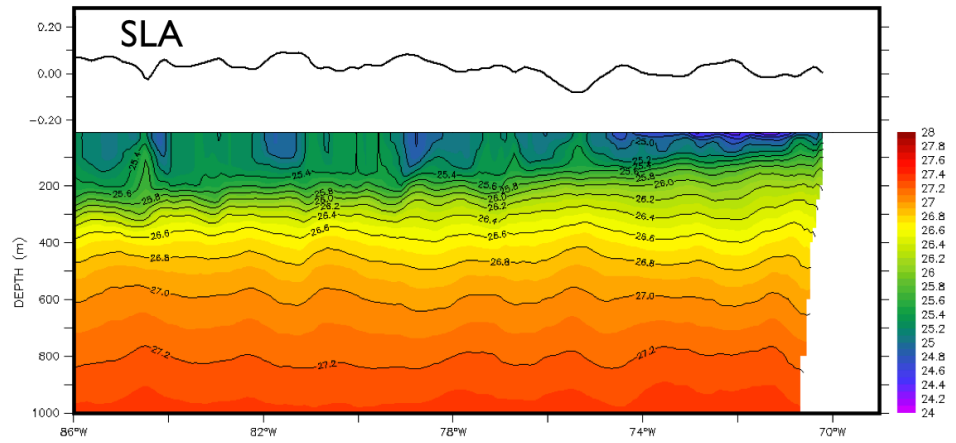
(a) SLA and Density profiles
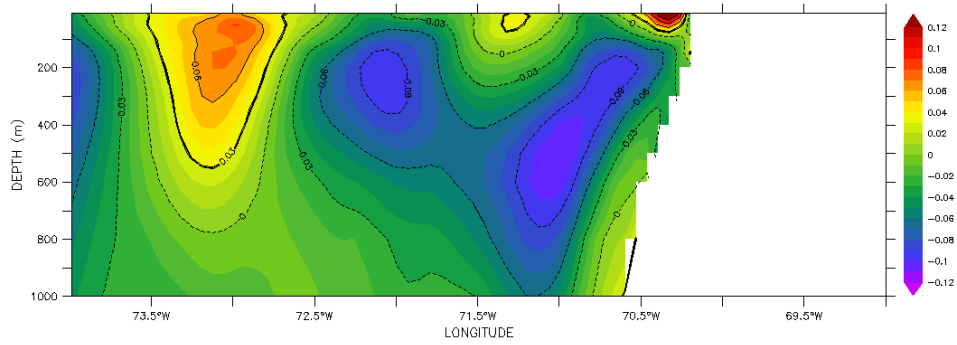
(b) Meridional velocity from 74W to 69W
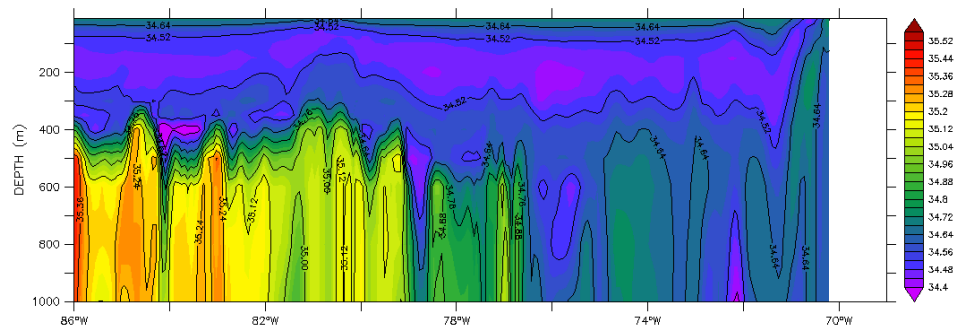
(c) Salinity from 86 W to 69 W

Figure 5.8: Vertical Profiles at 20 deg S of (a) Sea level anomaly and density profiles (b) Meridional velocity averaged over 7 days and (c) Salinity depicting the subsurface salinity minima layer
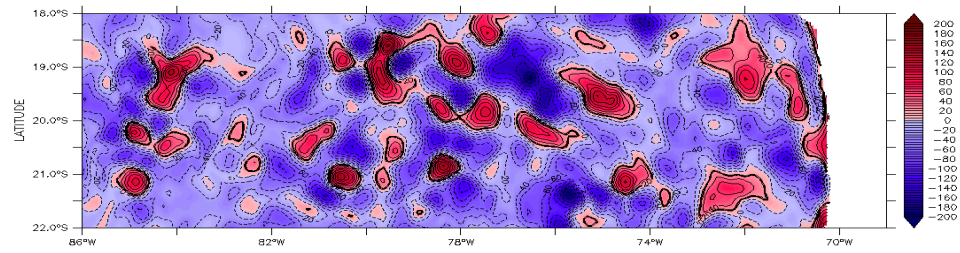
(a) Temp. Tendency
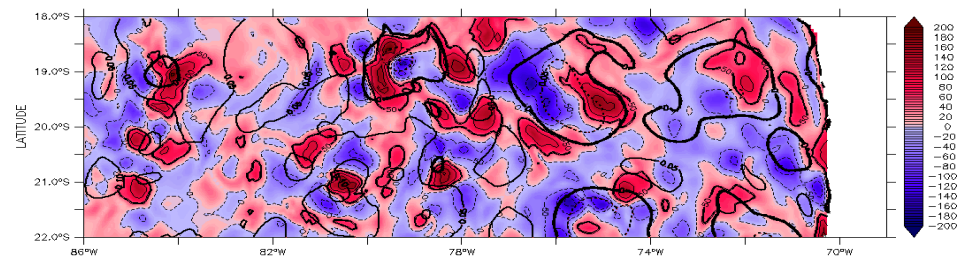
(b) Advection with SLA contours overlaid
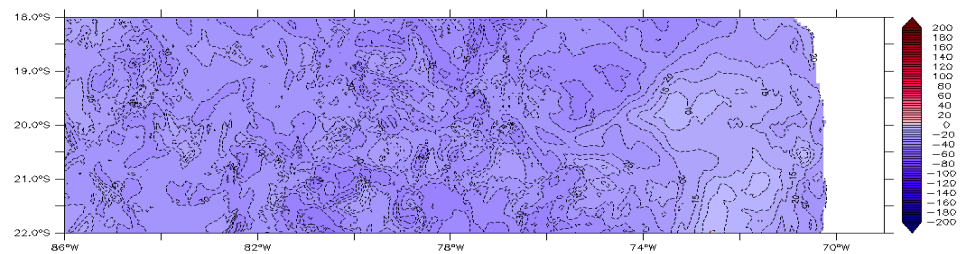
(c) Vertical Diffusion
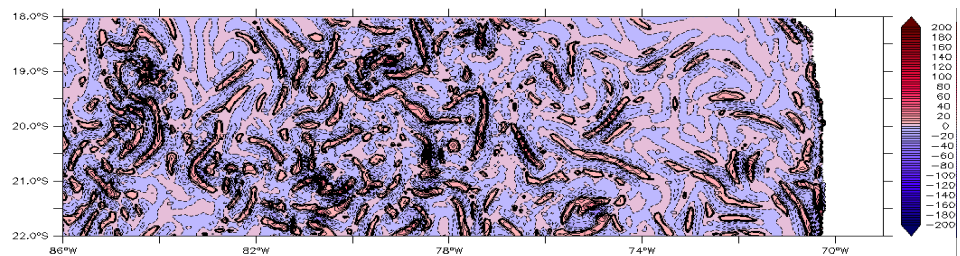
(d) Horizontal Diffusion

Figure 5.9: Spatial maps of heat budget terms from the model for 86 W:69W and 22S:18S. The heat budget terms are integrated to the depth of about 400 m and for a period of two weeks when the eddy was strongest.

Chapter 6

Linear vs Nonlinear Filtering with scale selective corrections for balanced dynamics in a simple atmospheric model

We investigate the role of the linear analysis step of the ensemble Kalman filters (EnKF) in disrupting the balanced dynamics in a simple atmospheric model and compare it to a fully nonlinear particle-based filter (PF). The filters have a very similar forecast step, but the analysis step of the PF solves the full Bayesian filtering problem, while the EnKF analysis only applies to Gaussian distributions. We compare the EnKF to two flavors of the particle filter with different sampling strategies, the Sequential Importance Resampling Filter (SIRF) and the Sequential Kernel Resampling Filter (SKRF). The model admits a chaotic vortical mode coupled to a comparatively fast gravity wave mode. It can also either be configured to evolve on a so-called slow manifold, where the fast motion is suppressed or such that the fast-varying variables are diagnosed from the slow-varying variables as slaved modes. Identical twin experiments show that EnKF and PF capture the variables on the slow manifold well as the dynamics is very stable. PFs, especially the SKRF, capture slaved modes better than the EnKF implying a

full Bayesian analysis estimates the nonlinear model variables better. The PFs perform significantly better in the fully coupled nonlinear model where fast and slow variables modulate each other. This suggests that the analysis step in the PFs maintain the balance in both variables much better than the EnKF. It is also shown that increasing the ensemble size generally improves the performance of the PFs but has less impact on the EnKF after a sufficient number of members has been used.

6.1   Introduction

The quality of the forecasts of the state of the atmosphere and ocean depends on the accuracy of the solutions of the partial differential equations (PDEs) describing these systems. Various data assimilation techniques have been developed over the last three decades to improve upon these solutions of the PDEs and to constrain the solutions to the ever increasing number of observations. This helps in reducing the uncertainties in the forecast of these highly chaotic systems. The most popular data assimilation schemes in operational forecasts are the four-dimensional variational assimilation (4D-VAR) approach (Lewis and Derber, 1985; Le Dimet and Talagrand, 1986) and the ensemble Kalman Filter approach (Evensen, 1994; Tippett et al., 2003).

The oceanic and atmospheric systems have multiple scales of dynamics interacting nonlinearly in time and space. For instance, the atmospheric system varies on timescales from climate to weather. The weather is fast-varying, nonlinear and chaotic and is known as an initial value problem, while the climate is slowly varying and is known as a boundary value problem (Lorenz, 1991). Ocean physics also involve multiple processes on multiple scales, from a few millimetres to thousands of kilometers in space and from seconds to decades in time. These are characterized by small-scale turbulent processes, mesoscale variability, decadal and climate changes, all interacting with each other (Robinson and Lermusiaux, 2004).

4DVAR and EnKF-based assimilation schemes have addressed the problem of forecasting multi-scale systems to some extent. They have many associated problems with regard to the nonlinearity of the models and assimilating observations with dynamics at various timescales and measures of nonlinearity (Bennett, 2002; Hoteit and Köhl, 2006; Van Leeuwen, 2010). In meteorological and climatological applications, "balance" generally refers to the dominance of vortical motion over inertia-gravity waves. In multi-scale systems like the ocean or atmosphere in which modeled flows in certain regimes are expected to be balanced, it has been found that current 4D data assimilation techniques, as the EnKF and 4DVAR, could cause the excitation of spurious unbalanced motion (Polavarapu et al., 2000; Houtekamer and Mitchell, 2005; Neef et al., 2006). This has been known to happen due to the development of unphysical correlations. Solutions to this problem have been attempted by imposing balance constraints on the analysis (Courtier and Talagrand, 1990; Dee, 1991b; Todling and Cohn, 1994; Polavarapu et al., 2000; Kepert, 2004) or by filtering out fast modes. Imbalance in the flow due to the assimilated data cannot be completely corrected for even with such adjustments (Neef et al., 2009). Gershgorin and Majda (2010) show that a linear Kalman filter with model error performs better than an exact Nonlinear Extended Kalman Filter (NEKF) for large enough observation times in a nonlinear slow-fast system, yet they also show that the NEKF is stable for the case of strong fast forcing and hence for strong non-Gaussianity unlike the linear KF. The application of the EnKF is still largely in a discussion/testing phase (Lorenc, 2003; Houtekamer and Mitchell, 2005). The ability of this method to capture unbalanced motion is, however, still poorly understood (Neef et al., 2009). Szunyogh et al. (2005) is an example of a case in which an EnKF-type assimilation method was able to capture a fast varying gravity wave mode that was present in observations and not in the model forecast indicating that flow-dependent covariance models can potentially capture unbalanced motion. Neef et al. (2006) reported similar results where the EnKF was able to provide better estimates of the fast varying modes than the linearized (extended) kalman filter. Other techniques such as scale dependent modeling and assimilation using the ensemble Kalman Filter have been attempted too (Zou and

Ghanem, 2005) in engineering applications. This would be a more appropriate solution if the coupling between the scales were not highly nonlinear and chaotic as in the ocean or atmosphere dynamics.

4DVAR and the EnKF are equivalent when the system is Gaussian and linear (Kalnay et al., 2007), but both do not fully address the nonlinear estimation problem (Van Leeuwen, 2010). The 4DVAR solution requires solving a non-convex optimization problem while the EnKF analysis is still based on the linear correction step of the Kalman filter (Le Dimet and Talagrand, 1986; Anderson, 2001; Hoteit et al., 2008). For nonlinear data assimilation problems, the optimal solution is believed to be the solution of the Bayesian estimation problem which involves the estimation of the conditional probability distribution function (PDF) of the system state given all available measurements up to the estimation time (Doucet et al., 2000). Knowledge of the state PDF allows determining different estimates of the state, such as the minimum variance (MV) estimate (Todling, 1999). The particle filter (PF) uses point-mass representation of the state PDF to provide a discrete approximation of the optimal nonlinear filter (ONF) (Doucet et al., 2000). In the PF, the particles are integrated forward with the numerical model to propagate the state PDF in time, and their assigned weights are updated every time new observations are available. The PF, however, suffers from the degeneracy phenomenon of its particles when most weights become concentrated on very few particles. Tackling this problem would require using resampling and a very large number of particles (Doucet et al., 2000). To alleviate this problem, Evensen (1994) proposed the EnKF while replacing the weight correction step by the linear Kalman correction step for each particle. This was shown to significantly enhance the robustness of the filter and allowed the implementation of the Bayesian filtering theory with small size ensembles of particles (Kivman, 2003; Hoteit et al., 2008; Van Leeuwen, 2010).

Despite recent successful implementations of the EnKF with various atmospheric and oceanic assimilation problems (Houtekamer and Mitchell, 2005; Hoteit et al., 2005; Pu and Hacker, 2009), it is still not clear to what extent the linear correction step affects the accuracy of the filtering solution. Kivman (2003) com-

pared the performances of the EnKF and the PF for the parameter estimation problem and found that the linear correction step of the EnKF fails to provide accurate estimates of the system parameters because of the strong nonlinear relation between the parameters and the observations. More recently, Jardak et al. (2010) compared the performances of the same filters in the presence of linear and nonlinear observation operators and concluded that the nonlinear filters are superior in the latter case. In this work, we are interested in assessing the impact of the linear correction step on the estimation of the different scales of the studied system. Following Neef et al. (2006), we address this problem using the simplified dynamical model of Lorenz (1986) which admits one nonlinear vortical mode and one inertia-gravity wave. We study the performance of the linear-based EnKF and two kinds of nonlinear filters, the Sequential Importance Resampling Filter (SIRF) and the Sequential Kernel Resampling Filter (SKRF). A similar problem has been considered by Neef et al. (2006) but studying the impact of linearization in the extended Kalman filter versus the ensemble approach, and by Neef et al. (2009) studying the impact of flow-dependent covariance evolution in the ensemble KF vs a static covariance model in an OI. In the Lorenz-86 model, we are mainly investigating whether the EnKF fails to capture the nonlinear coupling between the slow variable and the fast variable due to its linear correction step. This coupling between the slow and fast variable is preserved in the forward integration of the PFs and hence, we show that they perform better in preserving the balance in the model as compared to the EnKF. When the dynamics lie on the slow manifold, we show that the EnKF performs as well as the PFs since the dynamics are approximately linear. We are particularly interested to see if the nonlinear correction step captures the fast growing modes better compared to the EnKF, and if so whether it still maintains the improvement in the analysis of the slow evolving mode. The second focus is to study the behavior of two different nonlinear filters compared to the EnKF for data assimilation in this model with varying observation frequencies and varying scales.

In the first set of experiments of this study we will evaluate the performance of the three different filters in the slow manifold framework of the Lorenz-86 model.

The model is configured in the Slow Manifold with the fast modes set to zero and only the slowly varying vortical mode evolving in time. We test and show that the EnKF performs well compared to the two types of particle filters. In the second set of experiments we address the balanced flow problem, or flow where the vortical motion dominates and the inertial/gravitational motion is 'slaved' to the dominant vortical mode flow. In the third set of experiments we will evaluate the accuracy of the three different filter analyses with a fully nonlinear model with the slowly varying vortical mode coupled to the fast inertia-gravity wave mode and each of them evolving in time independently.

The chapter is organized as follows. The algorithms of the ensemble Kalman filter and the two types of particle filters are described and their characteristics compared in Section 6.2. Section 3 describes the different configurations of the extended Lorenz-86 model used in these experiments. The experimental setup describing the different model configurations and observation schemes used for experiments are presented in Section 4. Section 5 contains discussion and conclusions.

6.2   Linear and Nonlinear Bayesian Filtering

The Bayesian filtering approach is presented first and then approximations for its Monte Carlo implementation are presented in the forms of the PF and the EnKF.

To describe the Bayesian Filtering algorithm, consider the following nonlinear stochastic discrete-time dynamical system

$$\boldsymbol{x}_k \;\; = \;\; \boldsymbol{M}_k(\boldsymbol{x}_{k-1}) + \boldsymbol{\eta}_k, \tag{6.1}$$

$$\boldsymbol{y}_k \;\; = \;\; \boldsymbol{H}_k(\boldsymbol{x}_k) + \boldsymbol{\epsilon}_k, \tag{6.2}$$

where $\boldsymbol{x}_k$ is the state vector (to be estimated), of dimension n, $\boldsymbol{y}_k$ is the observation vector, of dimension p, $\boldsymbol{M}_k$ and $\boldsymbol{H}_k$ are two continuously differentiable maps from $\mathbb{R}^n$ to $\mathbb{R}^n$ and from $\mathbb{R}^n$ to $\mathbb{R}^p$ respectively representing the transition and the observational operators, and $\boldsymbol{\eta}_k$ and $\boldsymbol{\epsilon}_k$ denote the dynamical and the observational

noise, respectively. The conditional distributions of $\boldsymbol{\eta}_k$ and $\boldsymbol{\epsilon}_k$, given $\boldsymbol{x}_0, \ldots, \boldsymbol{x}_k$ are assumed to be Gaussian with zero mean and non-singular covariance matrices $\mathbf{Q}_k$ and $\mathbf{R}_k$, respectively.

Starting from a random initial condition with a known probability density function, the Bayesian filter provides the conditional density function of the system state given all available measurements up to the estimation time. To simplify the notation, we define $\boldsymbol{y}_{1:k}$ as a shorthand for the set of observations $\boldsymbol{y}_1, \ldots, \boldsymbol{y}_k$ previous to time t_k. Let $p_k^f(\,\cdot\mid\boldsymbol{y}_{1:k-1})$ be the conditional (predictive) density of $\boldsymbol{x}_k$ given $\boldsymbol{y}_{1:k-1}$ and $p_k^a(\,\cdot\mid\boldsymbol{y}_{1:k})$ be the conditional (analysis) density of $\boldsymbol{x}_k$ given $\boldsymbol{y}_{1:k}$, both determined at time t_k. The Bayesian filter recursively operates with a succession of prediction and correction steps as summarized below. The reader is referred to Doucet et al. (2000) for an extensive description of the filter.

- _Prediction step_: The predictive density $p_k^f(\,\cdot\mid\boldsymbol{y}_{1:k-1})$ is obtained by integrating $p_{k-1}^a(\,\cdot\mid\boldsymbol{y}_{1:k-1})$ with the model (6.1) to the time of the next available observation t_k. The conditional density of the state vector $\boldsymbol{x}_k$ to be at $\boldsymbol{x}$ at time t_k given that it was at u at time t_{k-1} is $\phi\left(\boldsymbol{x} - \boldsymbol{M}_k(\boldsymbol{u}); \mathbf{Q}_k\right)$, where

$$\phi(\boldsymbol{x}; \boldsymbol{\Sigma}) \;\; = \;\; \frac{1}{\sqrt{\det(2\pi\boldsymbol{\Sigma})}} \exp\left(-\frac{\boldsymbol{x}^T \boldsymbol{\Sigma}^{-1} \boldsymbol{x}}{2}\right) \tag{6.3}$$

denotes the Gaussian density of zero mean and covariance matrix $\boldsymbol{\Sigma}$. Thus,

$$p_k^f(\boldsymbol{x}\mid\boldsymbol{y}_{1:k-1}) \;\; = \;\; \int_{\mathbb{R}^n} \phi\left(\boldsymbol{x} - \boldsymbol{M}_k(\boldsymbol{u}); \mathbf{Q}_k\right) p_{k-1}^a(\boldsymbol{u}\mid\boldsymbol{y}_{1:k-1}) d\boldsymbol{u}. \tag{6.4}$$

- _Correction step_: After a new observation $\boldsymbol{y}_k$ is made, the analysis density $p_k(\,\cdot\mid\boldsymbol{y}_{1:k})$ at time t_k is determined by "correcting" the predictive density with the new observation using the Bayes rule,

$$p_k^a(\boldsymbol{x}\mid\boldsymbol{y}_{1:k}) \;\; = \;\; \frac{1}{b_k} p_k^f(\boldsymbol{x}\mid\boldsymbol{y}_{1:k-1})\phi\left(\boldsymbol{y}_k - \boldsymbol{H}_k(\boldsymbol{x}); \mathbf{R}_k\right). \tag{6.5}$$

The analysis density is therefore obtained by multiplying the prior predictive density by the observation density and normalizing by $b_k = \int_{\mathbb{R}^n} p_k^f(\boldsymbol{u}\mid\boldsymbol{y}_{1:k-1})\phi\left(\boldsymbol{y}_k - \boldsymbol{H}_k(\boldsymbol{u}); R_k\right) d\boldsymbol{u}$ to ensure a probability density.

While the expressions of the state *PDF* can be easily obtained, determining the value of the predictive density at each point of the state space is practically impossible for large dimensional systems (Doucet et al., 2000). This actually requires the evaluation of the model $\boldsymbol{M}_k(\boldsymbol{x})$ for a prohibitive number of values of $\boldsymbol{x}$, knowing that even one single evaluation can be computationally prohibitive in realistic atmospheric and oceanic applications (Snyder et al., 2008). The particle filter and the ensemble Kalman filter are two discrete approximations of the Bayesian filter. Here we describe the characteristics of these two Monte Carlo implementations of the Bayesian filter.

6.2.1   The Particle Filter (PF)

The PF provides a discrete solution of the Bayesian filtering problem using point-mass representations $\sum_{i=1}^{N} w_i \delta_{\boldsymbol{x}^i}$, of the state *PDFs* (Doucet et al., 2000). The vectors $\boldsymbol{x}^i$ are called particles and the w_i are their associated weights. N is the number of particles (or the size of the ensemble). After a forecast or analysis step, the minimum variance estimate of the system state is then obtained as the weighted-average of the ensemble $\sum_{i=1}^{N} w^i \boldsymbol{x}^i$. Starting from an initial ensemble of particles $\boldsymbol{x}_0^i, i = 1, \ldots, N$, the PF algorithm consists of a prediction step to integrate the particles in time and a correction step to update the weights as follows:

- *Prediction step*: At time t_{k-1}, the particles $\boldsymbol{x}_{k-1}^i$ are integrated forward with the model to the time of the next available observation t_k.

- *Correction step*:: The new observation is used to update the weights with

$$w_k^i \;=\; \frac{1}{c_k} w_{k-1}^i \phi \left(\boldsymbol{y}_k - \boldsymbol{H}_k(\boldsymbol{x}_k^i); \mathbf{R}_k \right), \tag{6.6}$$

where c_k is a constant normalizing the total weight. The particles remain unchanged. Thus a particle receives more/less weight proportional to its distance from the most recent observation normalized by the observational error covariance matrix $\mathbf{R}_k$.

In practice, the PF suffers from a major problem known as the degeneracy phenomenon (Doucet et al., 2000); after several iterations most weights become concentrated on very few particles. This happens because the particles drift away from the true state with the observations exerting no feedback on the particles. The "effective" size of the ensemble decreases over time and after few assimilation steps only a small fraction of the ensemble contributes to the filter solution, causing very often the divergence of the filter. Resampling was introduced as a way to get around this problem. This Monte-Carlo technique basically consists of drawing new particles according to the *PDF* of the ensemble and then reassigning them the same weights (Doucet et al., 2000). In most applications, the new particles are drawn from the discrete approximation of the state *PDF*. This is known as the Sequential Importance Resampling Filter (SIRF). To avoid drawing similar particles when the system noise is absent or insignificant, the particles might be also resampled from an approximating continuous *PDF* (Pham, 2001). This is known as the Sequential Kernel Resampling Filter (SKRF). Moreover, even with resampling, the PF would still require a large number of particles to provide an accurate solution (Doucet et al., 2000). This makes brute-force implementation of the PF with computationally demanding atmospheric and oceanic models quite a challenging problem (Anderson, 2003; Snyder et al., 2008; Van Leeuwen, 2009).

6.2.2 Ensemble Kalman Filtering (EnKF)

To avoid the problems associated with the application of the PF and the KF with large dimensional nonlinear problems, (Evensen, 1994) introduced the EnKF as a hybrid approach between the KF and the PF. The basic idea behind this filter is to combine the optimal forecast step of the PF with a KF correction of the particles. The weights are then kept uniform. The algorithm of the EnKF can be summarized as follows:

- *Prediction step*: As in the PF, the analyzed particles, $\boldsymbol{x}_{k-1}^{a,i}$ are advanced in time with the model to compute the forecast particles $\boldsymbol{x}_k^{f,i}$.

- *Correction step*: A KF correction step is applied to every forecast particle as

$$\boldsymbol{x}_k^{a,i} \ = \ \boldsymbol{x}_k^{f,i} + \mathbf{G}_k^e \big(\boldsymbol{y}_k^i - \boldsymbol{H}_k(\boldsymbol{x}_k^{f,i}) \big). \qquad (6.7)$$

The gain matrix $\mathbf{G}_k^e$ is the same as the Kalman gain but is computed from the sample covariance matrix of the $\boldsymbol{x}_k^{f,i}$ as described by (Evensen, 2003)

In Eq. (6.7), the observation was assigned a superscript index associated with each particle. This is because the observation needs to be perturbed by noise sampled from the *PDF* of the observational error (Burgers et al., 1998).

The correction step of the EnKF uses only the first two moments of the particle ensemble, and is thus suboptimal for non-Gaussian systems. In practical situations, however, the EnKF was found to be more robust than the PF when small-size ensembles were used because the Kalman update of the particles is applied using the forecast error covariance matrices estimated from the particles ensemble. This made the implementation of the Bayesian filtering feasible with high dimensional systems, as in meteorology and oceanography. The KF correction reduces the collapse of the ensemble by 'pulling' the particles toward the true state of the system, allowing the filter to operate with a reasonable number of particles (Kivman, 2003; Hoteit et al., 2008; Van Leeuwen, 2009). With large enough ensembles, however, the PF was shown to outperform the EnKF (Nakano et al., 2007; Jardak et al., 2010). It is still an active area of research as to the defects of a Kalman filter type linear correction that can be overcome by using the fully nonlinear (non-Gaussian) Bayesian correction in filtering highly nonlinear systems such as the ocean or the atmosphere.

6.3   Lorenz-86 Model Description

6.3.1   Lorenz-86 Model

The model used in this study is that of Lorenz (1986), as modified by Wirosoetisno and Shepherd (2000) (hereafter WS00), and will be referred to here

as the extended Lorenz (1986) model or exL86. It has only 4 degrees of freedom, but admits both a fast gravity wave and a chaotic vortical mode, with an asymptotic, nonlinear balance between fast and slow variables. The advantage of models such as exL86 is that the balance between fast and slow variables is well understood, and the assimilated analysis can thus be easily interpreted in terms of the balanced and unbalanced components of the motion. The fact that this model is conservative does not pose a great difficulty, since the intention here is to use it to study assimilation algorithms in the context of the slow versus the fast variables. As pointed out by Lorenz (1986) and WS00, dissipation of gravity waves is not the cause of the existence of a slow manifold, and therefore models such as this one can be quite representative of realistic balanced dynamics.

The basic equations of the model are as follows:

$$\frac{d\phi}{dt} = w \tag{6.8}$$

$$\frac{dw}{dt} = -\frac{C}{2}sin(2\phi + 2\epsilon bx) \tag{6.9}$$

$$\frac{dx}{dt} = -\frac{z}{\epsilon} \tag{6.10}$$

$$\frac{dz}{dt} = \frac{x}{\epsilon} + \frac{bC}{2}sin(2\phi + 2\epsilon bx) \tag{6.11}$$

where $C = 1 + 0.8cos(0.92t)$, with t as time. $\epsilon = 0.1$ and $b = 0.71$ are two other constants.

Equations (8)-(11) describe a chaotic vortical mode in ϕ and w, coupled to a linear gravity wave in x and z. The four variables are the spectral coefficients of potential vorticity ϕ and w, geostrophic imbalance z, and divergence x. . Note that ϕ is actually related to the phase of two potential vorticity coefficients from the original derivation Lorenz (1986). The parameter b, which couples the fast and slow normal modes, corresponds to the rotational Froude number and the parameter ϵ is related to the parameter b and the Rossby number by the following equation:

$$\epsilon \equiv \frac{RoB}{\sqrt{1 + B^2}} \tag{6.12}$$

where $Ro = U/fL$ is the Rossby number and $B = fL/\sqrt{gH}$ is the rotational

Froude number. Ro is the ratio of the inertial timescale to the advective timescale of the flow. B is ratio of the Coriolis force to the gravitational restoring force. The value of these parameters indicates a timescale of separation between the different normal modes (Saujani and Shepherd, 2006). The model can be run in various configurations to mimic the dynamics of coupled and uncoupled scales of motion with only the slow varying mode active or in a slaved configuration with the fast varying mode slaved to the slow manifold.

6.3.2 Slow Manifold Initialization

The model can be configured in a slow manifold such that two variables vary at a slow time scale and the fast varying variables are set to be zero. The lowest order approximation to a slow manifold in the exL86 system is found by setting $x = z = 0$ and evolving only ϕ and w. For $\epsilon = 0$ or $b = 0$, this manifold is exact, and results in the single-timescale system

$$\frac{d\phi}{dt} = w \tag{6.13}$$

$$\frac{dw}{dt} = -\frac{C}{2}sin(2\phi) \tag{6.14}$$

This system is analogous to a chaotic pendulum when C is still time dependent in this configuration. This corresponds physically to the quasigeostrophic equations as in both systems the fast gravity waves are filtered out. To establish how nonlinearity of the slow mode affects data assimilation, experiments with this model are performed using the Ensemble Kalman Filter and the two flavors of the Nonlinear Particle Filter. Results are presented in section 6.4.

6.3.3 Second-order slaving relations

The model can also be configured in a slaved relations mode such that the fast varying modes are only dependent on the slow variables and are time independent.

$$x = -\frac{\epsilon}{2}Cbsin2\phi + O(\epsilon^3) \tag{6.15}$$

$$z = \epsilon^2(Cbwcos2\phi + \frac{C'}{2}bsin(2\phi))$$
$$+O(\epsilon^3) \tag{6.16}$$

where C' is the time derivative of C.

To assess the efficiency of the nonlinear analysis step in enhancing the dynamical balance of the filter solutions, identical twin assimilation experiments were designed such that the true state was balanced, but the observational errors projected onto all degrees of freedom, including the fast modes. Results are presented in section 6.4

6.3.4   Experiments setup and objectives

We set up experiments to test the performance of the EnKF compared to the two flavors of particle filters, the SIRF and the SKRF. The ExL86 model is configured in 3 different modes. The first configuration used is the slow manifold configuration of the model in which the fast variables were set to zero and only the slow variables were allowed to evolve in time. This model configuration is weakly nonlinear in its dynamics.

The second configuration considered is the slaved mode with the fast variables depending completely on the evolution of the slow variables and not evolving in time independently. This configuration of the model has the slow variable evolving in time uncoupled to the fast variable. Filtering on this configuration will help us understand how the linear vs the nonlinear filter improves the slow mode and hence also influences the evolution of the fast mode without coupling back to the slow mode.

The third configuration is the fully nonlinear mode with the slow and the fast variables coupled and evolving in time separately as the full dynamics dictates. This model configuration enables us to assess whether the filters are improving the fully nonlinear coupled dynamics of the model or only the slow or fast modes

individually. This would give us an insight into how important it is to have a linear vs a nonlinear correction step to capture the dynamics of a fully nonlinear coupled model.

In all experiments presented here, we chose a trajectory of the model starting from the same initial conditions of ϕ = -6.617, w = -0.449, x = 0 and z = 0. In all these three configurations with 3 different types of filters, we investigated two different sets of observation schemes. One observation scheme was to observe all variables at all time. This observation scheme is called the All observation experiment (AOEx hereafter). The second observation scheme was to observe only the first (slow) variable and the third (mixed) variable every 8 time steps. This observation scheme is referred to as the Sparse observation experiment (hereafter SpOEx). All assimilation experiments were done with 10 and 25 ensemble members. Results from the experiments with 25 ensemble members are presented in this study for the different filter solutions. An inflation factor of 1.01 was used for the EnKF simulations to account for subsampling errors in the EnKF (Hamill et al., 2001)

6.4   Results from experiments

Results from the experiments with the three separate modes of the model are presented in this section.

6.4.1   Slow Manifold

To separate the problem of balance from that of general nonlinearity and chaos, we establish how well the EnKF, SIRF and SKRF estimate the model state in the single-time-scale slow manifold configuration of the model. In the slow manifold case, only the variables ϕ and w are varying in time and variables x and z are zero at all time. When all variables at all time are observed in the assimilation experiments, the EnKF estimates the slow variable with low error comparable to that of the nonlinear filters' solutions as shown in Fig 6.1. This shows that when the model has only a slowly varying single time scale which is weakly nonlinear,

the nonlinear filters are comparable in estimating the state to the EnKF, which is based on Gaussianity assumptions. Similarly, in Fig 6.2, we see the solutions from the three assimilation schemes for the SpOEx. This experiment shows that the SKRF estimates the variable w with lesser RMSE than SIRF and is comparable to the EnKF RMSE (after a few timesteps of assimilation). The advantage of the PFs is that the balance of the dynamic variables relies only on a balanced forecast ensemble which is not changed by a linear correction step such as in an ensemble Kalman Filter. Neef et al. (2006) show that a more balanced error covariance in an EnKF is the reason it captures the dynamics better than an Extended Kalman Filter (EKF). They also argue that over-observing can lead to a more unbalanced forecast ensemble and thus to an unbalanced analysis, yet in our experiments, reduced observations lead to great errors in all three filters, and more so in the EnKF and SIRF.

6.4.2 Second-order slaving relations

In Fig 6.3, the model was configured as an approximation to the slow manifold, where the evolution of the system depends on the slow variables only. The fast variables are found diagnostically as functions of the slow variables, and the gravity wave is suppressed. It can be seen that the EnKF estimate does not capture the transition between the peaks in the variable z. The reason for this failure could be that the EnKF updates the ensemble trajectories using a linear analysis estimate and hence could destroy the nonlinear interactions between the variables, while the SIRF and SKRF only change the ensemble probabilities but do not modify their trajectory. Hence, the nonlinear filters could retain the balance relationship to the extent that ensemble members themselves are balanced and the forecasts in the ensemble use the full nonlinear model and the gravity wave is therefore bounded. This could be destroyed in the EnKF when, at every analysis step, the ensemble members themselves are updated using a linear correction step. The RMSE for variable z (fast variable) is lowest for the SKRF. The peaks in variable z are captured well by both the SKRF and SIRF estimates. The total RMSE is lowest for SKRF.

Fig 6.4 shows the model estimates for the same slaved mode configuration with sparse observations. Again, SKRF state estimates have the lowest RMSE compared to the SIRF and EnKF state estimates. As in Fig 6.3, the EnKF state estimate is unable to infer the transition between peaks in the variable z which is inferred better in the SIRF and SKRF solutions. Although variable w is estimated well by all three filters, the SKRF performs better with this variable. Hence, the nonlinear filter, especially with particles sampled from a continuous *PDF*, estimates the solutions to the highly nonlinear model with scale separation better in both slow and fast time scales. The balance relationship between the slow modes and fast modes are simulated better by the nonlinear filters with better-estimated fast-slow statistics used to update the fast variables with observations of the slow variables. This is also in agreement with the results of Neef et al. (2009) where it is shown that an estimate of the fast variables from observations of a slow variable alone requires the fast-slow error covariances to capture the balance relationship.

6.4.3   Nonlinear Mode

Fig 6.5 shows the total root mean-square error (RMSE) and the RMSE for variable w and z. The RMSE for all three filters, EnKF, SIRF and SKRF are comparable and low. This shows that when assimilating observations of all variables and at all timesteps in a nonlinear model with interacting slow modes and fast modes, all three filters capture the variables well and maintain the balance among the variables. The slow mode is captured better by the EnKF than the fast mode as seen in Fig 6.6, where we assimilate sparse observations. The EnKF state estimate of the unobserved slow mode variable w and fast variable z are worse than the estimates by the nonlinear filters SIRF and SKRF. The nonlinear filters are comparable to each other and perform well in estimating both the slow and fast variables. The transition between peaks in the fast variable are still not well captured in these two schemes, yet they do capture them well in time as compared to the EnKF solutions. This is consistent with results from Neef et al. (2006) where it is shown that a nonlinear evolution in the model such as in PFs slows the growth in imbalance in the model analysis and also allows for efficient assimilation

of sparser observations without a great loss of balance. Neef et al. (2006) also show that the ensemble averaging in the EnKF helps in keeping a balanced state over an Extended Kalman Filter-like approach. This advantage is even better preserved in the weighted mean of the PFs.

We have also tested the assimilation experiment with various ensemble sizes from 10 to 100 and have shown the total RMS error for each variable in each of the ensemble size cases in Figure 6.7. This figure shows that for the EnKF, increasing the ensemble size from 10 to 100 does not significantly change the skill of the filter. For the PFs, increasing the ensemble size from 10 to 50 improves the skill of the filters but further increase in the ensemble size does not gain much in terms of reducing the RMS error. Even an ensemble size of 50 is much above the dimension of the problem being solved. Yet to model the PDFs of each variable appropriately and integrate it forward in time, it is necessary to sample the variable PDFs sufficiently in order to capture the most information.

One of the main properties of this model is the nonlinearity in the interaction of different modes and the non-Gaussianity of the fast mode. Both the nonlinear coupling and the fast forcing imply non-Gaussian PDFs for the fast variable. Hence, the model was run for all three filters with 1000 ensemble members so as to get a good estimate of the prior and posterior estimate for the PDFs of the model variables for the fully nonlinear configuration. The PDFs of the state are estimated using a Gaussian Mixture Model (GMM), a parametric probability density function represented as a weighted sum of Gaussian component densities. (McLachlan and Peel, 2000; Anderson and Moore, 1979). Plotting the PDFs of the variables shows the non-Gaussian nature of the PDFs of the variables in the fully nonlinear case. Doucet et al. (2000) show theoretically that the estimated PDF from the PFs converge to the Bayesian PDF as the number of samples tend to infinity. The EnKF always approximated the PDF to be Gaussian but the particle filters are able to capture a non-Gaussian PDF and evolve it forward in time. This could be a critical reason for the PFs to perform better than the EnKF.

Fig 6.8 shows that in the forecast and the analysis, the particle filters capture the non-Gaussian PDFs in their ensemble spread. When we reduce the number

of observations in time, both the forecast and analysis *PDFs* conditioned on the observations increase in their spread, yet the PFs do have a non-Gaussian PDF which is likely to represent the non-Gaussianity of the system better as shown in Fig 6.9.

Neef et al. (2009) show that the EnKF analysis cycle can cause the ensemble to lock onto a gravity wave of the wrong amplitude, causing filter divergence in the analysis of the fast mode, even in regimes where it converges for the slow mode. Fast-mode filter divergence comes about because the linear gravity wave ensemble does not spread between observations. This drawback is not overcome even when observations are very frequent. In realistic applications it is possible that gravity waves that are present in the truth may not be represented in the observations, perhaps because of filtering or averaging of observations. In that case, only the component that is slaved to the slow mode can be controlled by observations, which requires the filter to simulate the balance relationships between slow and fast model variables.

Hence, the above experiments show that in estimating states with various timescales interacting and in balance, both the nonlinear filters give better estimates than the EnKF which is based on a linear Kalman correction. Estimates of both the slow varying variables and fast varying variables are improved by the nonlinear filters over the EnKF solutions. These solutions show that even with a weakly nonlinear model or a highly nonlinear model with interactions between the fast and slow variables, the nonlinear filters unequivocally give lesser error in estimates of the state variables.

6.5   Discussion and conclusions

Kalman filtering since its introduction five decades ago has been adapted as one of the most promising tools for data assimilation. The Kalman filter is an optimal linear filter. Hence, two different approaches are generally used for the implementation of this estimation technique to nonlinear models. The first approach consists of linearizing the model equations leading to the so-called ex-

tended Kalman filter. This approach has been shown to be either too prohibitive computationally or have limitations in reduction in error of estimation for strongly nonlinear systems with simplified versions of the filter. Another approach is to use linear-analysis based Kalman Filter for nonlinear estimation and is based on the ensemble approach and the use of nonlinear Monte-Carlo ensemble forecasting methods to represent estimation errors with an ensemble of state vectors. Until recently, these linearized filters have been shown to perform relatively well in state estimation of multi-dimensional nonlinear problems compared to other approximate methods like optimal interpolation. The two main disadvantages that plague all Kalman filter based approaches are that they do not produce the variance-minimizing estimate in the analysis step for nonlinear models and they initialize the Fokker-Planck-Kolmogorov equation with an ensemble that preserves only the first two moments of the analysis error statistics. It is also not completely understood how these filters influence the state estimation of different scales of dynamics.

Particle filters, on the other hand, are fully nonlinear in both model evolution and analysis steps (Doucet et al., 2001; Gordon et al., 1993). They use the full error statistics in filtering and hence minimize the true variance and not an assumed Gaussian variance. They are more suited for nonlinear estimation and nonlinear Monte-Carlo ensemble forecasting of highly nonlinear processes such as ocean-atmosphere dynamics than linear-based Kalman filter. Yet, a fundamental problem with PFs is the so-called curse of dimensionality, which is related to the fact that a relatively small number of model ensemble runs trying to estimate the a large-dimensional system space is very unlikely to be close to the set of observations from this system (Snyder et al., 2008). More complicated particle filters have been proposed that can overcome the 'curse of dimensionality' , but haven't been used in geoscience applications very much (Van Leeuwen, 2009). We have tested two such modified PFs, the SIRF and the SKRF to understand how these filters influence the estimation of different scales of dynamics.

In this chapter, we have compared the efficiency of the EnKF with the two flavors of nonlinear particle filters, the SIRF and the SKRF, for problems (i) where there exists a separation of time scales between relatively fast and slow motions,

(ii) where the free fast motion is oscillatory, and (iii) where the evolution of the fast variables in the true state is slaved to that of the slow. These experiments showed that the SKRF, SIRF and EnKF have quite different properties when it comes to preserving balance in the assimilated analysis. The PFs always outperformed the EnKF with any of the tested schemes of observation frequencies or modes of the model. This strongly suggests that a filter preserving the nonlinearity in the forward model tends to also preserve the balance in the model.

Application of particle filters is attractive from the viewpoint that they use the full error statistics to integrate the Fokker-Planck-Kolmogorov equations of the system unlike a Kalman filter which uses only the first two moments in its integration. Hence, they are a truly variance minimizing scheme. Numerical results from experiments with the exL86 show that nonlinear filters behave much better than the ensemble Kalman filter methods with strongly nonlinear systems. The nonlinear filters also better preserve the dynamical balance of the system state resulting in more stable predictions in the slow and fast variables. Particle Filters, esp. SKRF, capture slaved modes better implying nonlinear jumps in dependent variables are simulated better. When the observation frequency and the number of variables observed are decreased, the nonlinear filters show a very clear improvement in performance compared to the linear-analysis-based Kalman filter estimations for both the slow and fast variables in all configurations of the model. This is very important for atmospheric and oceanic data assimilation where only a small fraction of the system state is observed.

This study is intended as a complement to similar studies such as Neef et al. (2006) and studies involving larger, more complicated models, such as Mitchell et al. (2002). Key points of the balance problem and drawbacks of linear assumptions in estimation theory compared to nonlinear filters highlighted in this study add to the research in the still-evolving field of 4D data assimilation. This research can be extended to study the balance dynamics in more complicated models to understand the behavior of nonlinear filters in systems with strong nonlinearity.

6.6   Acknowledgements

Figure 6.1: Slow Manifold : Every variable at all time steps is observed. The system is known perfectly. It can be observed that both EnKF and PFs capture the slow manifold well when all variables are observed.
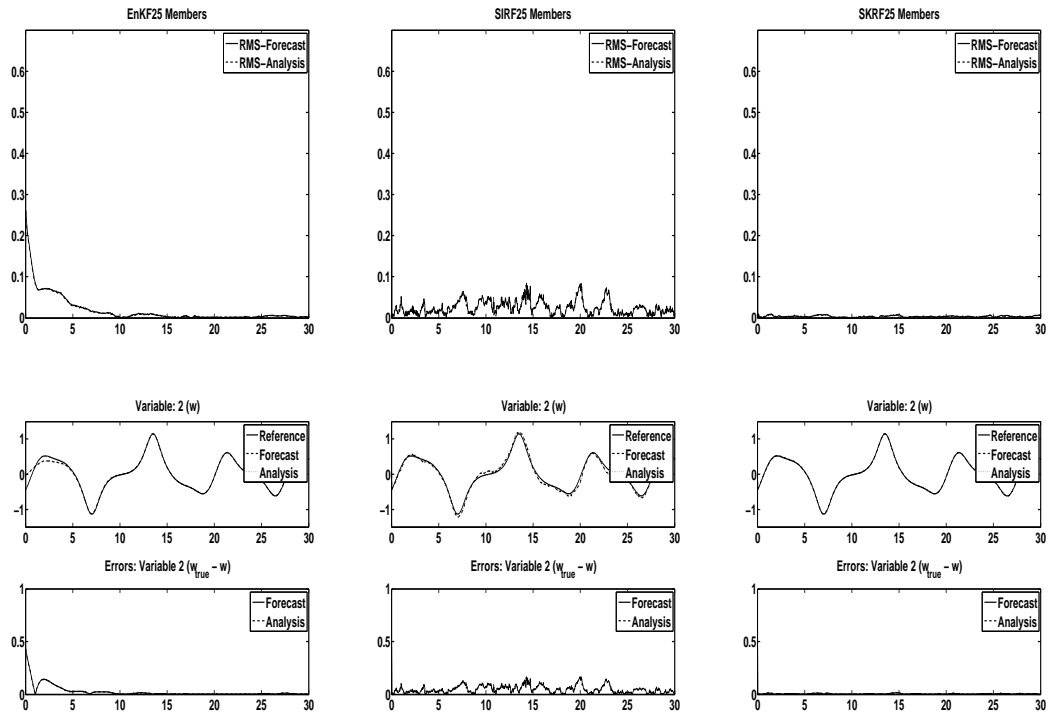
Figure 6.2: Slow Manifold : First and third variable at every 8th timestep is observed. Here we observe that the system is not well captured by the EnKF analysis where as the PFs capture the system well.
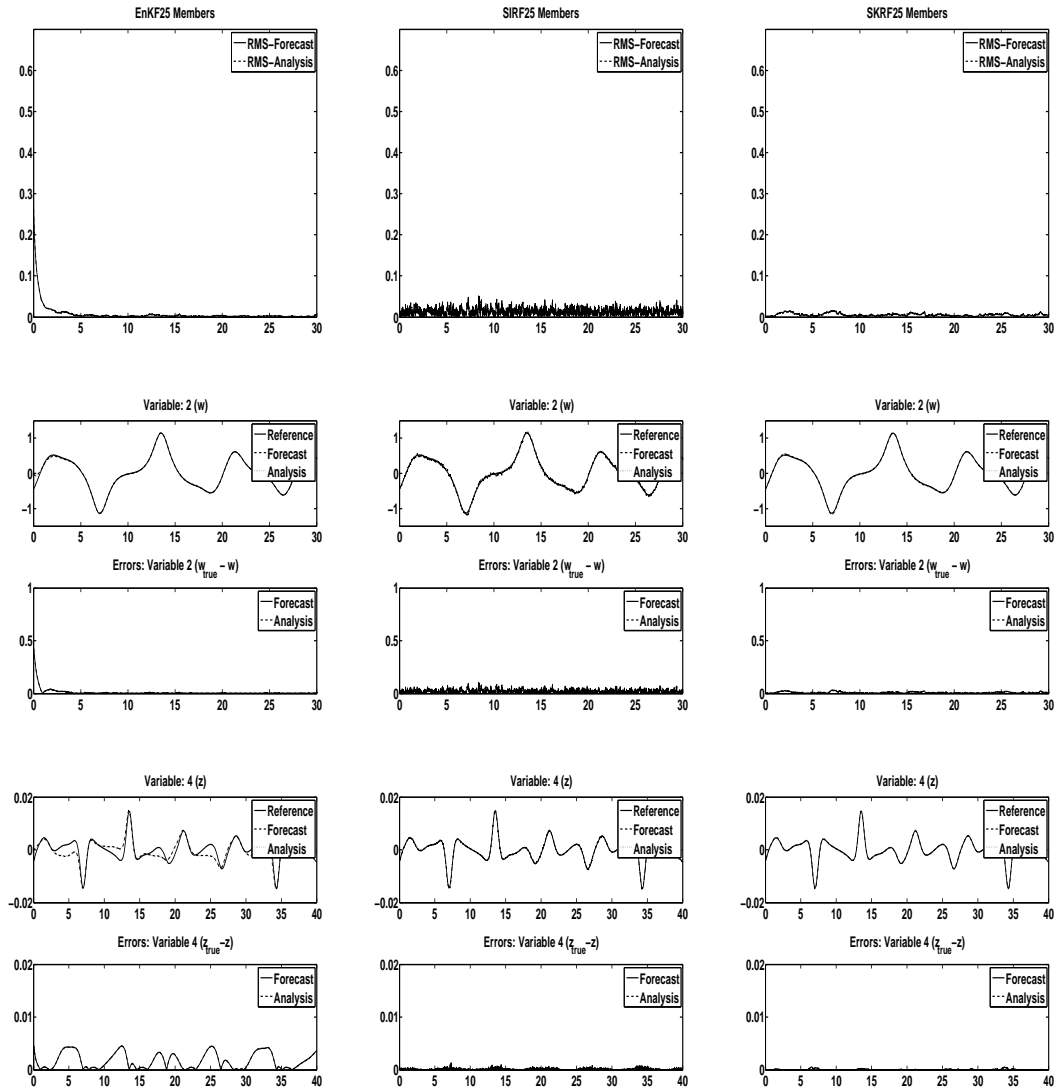
Figure 6.3: Slaved Manifold : Every variable at all time steps is observed. The system is known perfectly. It can be observed that both EnKF and PFs capture the slow manifold well when all variables are observed.
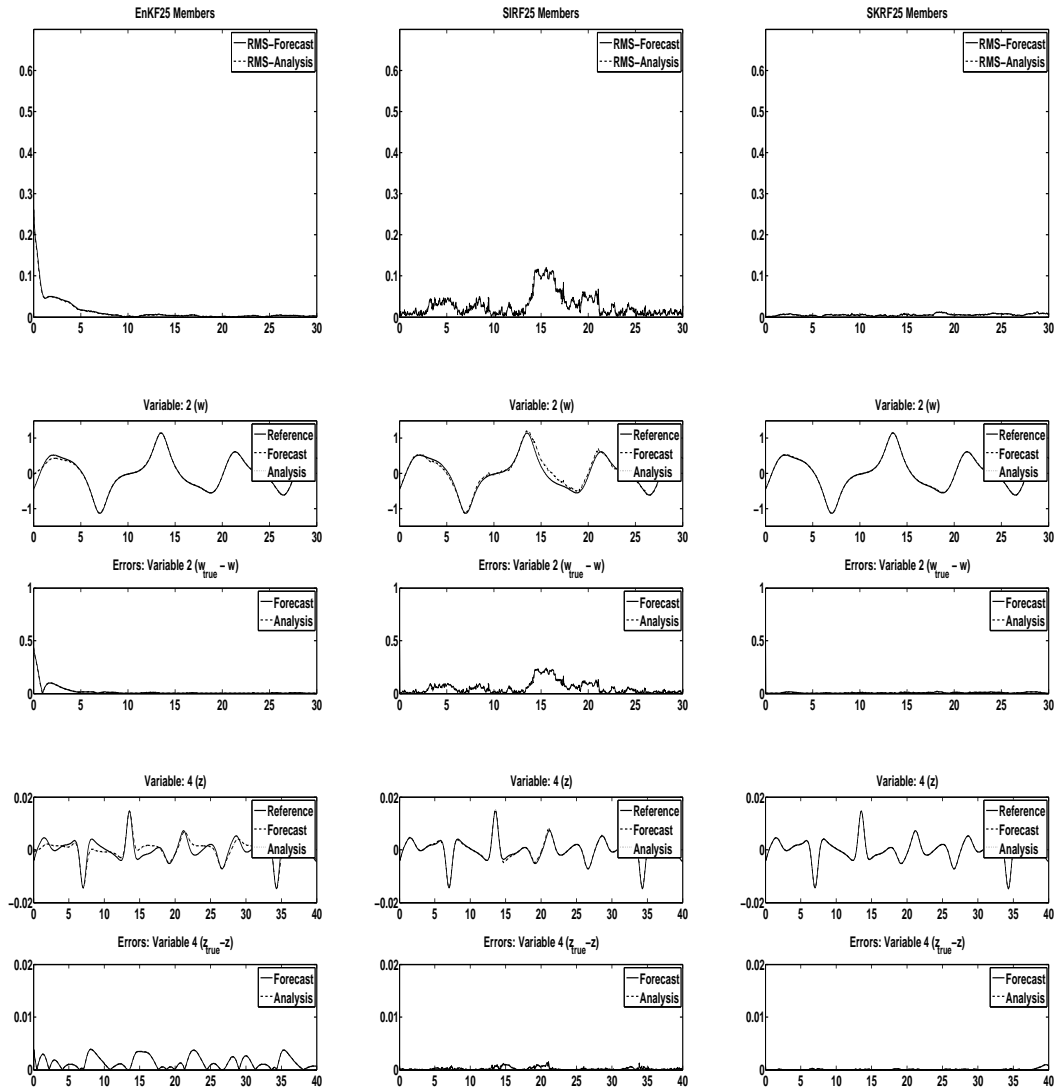
Figure 6.4: Slaved Manifold : First and third variable at every 8th timestep is observed. Here we observe that the system is not well captured by the EnKF analysis where as the PFs capture the system well.
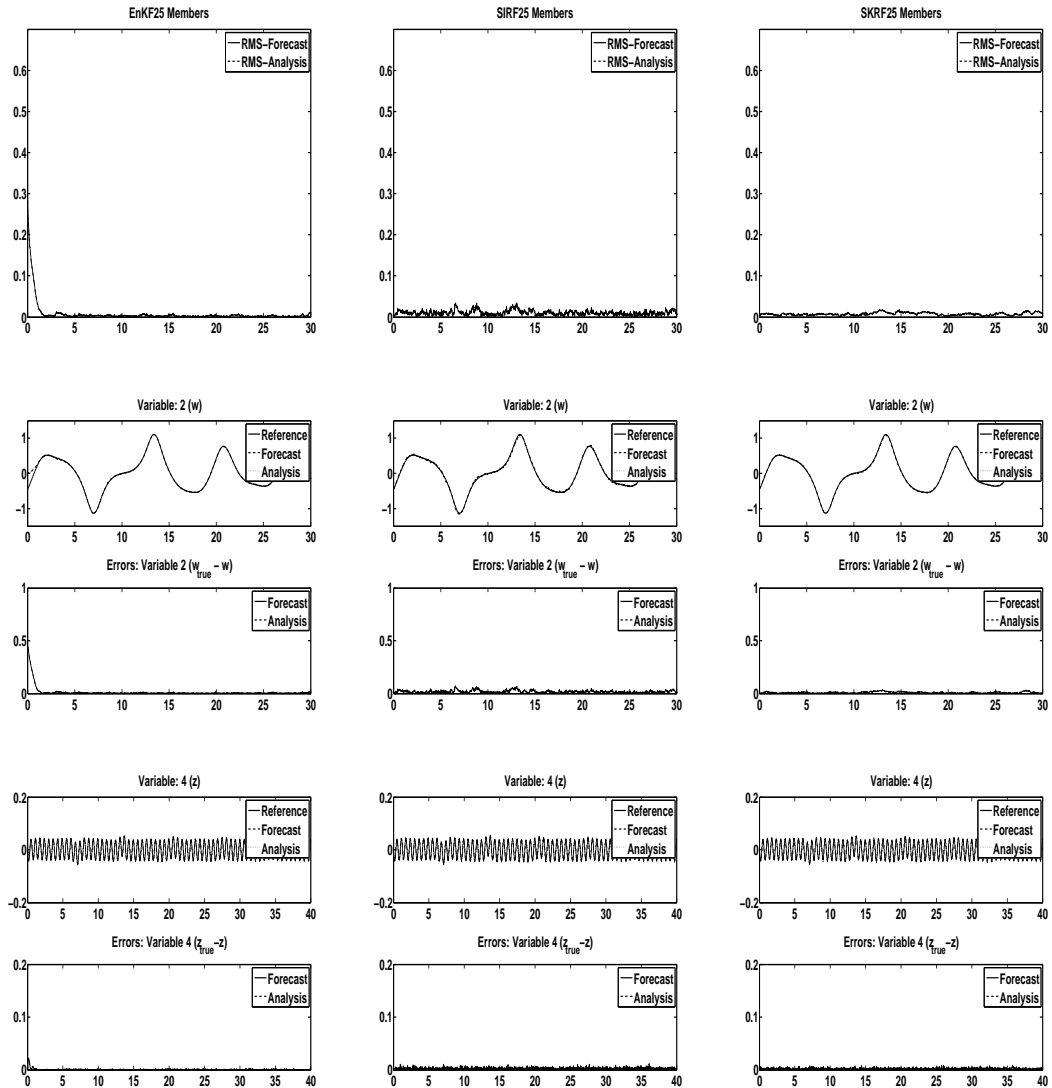
Figure 6.5: All Modes : Every variable at all time steps is observed. The system is known perfectly. It can be observed that both EnKF and PFs capture the slow manifold well when all variables are observed.
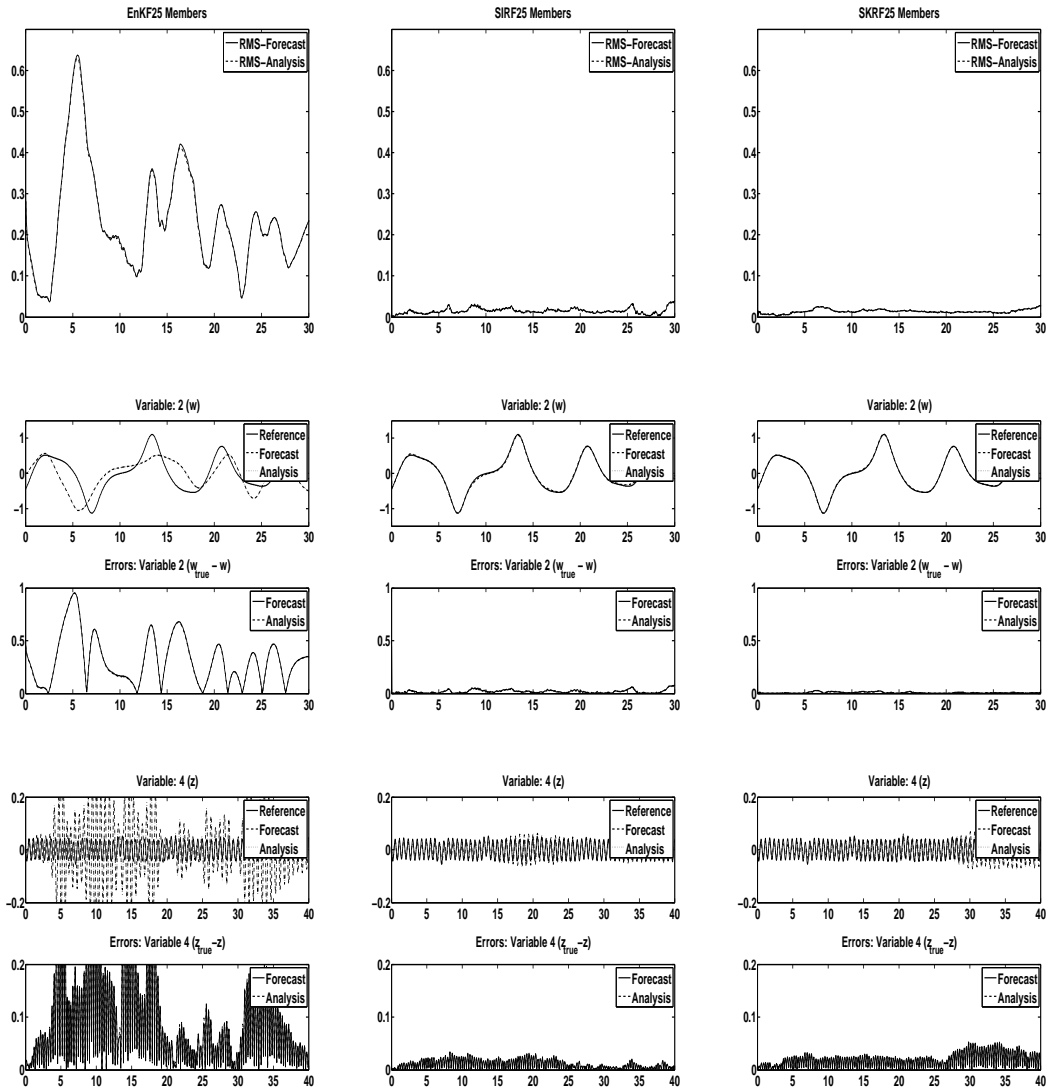
Figure 6.6: All Modes : First and third variable at every 8th timestep is observed. Here we observe that the system is not well captured by the EnKF analysis where as the PFs capture the system well
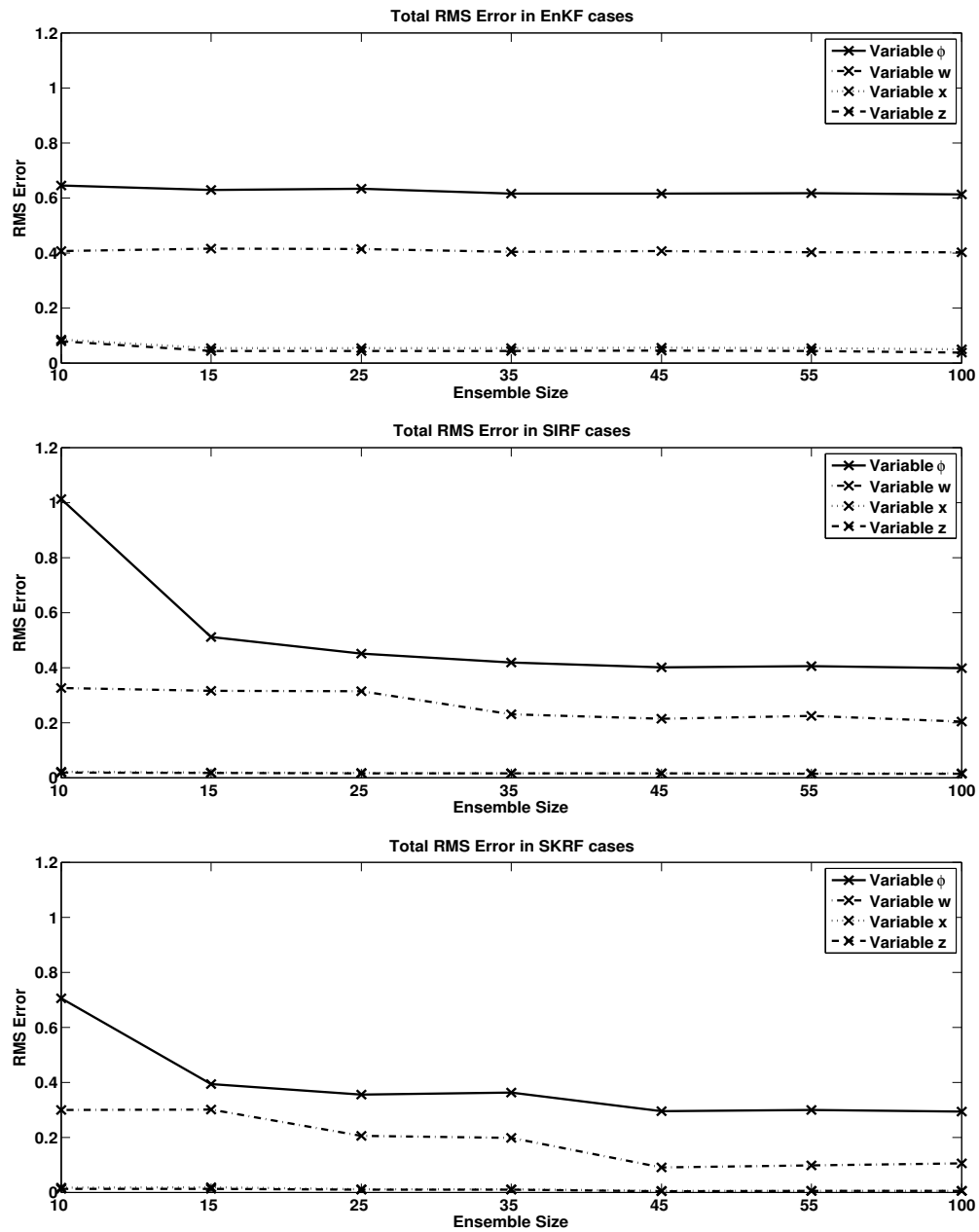
Figure 6.7: Comparison of average error for all the four variables in the All Modes configuration of the model with observations taken at every 8th timestep. Top panel shows the errors for the EnKF, middle panel for the SIRF and the bottom panel for the SKRF filters.
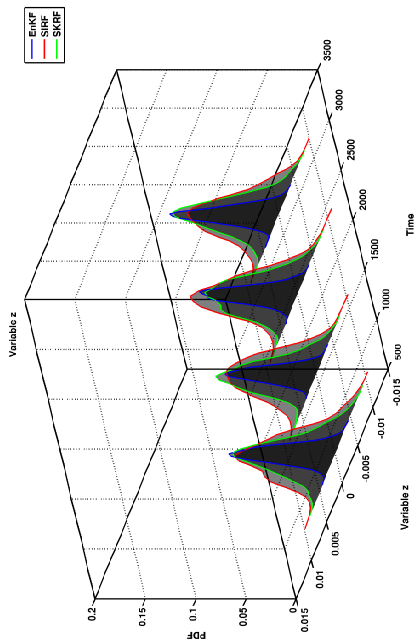
(a) Variable 2 Forecast
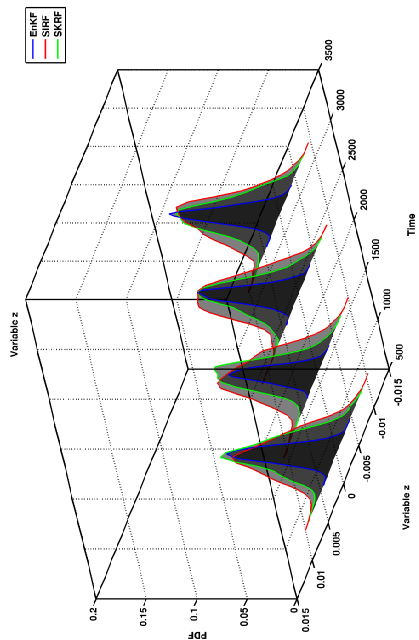
(b) Variable 4 Forecast
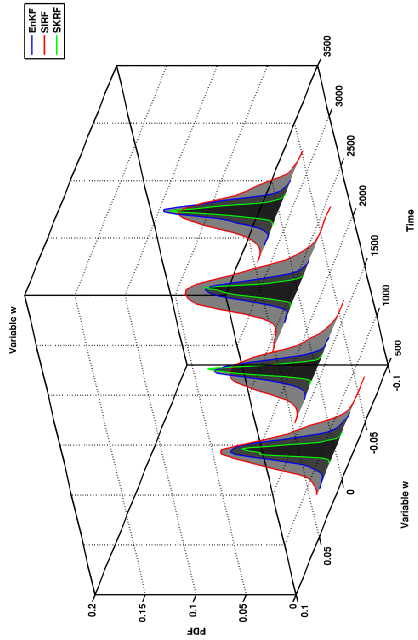
(c) Variable 2 Analysis
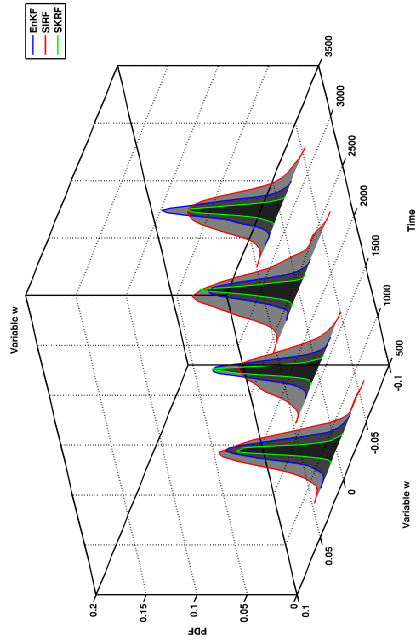
(d) Variable 4 Analysis

Figure 6.8: All Manifold : PDFs of forecast and analysis variables w and z for All modes case estimated using a Gaussian mixture model are shown as a function of time.The filters were run with observations taken at every timestep of the model run and the ensemble size of the filters were 1000 ensemble members.
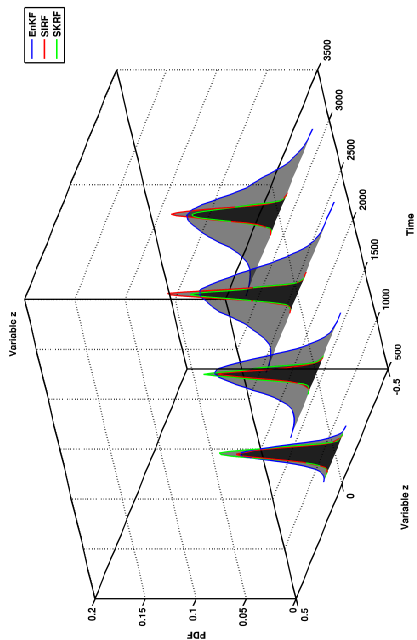
(a) Variable 2 Forecast
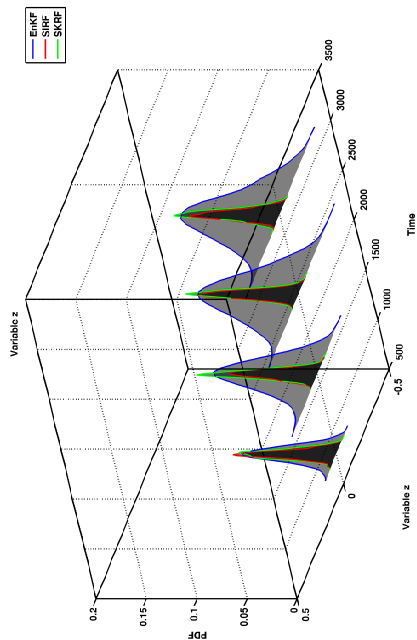
(b) Variable 4 Forecast
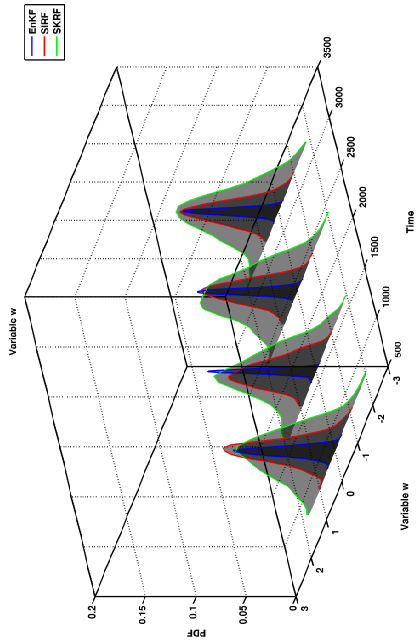
(c) Variable 2 Analysis
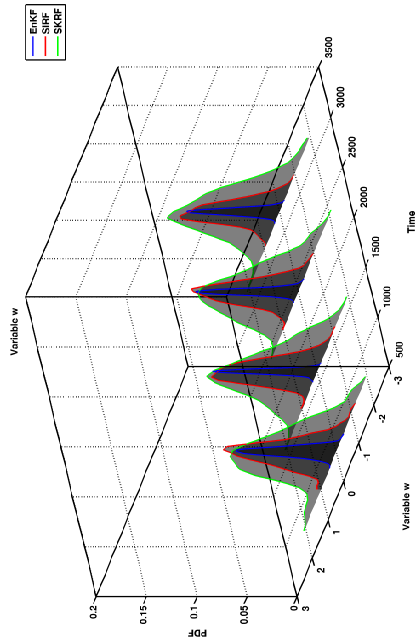
(d) Variable 4 Analysis

Figure 6.9: All Manifold : PDFs of forecast and analysis variables w and z for All modes case estimated using a Gaussian mixture model are shown as a function of time. The filters were run with observations taken at every 8th timestep of the model run and the ensemble size of the filters were 1000 ensemble members.

Chapter 7

Concluding remarks

In this concluding chapter we summarize the results of the Dissertation, with an emphasis on novelties, and new problems suggested by this research.

7.1 Final Remarks

Lewis Fry Richardson once had a dream : " Perhaps some day in the dim future it will be possible to advance the computations faster than the weather advances and at a cost less than the saving to mankind due to the information gained . But that is a dream." (Richardson, 1922). That dream had been fulfilled within the last few years of Richardson's life. Numerical models integrated on the first ENIAC machine were able to time step the equations forward to generate a forecast although erroneous due to the the huge approximations made for the computation to be feasible. Much of a similar battle is being fought even today in climate modeling. Although the computational resources have grown exponentially with Moore's law, since the 1950s, our modeling of the climate system and its interlinked processes are still wrought with many approximations and parameterizations due to lack of enough resources to resolve all scales of the dynamics.

At the outset of this Dissertation, we noted that the main challenges in numerical atmosphere-ocean modeling today are to resolve dynamics that are possible with today's synoptic scale resolution atmosphere models and mesoscale resolving

ocean models. The primary challenge in today's climate models is to resolve the MJO characteristics well, which lies at the interface of dynamics and thermodynamics and between seasonal and annual time periods. The primary challenge in ocean modeling with regional ocean models is to resolve ocean mesoscale eddies accurately and realistically. In this thesis, we investigated some properties of the improved MJO simulations in CCSM4 and then went on to study MJO's concurrence with various other climate phenomena. We also studied the change in MJO response in a warmer world. Next we assimilate ship cruise and satellite observed data to capture mesoscale features in a high resolution region ocean model of the Southeast Pacific region. After getting a state estimate of the ocean, we study the properties of the eddy and also analyze the heat budget in the region during the period of the cruise. Lastly we study how linearized filters can disrupt balance in atmosphere-ocean models by using a simplified proxy model for the same. We show that using a nonlinear filter which preserves the nonlinearity in the filtering step helps preserve the balance better.

7.2   Contributions of the Dissertation

The main contributions from the thesis can be summarized in the following paragraphs.

MJO in CCSM4

Simulating and forecasting the MJO is of central importance to the global climate and weather community, especially as models continue to increase resolution and resolve the various processes that contribute to intraseasonal variability. Yet most climate models today fail to simulate even the large-scale features of the MJO. In Chapter 2, we evaluate the performance of a 20-year run of CCSM4 in reproducing the primary characteristics of MJO, based on diagnostics established by the MJOWG.

CCSM4 produces coherent, broadbanded and energetic patterns in eastward

propagating intraseasonal zonal winds and OLR in the tropical Indian and Pacific Oceans that are generally consistent with MJO characteristics. Strong peaks occur in coherence spectra with periods between 20-100 days and zonal wavenumbers between 1 and 3. Model MJO's, however, tend to be more broadbanded in frequency than observation, with higher frequencies being associated with zonal wavenumbers in the MJO band. But broadscale patterns, as revealed in combined EOFs of U850, U200 and OLR, are remarkably consistent with observations and indicate that convective coupling occurs in the simulated MJOs.

MJO and Earth's Climate

Relations between MJO and other climate phenomena were explored as well, but no overwhelmingly strong links between ENSO state, Monsoonal flow or Indian Ocean Dipole mode were identified. In these short, 20-year runs, a tendency for MJO to be more energetic during weak warm ENSO conditions, negative Monsoon Hadley flow, and positive zonal shear, was noted. But longer runs and more detailed dynamical analysis will be needed to better understand what processes control MJO and what climate processes respond to MJO in CCSM4.

Increase in variance of precipitation and especially the variance in the intraseasonal precipitation indicates a more active hydrological cycle in global warming scenarios as seen in several previous studies. A histogram plot of the MJO amplitude and number of days shows an increase in the higher amplitude MJO active days and also in the very low or no MJO days. The net number of days with average MJO amplitude reduces in the global warming scenario. This is consistent with previous studies showing extreme precipitation events amplify in a warmer atmosphere (Allan and Soden, 2008). It is also observed that the model MJOs are active (with amplitude greater than one) for significantly higher number of days in the Indian Ocean and W. Pacific with higher amplitudes in the warmer atmosphere.

ROMS Data Assimilation: VOCALS fits

15 day Data assimilation fits over the PCCS region have been successfully conducted for Nov 2008 using the observations from both remotely sensed data and in situ data. ROMS I4D-VAR reduced the normalized absolute error (NAE) near the observational error level for all variables except for the upper level temperature. The statistical information of SSH, T and S plotted in the Taylor diagram showed the improvement of the correspondence between the data-assimilated model states and observed states.

Eddy structure, properties and heat content in the SEP

Eddy properties in the PCCS are studied with a high-resolution (dx = 7 km) regional model ocean state estimate and an altimetry analysis, using eddy tracking methods. The analysis of model eddies show that eddy signals penetrate to 800-1500 m in depth. Cyclonic eddies featured a shoaling salinity minimum layer (SML), doming isopycnals near the surface. Anticyclonic eddies were characterized by a depressed SML and depressed isopycnals in the upper ocean. An intensively surveyed cyclonic eddy was characterized by high salinity as predicted by Johnson and McTaggart (2010). The eddy had an average temperature anomaly of approximately -0.4^{o}C over a depth range from 100 - 700 m and features a cold anomaly of approximately -1°C near 150 m depth. The net temperature anomaly of the eddy depends on the depth to which it is integrated, though it is negative overall. The cold near-surface anomaly, caused by the doming of near-surface isopycnals, is likely more relevant than the net anomaly for assessing the effect of eddies on upper-ocean temperature, as it is more likely to be incorporated into the mixed layer. The vertically-integrated heat content of anticyclonic eddies determined from the ocean state estimate is only slightly different from that of cyclonic eddies. The heat balance for the period of the cruise from the ocean state estimate reveals that the mean horizontal advection is the dominant term that balances the temperature tendency of the upper layer of the ocean. The vertical diffusion is secondary and is about 30% of the advection magnitude. One of the major sources of cooling that balances the positive surface heat fluxes is advection dominated

by geostrophic transport. These results are partially consistent with those from observations described in Colbo and Weller (2007). Major terms of the heat equation in the upper 400 m were also calculated over the region of the cruise. The heat transport produced by geostrophic transport is one of the primary sources of cooling in the entire stratus region because of its spatial coherence (Zheng et al., 2010).

Balanced Dynamics in a Linear vs Nonlinear Filtering problem

Kalman filtering since its introduction five decades ago has been adapted as one of the most promising tools for data assimilation. The Kalman filter is an optimal linear filter. Hence, two different approaches are generally used for the implementation of this estimation technique to nonlinear models. The first approach consists of linearizing the model equations leading to the so-called extended Kalman filter. This approach has been shown to be either too prohibitive computationally or have limitations in reduction in error of estimation for strongly nonlinear systems with simplified versions of the filter. Another approach is to use linear-analysis based Kalman Filter for nonlinear estimation and is based on the ensemble approach and the use of nonlinear Monte-Carlo ensemble forecasting methods to represent estimation errors with an ensemble of state vectors. Until recently, these linearized filters have been shown to perform relatively well in state estimation of multi-dimensional nonlinear problems compared to other approximate methods like optimal interpolation. The two main disadvantages that plague all Kalman filter based approaches are that they do not produce the variance-minimizing estimate in the analysis step for nonlinear models and they initialize the Fokker-Planck-Kolmogorov equation with an ensemble that preserves only the first two moments of the analysis error statistics. It is also not completely understood how these filters influence the state estimation of different scales of dynamics.

Particle filters, on the other hand, are fully nonlinear in both model evolution and analysis steps (Doucet et al., 2001; Gordon et al., 1993). They use the full error statistics in filtering and hence minimize the true variance and not an assumed Gaussian variance. They are more suited for nonlinear estimation and

nonlinear Monte-Carlo ensemble forecasting of highly nonlinear processes such as ocean-atmosphere dynamics than linear-based Kalman filter. Yet, a fundamental problem with PFs is the so-called curse of dimensionality, which is related to the fact that a relatively small number of model ensemble runs trying to estimate the a large-dimensional system space is very unlikely to be close to the set of observations from this system (Snyder et al., 2008). More complicated particle filters have been proposed that can overcome the 'curse of dimensionality' , but haven't been used in geoscience applications very much (Van Leeuwen, 2009). We have tested two such modified PFs, the SIRF and the SKRF to understand how these filters influence the estimation of different scales of dynamics.

In chapter 6, we have compared the efficiency of the EnKF with the two flavors of nonlinear particle filters, the SIRF and the SKRF, for problems (i) where there exists a separation of time scales between relatively fast and slow motions, (ii) where the free fast motion is oscillatory, and (iii) where the evolution of the fast variables in the true state is slaved to that of the slow. These experiments showed that the SKRF, SIRF and EnKF have quite different properties when it comes to preserving balance in the assimilated analysis. The PFs always outperformed the EnKF with any of the tested schemes of observation frequencies or modes of the model. This strongly suggests that a filter preserving the nonlinearity in the forward model tends to also preserve the balance in the model.

7.3   Future Directions

Frontiers in modeling multi-scale interactions in the climate system are being addressed by the climate modeling now that the capability to model scales of 10s of kilometers are slowing being tested and tuned for in the global climate models. Using these high resolution climate models or regional downscaled high resolution numerical models, dynamical features of ocean-atmosphere flow never modeled before can be studied and learnt from in a unique way.

One of the challenging problems still is to model a realistic MJO event

with all the scales of motion more realistic than any of the current climate models are able to achieve. The best climate models today can model the large scale features of the MJO well with modified convective parameterization schemes and higher resolution grids. Yet, they still seem to lack some fundamental physical, thermodynamical or a coupled process that is key to model the MJO. A large field campaign to observe a live MJO was launched a few months ago. The field campaign called DYNAMO, which stands for "DYNAmics of the MJO" was lucky enough to witness atleast a couple of MJOs and gather rich data of the vertical and horizontal structure of the MJO. It should be very educational to study the key processes that were active during an active MJO and study how the global climate models can be improved to include these processes and hence a better MJO simulation.

Another open problem is to model ocean mesoscale eddies with or without data assimilation, realistically so as to be able to understand various physics associated with ocean eddies such as mixing up nutrients for biological activity or transporting heat and changing the physical structure of the ocean. Hence, being able to model ocean eddies better in regional and global models will improve our capabilities to understand the impact of small scale dynamics on large scale changes such as the global heat budget or impacts on water mass movements around the globe.

A third open problem with regard to studying balance preserving data assimilation techniques is to user higher hierarchical models and understand which part of the dynamics are being lost or destroyed by using data assimilation techniques of today which are not formulated to preserve balance in the dynamics.

7.4   Concluding Thought

Although, our understanding of the climate system will steadily increase with increased capabilities of climate modeling in the coming decades, this is threatened by a growing gap between high resolution simulations and understand-

ing the physics behind certain complex ocean-atmospheric phenomena. In order to fill this gap, climate scientists must study the system using a suite of hierarchical models of varying complexity. Thus we can work towards a goal of having a deeper understanding of the fundamental processes which interact and control our Earth's climate and simultaneously have capability to numerically model and predict changes that could occur (some devastatingly so). While climate modelers and theorists lay the foundations for the future generations of climate models, the study of the various interlinked processes of the climate system must continue and form the pillars on which one can develop the generalized theory of earth's climate system. The ultimate fruits of this labour include, a better understanding of the baffling complexity around us, better solutions for related practical problems such as climate prediction - and perhaps, as Wigner (1960) called it - "unreasonable effectiveness of mathematics" - and finally, its own beauty.

Bibliography

Ajayamohan, R. S., Rao, S. A., and Yamagata, T. (2008). Influence of Indian Ocean Dipole on Poleward Propagation of Boreal Summer Intraseasonal Oscillations. *Journal of Climate*, 21(21):5437–5454.

Allan, R. P. and Soden, B. J. (2008). Atmospheric Warming and the Amplification of Precipitation Extremes. *Science*, 321(5895):1481–1484.

Anderson, B. and Moore, J. B. (1979). *Optimal filtering.* Information and System Sciences Series. Prentice-Hall Information and System.

Anderson, D. L. T., Sheinbaum, J., and Haines, K. (1996). Data assimilation in ocean models. *Reports on Progress in Physics*, 59:1209–1266.

Anderson, D. L. T. and Willebrand, J. (1988). *Oceanic Circulation Models: Combining Data and Dynamics.* Kluwer Academic Publications, Boston/London.

Anderson, J. (2001). An ensemble adjustment Kalman filter for data assimilation. *Monthly Weather Review*, 129(12):2884–2903.

Anderson, J. (2003). A local least squares framework for ensemble filtering. *Monthly Weather Review*, 131:634–642.

Annamalai, H., Murtugudde, R., Potemra, J., Xie, S., Liu, P., and Wang, B. (2003). Coupled dynamics over the indian ocean: Spring initiation of the zonal mode. *Deep-Sea Research Part II*, 50(12-13):2305–2330.

Annamalai, H. and Slingo, J. (2001). Active/break cycles: Diagnosis of the intraseasonal variability of the Asian summer monsoon. *Climate Dynamics*, 18(1-2):85–102.

Anthes, R. A. (1974). Data assimilation and initialization of hurricane prediction models. *J. Atmos. Sci.*, 31:702–719.

Behera, S., Krishnan, R., and Yamagata, T. (1999). Unusual ocean-atmosphere conditions in the tropical Indian Ocean during 1994. *Geophysical Research Letters*, 26(19):3001–3004.

Bennett, A. (2002). *Inverse modeling of the ocean and atmosphere.* Cambridge Univ.

Bennett, A. F. (1992). *Inverse Methods in Physical Oceanography.* Cambridge University Press, Cambridge.

Bergman, J., Hendon, H., and Weickmann, K. M. (2001). Intraseasonal air-sea interactions at the onset of El Nino. *Journal of Climate*, 14(8):1702–1719.

Bergthorsson, P. and Döös, B. (1955). Numerical weather map analysis. *Tellus*, 7:329–340.

Bessafi, M. and Wheeler, M. (2006). Modulation of South Indian Ocean tropical cyclones by the Madden-Julian Oscillation and convectively coupled equatorial waves. *Monthly Weather Review*, 134(2):638–656.

Biello, J. A. and Majda, A. J. (2005). A New Multiscale Model for the Madden–Julian Oscillation. *Journal of the Atmospheric Sciences.*

Bretherton, C. S., Uttal, T., and Fairall, C. W. (2004). The EPIC 2001 stratocumulus study. *Bulletin of the American Meteorological Society.*

Bryan, K. (1969). A numerical method for the study of the circulation of the world ocean. *Journal of Computational Physics*, 4:347–376.

Bryan, K. (1987). Potential vorticity in models of the ocean circulation. *Quarterly Journal of the Royal Meteorological Society*, 113:713–734.

Burgers, G., Jan van Leeuwen, P., and Evensen, G. (1998). Analysis scheme in the ensemble Kalman filter. *Monthly Weather Review*, 126(6):1719–1724.

Camargo, S., Wheeler, M., and Sobel, A. (2009). Diagnosis of the MJO modulation of tropical cyclogenesis using an empirical index. *Journal of the Atmospheric Sciences*, 66(10):3061–3074.

Capet, X., Colas, F., Penven, P., Marchesiello, P., and McWilliams, J. (2008). Eddies in eastern boundary subtropical upwelling systems. *Ocean modeling in an Eddying regime, Geophysical monograph series.*

Carton, J. A. and Hackert, E. C. (1990). Data assimilation applied to temperature and circulation in the tropical atlantic 1983-1984. *Journal of Physical Oceanography*, 20:1150–1165.

Carvalho, L. and Jones, C. (2002). Intraseasonal large-scale circulations and mesoscale convective activity in tropical South America during the TRMM-LBA campaign. *Journal of Geophysical Research.*

Carvalho, L. M. V., Jones, C., and Liebmann, B. (2002). Extreme Precipitation Events in Southeastern South America and Large-Scale Convective Patterns in the South Atlantic Convergence Zone. *Journal of Climate*, 15:2377–2394.

Cassou, C. (2008). Intraseasonal interaction between the Madden-Julian oscillation and the North Atlantic Oscillation. *Nature*, 455(7212):523–527.

Chaigneau, A., Gizolme, A., and Grados, C. (2008). Mesoscale eddies off Peru in altimeter records: Identification algorithms and eddy spatio-temporal patterns. *Prog. Oceanogr.*

Chaigneau, A., Le Texier, M., and Eldin, G. (2011a). Vertical structure of mesoscale eddies in the eastern South Pacific Ocean: A composite analysis from altimetry and Argo profiling floats. *Journal of Geophysical Research.*

Chaigneau, A., Le Texier, M., Eldin, G., Grados, C., and Pizarro, Ó. (2011b). Vertical structure of mesoscale eddies in the eastern South Pacific Ocean: A composite analysis from altimetry and Argo profiling floats. *J Geophys Research.*

Chaigneau, A. and Pizarro, O. (2005). Mean surface circulation and mesoscale turbulent flow characteristics in the eastern South Pacific from satellite tracked drifters. *Journal of Geophysical Research.*

Chelton, D. B., Gaube, P., Schlax, M. G., Early, J. J., and Samelson, R. M. (2011). The Influence of Nonlinear Mesoscale Eddies on Near-Surface Oceanic Chlorophyll. *Science.*

Chelton, D. B., Schlax, M., Samelson, R. M., and de Szoeke, R. (2007). Global observations of large oceanic eddies. *Geophysical Research Letters.*

Colas, F., Mcwilliams, J. C., Capet, X., and Kurian, J. (2011). Heat balance and eddies in the Peru-Chile current system. *Climate Dynamics.*

Colbo, K. and Weller, R. (2007). The variability and heat budget of the upper ocean under the Chile-Peru stratus. *Journal of Marine Research.*

Combes, V., Di Lorenzo, E., Gómez, F., Hormazabal, S., Strub, T., and Putrasahan, D. (2009). Modeling interannual and decadal variability in the humboldt current upwelling system. *Journal of Physical Oceanography.*

Cornuelle, B. D., Chereskin, T. K., Niiler, P. P., Morris, M. Y., and Musgrave, D. L. (2000). Observations and modeling of a California undercurrent eddy. *Journal of Geophysical Research.*

Correa-Ramirez, M. A., Hormazábal, S., and Yuras, G. (2007). Mesoscale eddies and high chlorophyll concentrations off central Chile (29 °–39 °S). *Geophysical Research Letters.*

Courtier, P. and Talagrand, O. (1990). Variational assimilation of meteorological observations with the direct and adjoint shallow-water equations. *Tellus A*, 42(5):531–549.

Cressman, G. P. (1959). An operational objective analysis system. *Monthly Weather Review*, 87(10).

Cressman, G. P. and Gilchrist, B. (1954). An experiment in objective analysis. *Tellus*, 6(4).

Dai, A. (2006). Precipitation Characteristics in Eighteen Coupled Climate Models. *Journal of Climate*.

Danabasoglu, G., Bates, S., Briegleb, B., Jayne, S., Jochum, M., Large, W. G., Peacock, S., and Yeager, S. G. (2011). The CCSM4 ocean component. *Journal of Climate*.

De Mey, P. (1997). *Data assimilation at the oceanic mesoscale: A review.* JOURNAL-METEOROLOGICAL SOCIETY OF JAPAN SERIES 2.

de Szoeke, S., Fairall, C., Wolfe, D., Bariteau, L., and Zuidema, P. (2010). Surface flux observations on the southeastern tropical Pacific Ocean and attribution of SST errors in coupled ocean-atmosphere models. *Journal of Climate*.

Dee, D. (1991a). Simplification of the kalman filter for meteorological data assimilation. *Q. J. R. Meteorol. Soc.*

Dee, D. (1991b). Simplification of the Kalman filter for meteorological data assimilation. *Quarterly Journal of the Royal Meteorological Society*, 117:365–384.

Derber, J. and Rosati, A. (1989). A global oceanic data assimilation system. *Journal of Physical Oceanography*, 19(9):1333–1347.

Deser, C., Phillips, A., Tomas, R., Okumura, Y., Alexander, M., Capotondi, A., Scott, J., Kwon, Y., and Ohba, M. (2011). ENSO and Pacific Decadal Variability in Community Climate System Model Version 4. *Journal of Climate*.

Di Lorenzo, E., Moore, A., Arango, H. G., Cornuelle, B., Miller, A., Powell, B., Chua, B., and Bennett, A. F. (2007). Weak and strong constraint data assimilation in the inverse Regional Ocean Modeling System (ROMS): Development and application for a baroclinic coastal upwelling system. *Ocean Modelling*.

DiNezio, P. N., Clement, A. C., Vecchi, G. A., Soden, B. J., Kirtman, B. P., and LEE, S.-K. (2009). Climate Response of the Equatorial Pacific to Global Warming. *Journal of Climate*, 22(18):4873–4892.

Doucet, A., De Freitas, N., and Gordon, N. (2001). *Sequential Monte Carlo methods in practice.* Springer.

Doucet, A., Godsill, S., and Andrieu, C. (2000). On sequential Monte Carlo sampling methods for Bayesian filtering. *Statistics and Computing.*

Emery, W. and Thomson, R. E. (1998). *Data and their analysis methods in physical oceanography.* Pergamon Press, Amsterdam.

Evensen, G. (1994). Sequential data assimilation with a nonlinear quasi-geostrophic model using Monte Carlo methods to forecast error statistics. *Journal of Geophysical Research*, 99:10–10.

Evensen, G. (2003). The Ensemble Kalman Filter: theoretical formulation and practical implementation. *Ocean Dynamics*, 53(4):343–367.

Ezer, T. and Mellor, G. L. (1994). Continuous assimilation of geosat altimeter data into a three-dimensional primitive equation gulf stream model. *Journal of Physical Oceanography*, 24:832–847.

Fairall, C. W., Bradley, E., Rogers, D., Edson, J., and Young, G. (1996). Bulk parameterization of air-sea fluxes for tropical ocean-global atmosphere coupled-ocean atmosphere response experiment. *Journal of Geophysical Research.*

Flatau, M., Flatau, P., Phoebus, P., and Niiler, P. (1997). The feedback between equatorial convection and local radiative and evaporative processes: The implications for intraseasonal oscillations. *Journal of the Atmospheric Sciences.*

Forget, G. (2010). Mapping Ocean Observations in a Dynamical Framework: A 2004–06 Ocean Atlas. *Journal of Physical Oceanography.*

Gandin, L. S. (1965). *Objective analysis of meteorological fields.* Israel Program for Scientific Translations, Jerusalem.

Garreaud, R. and Muñoz, R. (2005). The low-level jet off the west coast of subtropical South America: Structure and variability. *Monthly Weather Review.*

Gastineau, G. and Soden, B. J. (2009). Model projected changes of extreme wind events in response to global warming. *Geophysical Research Letters*, 36:L10810.

Gent, P. R., Danabasoglu, G., Donner, L. J., Holland, M. M., Hunke, E. C., Jayne, S. R., Lawrence, D. M., Neale, R. B., Rasch, P. J., Vertenstein, M., Worley, P. H., Yang, Z.-L., and Zhang, M. (2010). The Community Climate System Model Version 4. *J Climate*, pages 1–16.

Gent, P. R., Danabasoglu, G., Donner, L. J., Holland, M. M., Hunke, E. C., Jayne, S. R., Lawrence, D. M., Neale, R. B., Rasch, P. J., Vertenstein, M., Worley, P. H., Yang, Z.-L., and Zhang, M. (2011). The Community Climate System Model Version 4. *Journal of Climate.*

Gershgorin, B. and Majda, A. (2010). Filtering a nonlinear slow-fast system with strong fast forcing. *Comm Math Sci*, 8(1):67–92.

Ghil, M., Ide, K., Bennett, A. F., Courtier, P., Kimoto, M., and Sato, N., editors (1997). *Data Assimilation in Meteorology and Oceanography: Theory and Practice*. Meteorological Society of Japan and Universal Academy Press, Tokyo.

Ghil, M. and Malanotte-Rizzoli, P. (1991). Data assimilation in meteorology and oceanography. *Adv. Geophys.*, 33:141–266.

Gill, A. and Niller, P. (1973). The theory of the seasonal variability in the ocean. *Deep Sea Research and Oceanographic Abstracts*.

Gordon, A. (1986). Interocean exchange of thermocline water. *Journal of Geophysical Research*, 91:5037–5046.

Gordon, C., Rosati, A., and Gudgel, R. (2010). Tropical sensitivity of a coupled model to specified ISCCP low clouds. *Journal of Climate*.

Gordon, N., Salmond, D., and Smith, A. (1993). Novel approach to nonlinear/non-Gaussian Bayesian state estimation. *Radar and Signal Processing, IEE Proceedings F*, 140(2):107–113.

Goswami, B., Ajayamohan, R., Xavier, P., and Sengupta, D. (2003). Clustering of synoptic activity by Indian summer monsoon intraseasonal oscillations. *Geophysical Research Letters*, 30(8).

Goswami, B., Krishnamurthy, V., and Annmalai, H. (1999). A broad-scale circulation index for the interannual variability of the Indian summer monsoon. *Q.J.R. Meteorol. Soc.*, 125(554):611–633.

Goswami, B. and Mohan, R. (2001). Intraseasonal oscillations and interannual variability of the Indian summer monsoon. *J Climate*, 14:1180–1198.

Gregory, D., Kershaw, R., and Inness, P. M. (1997). Parametrization of momentum transport by convection. II: Tests in singlecolumn and general circulation models. *Q.J.R. Meteorol. Soc.*, 123:1153–1183.

Hamill, T., Whitaker, J., and Snyder, C. (2001). Distance-dependent filtering of background error covariance estimates in an ensemble Kalman filter. *Monthly Weather Review*, 129(11):2776–2790.

Hayashi, Y. and Golder, D. (1986). Tropical intraseasonal oscillations appearing in a GFDL general circulation model and FGGE data. Part I: Phase propagation. *J. Atmos. Sci.*

Hayashi, Y. and Golder, D. (1988). Tropical intraseasonal oscillations appearing in a GFDL general circulation model and FGGE data. Part II: Structure. *J. Atmos. Sci.*

Held, I. M. and Soden, B. (2006). Robust responses of the hydrological cycle to global warming. *Journal of Climate.*

Hendon, H., Wheeler, M., and Zhang, C. (2007). Seasonal dependence of the MJO-ENSO relationship. *J Climate*, 20:531–543.

Hendon, H. H. and Salby, M. (1994). The life cycle of the Madden–Julian oscillation. *Journal of the Atmospheric Sciences.*

Hendon, H. H. and Wheeler, M. C. (2008). Some Space–Time Spectral Analyses of Tropical Convection and Planetary-Scale Waves. *Journal of the Atmospheric Sciences*, 65(9):2936–2948.

Holland, W. R. and Hirschman, A. D. (1972). A numerical calculation of the circulation in the north atlantic ocean. *Journal of Physical Oceanography*, 2:336–354.

Holland, W. R. and Malanotte-Rizzoli, P. (1989). Assimilation of altimeter data into an ocean circulation model: space versus time resolution studies. *Journal of Physical Oceanography*, 19:1507–1534.

Holte, J., Straneo, F., Moffat, C., Weller, B., and Farrar, T. (2012). Structure, properties, and heat content of eddies in the southeast Pacific Ocean. *Journal of Physical Oceanography.*

Hormazabal, S., Núñez, S., Arcos, D., Espindola, F., and Yuras, G. (2004). Mesoscale eddies and pelagic fishery off central Chile (33-40S). *Gayana (Concepción).*

Hoteit, I. and Köhl, A. (2006). Efficiency of reduced-order, time-dependent adjoint data assimilation approaches. *Journal of Oceanography*, 62(4):539–550.

Hoteit, I., Korres, G., and Triantafyllou, G. (2005). Comparison of extended and ensemble based Kalman filters with low and high resolution primitive equation ocean models. *Nonlinear Processes in Geophysics*, 12(5):755–765.

Hoteit, I., Pham, D., Triantafyllou, G., and Korres, G. (2008). Particle Kalman filtering for data assimilation in meteorology and oceanography. *Under Preparation.*

Houtekamer, P. and Mitchell, H. (2005). Ensemble Kalman filtering. *Quarterly Journal of the Royal Meteorological Society*, 131(613):3269–3289.

Huffman, G. J., Adler, R. F., Morrissey, M. M., Bolvin, D. T., Curtis, S., Joyce, R., Mcgavock, B., and Susskind, J. (2001). Global Precipitation at One-Degree Daily Resolution from Multisatellite Observations. *Journal of Hydrometeorology*, 2:36–50.

Inness, P., Slingo, J., and Guilyardi, E. (2003). Simulation of the Madden-Julian Oscillation in a coupled general circulation model. Part II: The role of the basic state. *Journal of Climate.*

Isern-Fontanet, J., García-Ladona, E., and Font, J. (2003). Identification of marine eddies from altimetric maps. *Journal of Atmospheric and Oceanic Technology.*

Isoguchi, O. and Kawamura, H. (2006). MJO-related summer cooling and phytoplankton blooms in the South China Sea in recent years. *Geophysical Research Letters*, 33(16):L16615–.

Jardak, M., Navon, I., and Zupanski, M. (2010). Comparison of Sequential data assimilation methods for the Kuramoto-Sivashinsky equation. *International Journal for Numerical Methods in Fluids*, 62:374–402.

Jochum, M. (2009). Impact of latitudinal variations in vertical diffusivity on climate simulations. *Journal of Geophysical Research*, 114(C1):C01010.

Johnson, G. C. and McTaggart, K. E. (2010). Equatorial Pacific 13 °C Water Eddies in the Eastern Subtropical South Pacific Ocean*. *Journal of Physical Oceanography.*

Jones, C. (2000). The influence of intraseasonal variations on medium-to extended-range weather forecasts over South America. *Monthly Weather Review.*

Jones, C. and Carvalho, L. (2006). Changes in the Activity of the Madden-Julian Oscillation during 1958-2004. *Journal of Climate.*

Jones, C. and Carvalho, L. (2011). Will global warming modify the activity of the Madden–Julian Oscillation? *Quarterly Journal of the Royal Meteorological Society.*

Jones, C., Carvalho, L., and Higgins, R. W. (2004a). A statistical forecast model of tropical intraseasonal convective anomalies. *Journal of . . . .*

Jones, C., Waliser, D. E., and Lau, K. (2004b). Global occurrences of extreme precipitation and the Madden-Julian Oscillation: Observations and predictability. *Journal of Climate.*

Kalnay, E., Kanamitsu, M., Kistler, R., Collins, W., Deaven, D., Gandin, L., Iredell, M., Saha, S., White, G., Woollen, J., Zhu, Y., Leetmaa, A., Reynolds, R., Chelliah, M., Ebisuzaki, W., WHiggins, Janowiak, J., Mo, K. C., Ropelewski,

C., Wang, J., Jenne, R., and Joseph, D. (1996). The NCEP/NCAR 40-year reanalysis project. *Bulletin of the American Meteorological Society*, 77(3):437–471.

Kalnay, E., Li, H., Miyoshi, T., Yang, S.-C., and Ballabrera-Poy, J. (2007). 4-D-Var or ensemble Kalman filter? *Tellus A*, 59(5):758–773.

Karstensen, J. (2004). Formation of the South Pacific Shallow Salinity Minimum: A Southern Ocean Pathway to the Tropical Pacific. *Journal of Physical Oceanography*.

Kemball-Cook, S. R. and Weare, B. C. (2001). The Onset of Convection in the Madden–Julian Oscillation. *Journal of Climate*, 14.

Kepert, J. D. (2004). On ensemble representation of the observation-error covariance in the Ensemble Kalman Filter. *Ocean Dynamics*, 54(6):561–569.

Kessler, W. (2001). EOF representations of the madden–julian oscillation and its connection with enso. *J Climate*, 14(13):3055–3061.

Kessler, W. and Kleeman, R. (2000). Rectification of the Madden–Julian oscillation into the ENSO cycle. *Journal of Climate*, 13:3560–3575.

Kiehl, J. and Gent, P. (2004). The community climate system model, version 2. *Journal of Climate*.

Killworth, P. D., Dieterich, C., Le Provost, C., Oschlies, A., and Willebrand, J. (2001). Assimilation of altimetric data and mean sea surface height into an eddy-permitting model of the north atlantic. *Progress in Oceanography*, 48:313–335.

Kim, D., Sperber, K., Stern, W., Waliser, D., Kang, I., Maloney, E., Wang, W., Weickmann, K., Benedict, J., Khairoutdinov, M., Lee, M. I., Neale, R., Suarez, M., Thayer-Calder, K., and Zhang, G. (2009a). Application of MJO simulation diagnostics to climate models. *J. Clim*, 22:6413–6436.

Kim, D., Sperber, K., Stern, W., Waliser, D. E., Kang, I., Maloney, E., Wang, W., Weickmann, K., Benedict, J. J., Khairoutdinov, M., Lee, M. I., Neale, R. B., Suarez, M., Thayer-Calder, K., and Zhang, G. (2009b). Application of MJO simulation diagnostics to climate models. *J. Clim*.

Kim, J.-H., Ho, C.-H., Kim, H.-S., Sui, C.-H., and Park, S. K. (2008). Systematic Variation of Summertime Tropical Cyclone Activity in the Western North Pacific in Relation to the Madden–Julian Oscillation. *Journal of Climate*, 21(6):1171–1191.

Kivman, G. (2003). Sequential parameter estimation for stochastic systems. *Nonlinear Processes in Geophysics*, 10:253–259.

Klein, S. and Hartmann, D. (1993). The seasonal cycle of low stratiform clouds. *Journal of Climate*.

Krishnamurthy, V. and Kirtman, B. (2003). Variability of the Indian Ocean: Relation to monsoon and ENSO. *QJR Meteorol. Soc*, 129(590):1623–1646.

Kug, J., Sooraj, K., Jin, F., and Luo, J. (2009). Impact of Indian Ocean Dipole on high-frequency atmospheric variability over the Indian Ocean. *Atmospheric research*, 94:134–139.

Large, W. G. and Danabasoglu, G. (2006). Attribution and Impacts of Upper-Ocean Biases in CCSM3. *Journal of Climate*.

Large, W. G. and Yeager, S. (2009). The Global Climatology of an Interannually varying Air-Sea Flux Dataset. *Clim. Dyn.*, 33(2):341–364.

Lau, N. and Lau, K. (1986). The structure and propagation of intraseasonal oscillations appearing in a GFDL general circulation model. *Journal of the Atmospheric Sciences*.

Lau, W. (2005). El nino southern oscillation connection. In Lau, W. and Waliser, D., editors, *Intraseasonal Variability in the Atmosphere-Ocean Climate System*, pages 271–305. Praxis. Springer Berlin Heidelberg.

Lau, W. and Waliser, D. (2005a). *Intraseasonal variability in the atmosphere-ocean climate system*. Springer-Praxis.

Lau, W. and Waliser, D. E. (2005b). *Intraseasonal variability in the atmosphere-ocean climate system*. Springer.

Le Dimet, F. and Talagrand, O. (1986). Variational algorithms for analysis and assimilation of meteorological observations: Theoretical aspects. *Tellus*, 38(2):97–110.

Leetmaa, A., Behringer, D., Huyer, A., Smith, R., and Toole, J. (1987). Hydrographic conditions in the Eastern Pacific before, during and after the 1982/83 El Niño. *Prog. Oceanogr.*

Lermusiaux, P. F. J. and Robinson, A. R. (1999). Data assimilation via error subspace statistical estimation.part i: Theory and schemes. *Monthly Weather Review*, 127:1385–1407.

Lewis, J., Lakshmivarahan, S., and Dhall, S. (2006). *Dynamic Data Assimilation: A Least Squares Approach*. Cambridge University Press, Cambridge.

Lewis, J. M. and Derber, J. (1985). The use of adjoint equations to solve a variational adjustment problem with advective constraints. *Tellus A*.

Liebmann, B., Hendon, H., and Glick, J. (1994). The relationship between tropical cyclones of the western Pacific and Indian Oceans and the Madden–Julian oscillation. *J. Meteor. Soc. Japan*, 72(41):1–412.

Liebmann, B. and Smith, C. (1996). Description of a complete (interpolated) outgoing longwave radiation dataset. *Bulletin of the American Meteorological Society*, 77(6):1275–1277.

Lin, J., Weickmann, K., Kiladis, G., Mapes, B., Sperber, K., Lin, W., Wheeler, M., Schubert, S., Genio, A. D., Donner, L., Emori, S., Gueremy, J.-F., Hourdin, F., Rasch, P. J., Roeckner, E., and Scinocca, J. F. (2006a). Tropical intraseasonal variability in 14 IPCC AR4 climate models. Part I: Convective signals. *J Climate*, 19(12):2665–2690.

Lin, J., Weickmann, K., Kiladis, G., Mapes, B., Sperber, K., Lin, W., Wheeler, M., Schubert, S., Genio, A. D., Donner, L. J., Emori, S., Gueremy, J.-F., Hourdin, F., Rasch, P. J., Roeckner, E., and Scinocca, J. F. (2006b). Tropical intraseasonal variability in 14 IPCC AR4 climate models. Part I: Convective signals. *Journal of Climate*, 19(12):2665–2690.

Lin, J.-L. (2007). The Double-ITCZ Problem in IPCC AR4 Coupled GCMs: Ocean–Atmosphere Feedback Analysis. *Journal of Climate*.

Lin, S. (2004). A "vertically Lagrangian" finite-volume dynamical core for global models. *Monthly Weather Review*, 132:2293–2307.

Liu, Z., Vavrus, S., He, F., Wen, N., and Zhong, Y. (2005). Rethinking Tropical Ocean Response to Global Warming: The Enhanced Equatorial Warming*. *Journal of Climate*, 18(22):4684–4700.

Lorenc, A. (2003). The potential of the ensemble Kalman filter for NWP-a comparison with 4D-Var. *Quarterly Journal of the Royal Meteorological Society*, 129(595):3183–3203.

Lorenz, E. (1986). On the existence of a slow manifold. *Journal of the Atmospheric Sciences*.

Lorenz, E. (1991). Dimension of weather and climate attractors. *Nature*, 353:241–244.

Lu, C. and Browning, G. L. (1998). The impact of observational errors on objective analyses. *Journal of Atmospheric Sciences*, 55:1791–1807.

Lukas, R. (1986). The termination of the Equatorial Undercurrent in the eastern Pacific. *Progress in Oceanography*.

Lynch, P. (2006). *The emergence of numerical weather prediction: Richardson's dream.* Cambridge University Press.

Ma, C., Mechoso, C. R., and Robertson, A. (1996a). Peruvian stratus clouds and the tropical Pacific circulation: A coupled ocean-atmosphere GCM study. *Journal of Climate.*

Ma, C., Mechoso, C. R., Robertson, A., and Arakawa, A. (1996b). Peruvian stratus clouds and the tropical Pacific circulation: A coupled ocean-atmosphere GCM study. *Journal of Climate.*

Madden, R. and Julian, P. (1971a). Detection of a 40–50 day oscillation in the zonal wind in the tropical Pacific. *Journal of the Atmospheric Sciences*, 28:702–708.

Madden, R. and Julian, P. (1972). Description of global-scale circulation cells in the tropics with a 40-50 day period. *Journal of the Atmospheric Sciences*, 29(6):1109–1123.

Madden, R. and Julian, P. (1994a). Observations of the 40–50-day tropical oscillation—A review. *Monthly Weather Rev*, 122:814–837.

Madden, R. A. (1994). Observations of the 40-50-day tropical oscillation-A review. *Monthly Weather Review.*

Madden, R. A. and Julian, P. (1971b). Detection of a 40–50 day oscillation in the zonal wind in the tropical Pacific. *Journal of the Atmospheric Sciences.*

Madden, R. A. and Julian, P. (1994b). Observations of the 40–50-day tropical oscillation—A review. *Monthly Weather Review.*

Malanotte-Rizzoli, P. and Tziperman, E. (1996). The oceanographic data assimilation problem: Overview, motivation and purposes. In Malanotte-Rizzoli, P., editor, *Modern Approaches to Data Assimilation in Ocean Modeling*, pages 3–17. Elsevier Science B. V., Amsterdam, The Netherlands.

Malanotte-Rizzoli, P. and Young, R. E. (1995). Assimilation of global versus local data sets into a regional model of the gulf stream system: 1. data effectiveness. *J. Geophys. Res.*, 100:24,773–24,796.

Maloney, E. and Hartmann, D. (2000a). Modulation of eastern North Pacific hurricanes by the Madden–Julian oscillation. *Journal of Climate*, 13:1451–1460.

Maloney, E. D. (2000). Modulation of Hurricane Activity in the Gulf of Mexico by the Madden-Julian Oscillation. *Science*, 287(5460):2002–2004.

Maloney, E. D. and Hartmann, D. (2000b). Modulation of hurricane activity in the Gulf of Mexico by the Madden-Julian oscillation. *Science*, 287:2002–2004.

Marchesiello, P., McWilliams, J., and Shchepetkin, A. (2003). Equilibrium structure and dynamics of the California Current System. *Journal of Physical Oceanography*.

Marshall, A., Alves, O., and Hendon, H. (2009). A coupled GCM analysis of MJO activity at the onset of El Nino. *Journal of the Atmospheric Sciences*, 66:966–983.

Matthews, A. (2004). Atmospheric response to observed intraseasonal tropical sea surface temperature anomalies. *Geophysical Research Letters*.

Matthews, A., Singhruck, P., and Heywood, K. J. (2007). Deep ocean impact of a Madden-Julian oscillation observed by Argo floats. *Science*, 318(5857):1765–1769.

McCreary Jr, J. (1985). Modeling equatorial ocean circulation. *Annual Review of Fluid Mechanics*.

McIntosh, P. C. (1977). Oceanic data interpolation: Objective analysis and splines. *J. Geophys. Res.*, 95:13,529–13,541.

McLachlan, G. and Peel, D. (2000). *Finite mixture models*. John Wiley & Sons, Inc.

McPhaden, M. (1999). Genesis and evolution of the 1997-98 El Niño. *Science*.

McWilliams, J. C. (1984). Emergence of isolated coherent vortices in turbulent flow. *Journal of Fluid Mechanics*.

Mcwilliams, J. C. and Flierl, G. (1979). On the evolution of isolated, nonlinear vortices. *Journal of Physical Oceanography*.

Mechoso, C. R., Robertson, A., Barth, N., and Davey, M. (1995). The seasonal cycle over the tropical Pacific in coupled ocean–atmosphere general . . . . *Monthly Weather Review*.

Mellor, G. and Yamada, T. (1982). Developement of a turbulence closure model for geophysical fluid problems. *Rev. Geophys. Space Phys.*, 20:851–875.

Mellor, G. L. and Ezer, T. (1991). A gulf stream model and an altimetry assimilation scheme. *Journal of Geophysical Research*, 96:8779–8795.

Miller, R. (1997). Tropical thermostats and low cloud cover. *Journal of Climate*.

Mitchell, H., Houtekamer, P., and Pellerin, G. (2002). Ensemble size, balance, and model-error representation in an ensemble Kalman filter. *Monthly Weather Review*, 130:2791–2808.

Montes, I., Colas, F., Capet, X., and Schneider, W. (2010a). On the pathways of the equatorial subsurface currents in the eastern equatorial Pacific and their contributions to the Peru-Chile Undercurrent. *Journal of Geophysical Research.*

Montes, I., Colas, F., Capet, X., and Schneider, W. (2010b). On the pathways of the equatorial subsurface currents in the eastern equatorial Pacific and their contributions to the Peru-Chile Undercurrent. *Journal of Geophysical Research.*

Moore, A., Arango, H. G., Di Lorenzo, E., Cornuelle, B., Miller, A., and Neilson, D. (2004). A comprehensive ocean prediction and analysis system based on the tangent linear and adjoint of a regional ocean model. *Ocean Model.*

Moore, A. M., Arango, H. G., Broquet, G., Edwards, C., Veneziani, M., Powell, B., Foley, D., Doyle, J., Costa, D., and Robinson, P. (2011). The Regional Ocean Modeling System (ROMS) 4-dimensional variational data assimilation systems. Part II: Performance and Application to the California Current System. *Prog. Oceanogr.*

Morrow, R., Birol, F., Griffin, D., and Sudre, J. (2004). Divergent pathways of cyclonic and anti-cyclonic ocean eddies. *Geophysical Research Letters.*

Nakano, S., Ueno, G., and Higuchi, T. (2007). Merging particle filter for sequential data assimilation. *Nonlinear Processes in Geophysics*, 14:395–408.

Neale, R., Richter, J., and Jochum, M. (2008). The impact of convection on ENSO: From a delayed oscillator to a series of events. *J Climate*, 21(22):5904–5924.

Neef, L. J., Polavarapu, S., and Shepherd, T. (2009). A low-order model investigation of the analysis of gravity waves in the Ensemble Kalman Filter. *Journal of the Atmospheric Sciences*, 66(6):1717–1734.

Neef, L. J., Polavarapu, S. M., and Shepherd, T. G. (2006). Four-Dimensional Data Assimilation and Balanced Dynamics. *Journal of the Atmospheric Sciences*, 63(7):1840.

Newman, M., Sardeshmukh, P., and Penland, C. (2009). How important is air-sea coupling in ENSO and MJO evolution? *Journal of Climate*, 22:2958–2977.

Okubo, A. (1970). Horizontal dispersion of floatable particles in the vicinity of velocity singularities such as convergences. *Deep Sea Research and Oceanographic Abstracts.*

Panofsky, R. A. (1949). Objective weather-map analysis. *Journal of the Atmospheric Sciences*, 6(6):386–392.

Pasquero, C., Provenzale, A., and Babiano, A. (2001). Parameterization of dispersion in two-dimensional turbulence. *Journal of Fluid Mechanics.*

Penven, P. (2005). Average circulation, seasonal cycle, and mesoscale dynamics of the Peru Current System: A modeling approach. *Journal of Geophysical Research.*

Pham, D. (2001). Stochastic methods for sequential data assimilation in strongly nonlinear systems. *Monthly Weather Review*, 129.

Pohl, B., Fauchereau, N., Reason, C., and Rouault, M. (2010). Relationships between the Antarctic Oscillation, the Madden-Julian Oscillation, and ENSO, and consequences for Rainfall Analysis. *J Climate*, 23(2):238–254.

Pohl, B. and Matthews, A. (2007). Observed changes in the lifetime and amplitude of the Madden-Julian oscillation associated with interannual ENSO sea surface temperature anomalies. *Journal of Climate.*

Polavarapu, S., Tanguay, M., and Fillion, L. (2000). Four-Dimensional Variational Data Assimilation with Digital Filter Initialization. *Monthly Weather Review*, 128:2491–2510.

Powell, B., Arango, H., Moore, A., Di Lorenzo, E., Milliff, R., and Foley, D. (2008). 4DVAR data assimilation in the intra-Americas sea with the Regional Ocean Modeling System (ROMS). *Ocean Model.*

Powell, B., Moore, A., Arango, H., Di Lorenzo, E., Milliff, R., and Leben, R. (2009). Near real-time ocean circulation assimilation and prediction in the Intra-Americas Sea with ROMS. *Dyn. Atmos. Oceans.*

Pu, Z. and Hacker, J. (2009). Ensemble-based Kalman filters in strongly nonlinear dynamics. *Advances in Atmospheric Sciences*, 26(3):373–380.

Rao, S., Masson, S., Luo, J., Behera, S., and Yamagata, T. (2007). Termination of Indian Ocean Dipole events in a coupled general circulation model. *Journal of Climate*, 20:3018–3035.

Ray, P. and Zhang, C. (2010). A Case Study of the Mechanics of Extratropical Influence on the Initiation of the Madden–Julian Oscillation. *Journal of the Atmospheric Sciences*, 67(2):515–528.

Raymond, D. and Blyth, A. M. (1986). A stochastic mixing model for nonprecipitating cumulus clouds. *Journal of the Atmospheric Sciences*, 43(22):2708–2718.

Raymond, D. and Blyth, A. M. (1992). Extension of the stochastic mixing model to cumulonimbus clouds. *Journal of the Atmospheric Sciences*, 49(21):1968–1983.

Reed, R. and Halpern, D. (1976). Observations of the California Undercurrent off Washington and Vancouver Island. *Limnology and Oceanography.*

Reid, J. (1973). The shallow salinity minima of the Pacific Ocean. *Deep Sea Research and Oceanographic Abstracts*.

Richardson, L. (1922). *Weather prediction by numerical process*. Dover.

Richter, J. and Rasch, P. J. (2008). Effects of convective momentum transport on the atmospheric circulation in the Community Atmosphere Model, version 3. *J Climate*, 21:1487–1499.

Robinson, A. R. and Lermusiaux, P. (2004). Prediction systems with data assimilation for coupled ocean science and ocean acoustics. In Tolstoy, D. A., Shang, E., Teng, Y.-C., and Tolstoy, A., editors, *Theoretical and Computational Acoustics*. World Scientific Publishing Co. Pte. Ltd.

Roundy, P. (2008). Analysis of convectively coupled kelvin waves in the indian ocean mjo. *Journal of Atmospheric Sciences*, 65(4):1342–1359.

Roundy, P. and Kravitz, J. R. (2009). The association of the evolution of intraseasonal oscillations to ENSO phase. *Journal of Climate*, 22:381–395.

Saji, N., Goswami, B., Vinayachandran, P., and Yamagata, T. (1999). A dipole mode in the tropical Indian Ocean. *Nature*, 401(6751):360–363.

Salby, M., Garcia, R., and Hendon, H. H. (1994). Planetary-scale circulations in the presence of climatological and wave-induced heating. *Journal of the Atmospheric Sciences*.

Sardeshmukh, P. and Sura, P. (2007). Multiscale impacts of variable heating in climate. *J Climate*, 20(23):5677–5695.

Sarmiento, J. and Bryan, K. (1982). An ocean transport model for the north atlantic. *Journal of Geophysical Research*, 87:394–408.

Saujani, S. and Shepherd, T. G. (2006). A unified theory of balance in the extratropics. *Journal of Fluid Mechanics*, 569:447.

Schneider, T. (2009). Scaling of precipitation extremes over a wide range of climates simulated with an idealized GCM. *Journal of Climate*.

Schneider, T. (2010). The hydrological cycle over a wide range of climates simulated with an idealized GCM.

Schneider, T., O'Gorman, P. A., and Levine, X. (2009). Water vapor and the dynamics of climate changes. *arXiv.org*, physics.ao-ph.

Schneider, W., Fuenzalida, R., Rodríguez-Rubio, E., Garcés-Vargas, J., and Bravo, L. (2003). Characteristics and formation of eastern South Pacific intermediate water. *Geophysical Research Letters*.

Schott, F. M. V. and Send, U. (1994). Open ocean deep convection, mediterranean and greenland seas. In Rizzoli, P. and Robinson, A., editors, *Ocean processes in climate dynamics: Global and Mediterranean examples*, pages 203–225. Kluwer.

Slingo, J. and Annamalai, H. (2000). 1997: The el nino of the century and the response of the indian summer monsoon. *Monthly Weather Rev*, 128(6):1778–1797.

Slingo, J., Inness, P., Neale, R., Woolnough, S., and Yang, G. (2003). Scale interactions on diurnal toseasonal timescales and their relevanceto model systematic errors. *Annals of Geophysics*.

Slingo, J., Sperber, K., Boyle, J., Ceron, J., Dix, M., Dugas, B., Ebisuzaki, W., Fyfe, J., Gregory, D., Gueremy, J., Hack, J., Harzallah, A., Inness, P., Kittoh, A., Lau, W. K.-M., McAvaney, B., Madden, R., Matthews, A., Palmer, T. N., Park, C., Randall, D., and Renno, N. (1996a). Intraseasonal oscillations in 15 atmospheric general circulation models: Results from an AMIP diagnostic subproject. *Climate Dynamics*, 12(5):325–357.

Slingo, J., Sperber, K., Boyle, J., Ceron, J., Dix, M., Dugas, B., Ebisuzaki, W., Fyfe, J., Gregory, D., Gueremy, J.-F., Hack, J., Harzallah, A., Inness, P., Kittoh, A., Lau, W. K.-M., McAvaney, B., Madden, R. A., Matthews, A., Palmer, T. N., Park, C., Randall, D., and Renno, N. (1996b). Intraseasonal oscillations in 15 atmospheric general circulation models: Results from an AMIP diagnostic subproject. *Climate Dynamics*.

Slingo, J. M., Rowell, D. P., Sperber, K. R., and Nortley, F. (1999). On the predictability of the interannual behaviour of the Madden-Julian oscillation and its relationship with el Ni??o. *Quarterly Journal of the Royal Meteorological Society*, 125(554):583–609.

Snyder, C., Bengtsson, T., Bickel, P., and Anderson, J. (2008). Obstacles to High-Dimensional Particle Filtering. *Monthly Weather Review*, 136(12):4629.

Soden, B. (2007). Global warming and the weakening of the tropical circulation. *Journal of Climate*.

Song, H. (2011). *Sensitivity analysis, ocean state estimation and diagnostics in the California Current*. PhD thesis, UCSD.

Sperber, K. and Annamalai, H. (2008a). Coupled model simulations of boreal summer intraseasonal (30–50 day) variability, Part 1: Systematic errors and caution on use of metrics. *Climate Dynamics*, 31(2):345–372.

Sperber, K. R. and Annamalai, H. (2008b). Coupled model simulations of boreal summer intraseasonal (30–50 day) variability, Part 1: Systematic errors and caution on use of metrics. *Climate Dynamics*.

Stammer, D. and Wunsch, C. (1999). Temporal changes in eddy energy of the oceans. *Deep Sea Research-Part II-Topical Studies in Oceanography.*

Stevenson, S., Fox-Kemper, B., Jochum, M., Neale, R., Deser, C., and Meehl, G. (2011). Will there be a significant change to El Nino in the 21st century? *Journal of Climate.*

Strub, P., Mesías, J., and Montecino, V. (1998). Coastal ocean circulation off western South America . *The sea.*

Swart, N., Ansorge, I., and Lutjeharms, J. (2008). Detailed characterization of a cold Antarctic eddy. *Journal of Geophysical Research.*

Szunyogh, I., Kostelich, E., Gyarmati, G., and Patil, D. (2005). Assessing a local ensemble Kalman filter: perfect model experiments with the National Centers for Environmental Prediction global model. *Tellus A*, 57(A):528–545.

Takayabu, Y., Iguchi, T., Kachi, M., Shibata, A., and Kanzawa, H. (1999). Abrupt termination of the 1997–98 El Niño in response to a Madden–Julian oscillation. *Nature*, 402:279–282.

Tang, Y. and Yu, B. (2008). MJO and its relationship to ENSO. *J. Geophys. Res*, 113.

Tippett, M., Anderson, J., Bishop, C. H., Hamill, T. M., and Whitaker, J. (2003). Ensemble square root filters. *Monthly Weather Review*, 131(7):1485–1490.

Todling, R. (1999). Estimation theory and foundations of atmospheric data assimilation. *DAO Office Note.*

Todling, R. and Cohn, S. E. (1994). Suboptimal schemes for atmospheric data assimilation based on the Kalman filter. *Monthly Weather Review*, 122(11):2530.

Toniazzo, T., Mechoso, C. R., Shaffrey, L. C., and Slingo, J. M. (2009). Upper-ocean heat budget and ocean eddy transport in the south-east Pacific in a high-resolution coupled model. *Climate Dynamics.*

Treguier, A., Boebel, O., and Barnier, B. (2003). Agulhas eddy fluxes in a 1/6° Atlantic model 10.1016/S0967-0645(02)00396-X : Deep Sea Research Part II: Topical Studies in Oceanography — ScienceDirect.com. *Deep Sea Research Part II.*

Trenberth, K. E. (1989). Toga and atmospheric processes. understanding climate change. In A. Berger, R. E. D. and Kidson, J. W., editors, *Proc. of IUGG Symp-osium 15, Geophysical Monograph No. 52, IUGG Vol. 7*, pages 117–125, Washington, D.C. Amer. Geophys. Union.

Trenberth, K. E. and Solomon, A. (1993). Implications of global atmospheric spatial spectra for processing and displaying data. *J. Climate*, 6:531–545.

Tsuchiya, M. (1985). Evidence of a double-cell subtropical gyre in the South Atlantic Ocean. *Journal of Marine Research*.

Tsuchiya, M. and Talley, L. (1998). A Pacific hydrographic section at 88 W: Water-property distribution. *Journal of Geophysical Research*.

Tziperman, E., Thacker, C., Long, R. B., and Hwang, S. M. (1992). Oceanic data analysis using a general circulation model i - simulations. *Journal of Physical Oceanography*, 22:1434–1457.

Van Leeuwen, P. (2009). Particle filtering in geophysical systems. *Monthly Weather Review*, 137.

Van Leeuwen, P. J. (2010). Nonlinear data assimilation in geosciences: an extremely efficient particle filter. *Quarterly Journal of the Royal Meteorological Society*, 136(653):1991–1999.

Vecchi, G., Soden, B., Wittenberg, A., and Held, I. M. (2006). Weakening of tropical Pacific atmospheric circulation due to anthropogenic forcing. *Nature*.

Waliser, D., Sperber, K., Hendon, H., Kim, D., Maloney, E., Wheeler, M., Weickmann, K., Zhang, C., Donner, L., and Gottschalck, J. (2008). MJO simulation diagnostics. *J. Climate*, 22:3006–3030.

Waliser, D. E., Jin, K., Kang, I.-S., Stern, W. F., Schubert, S. D., Wu, M. L. C., Lau, K.-M., Lee, M.-I., Krishnamurthy, V., Kitoh, A., Meehl, G. A., Galin, V. Y., Satyan, V., Mandke, S. K., Wu, G., Liu, Y., and Park, C.-K. (2003). AGCM simulations of intraseasonal variability associated with the Asian summer monsoon. *Climate Dynamics*, 21(5-6):423–446.

Waliser, D. E. and Lau, K. (1999). The influence of coupled sea surface temperatures on the Madden-Julian oscillation: A model perturbation experiment. *Journal of the Atmospheric . . . .*

Waliser, D. E., Murtugudde, R., Strutton, P., and Li, J.-L. (2005). Subseasonal organization of ocean chlorophyll: Prospects for prediction based on the Madden-Julian Oscillation. *Geophysical Research Letters*, 32(23):L23602–.

Wang, B. and Rui, H. (1990). Dynamics of the coupled moist Kelvin–Rossby wave on an equatorial-plane. *J. Atmos. Sci.*

Wang, B. and Xie, X. (1997). A model for the boreal summer intraseasonal oscillation. *Journal of the Atmospheric Sciences*.

Webster, P., Moore, A., Loschnigg, J., and Leben, R. (1999). Coupled ocean-atmosphere dynamics in the Indian Ocean during 1997-98. *Nature*, 401(6751):356–360.

Webster, P. and Yang, S. (1992). Monsoon and ENSO: Selectively interactive systems. *Q.J.R. Meteorol. Soc.*, 118:877–926.

Weiss, J. (1991). The dynamics of enstrophy transfer in two-dimensional hydro-dynamics. *Physica D: Nonlinear Phenomena*.

Wheeler, M. and Hendon, H. (2004). An all-season real-time multivariate MJO index: Development of an index for monitoring and prediction. *Monthly Weather Review*, 132:1917–1932.

Wheeler, M. and McBride, J. (2004). Intraseasonal Variability of the Australian-Indonesian Monsoon Region. *Intraseasonal Variability of the Atmosphere-Ocean Climate System, WK-M. Lau and DE Waliser Eds., Praxis Publishing*.

Wigner, E. P. (1960). The unreasonable effectiveness of mathematics in the natural sciences. Richard courant lecture in mathematical sciences delivered at New York University, May 11, 1959. *Communications on Pure and Applied Mathematics*.

Wirosoetisno, D. and Shepherd, T. G. (2000). Averaging, slaving and balance dynamics in a simple atmospheric model. *Physica D: Nonlinear Phenomena*, 141(1-2):37–53.

Wood, R., Mechoso, C. R., Bretherton, C., Weller, R., Huebert, B., Straneo, F., Albrecht, B., Coe, H., Allen, G., Vaughan, G., Daum, P., Fairall, C., Chand, D., Klenner, L. G., Garreaud, R., Grados, C., Covert, D. S., Bates, T. S., Krejci, R., Russell, L. M., De Szoeke, S., Brewer, A., Yuter, S. E., Springston, S. R., Chaigneau, A., Toniazzo, T., Minnis, P., Palikonda, R., Abel, S. J., Brown, W. O. J., Williams, S., Fochesatto, J., Brioude, J., and Bower, K. N. (2011). The VAMOS Ocean-Cloud-Atmosphere-Land Study Regional Experiment (VOCALS-REx): goals, platforms, and field operations. *Atmos. Chem. Phys.*

Woodgate, R. A. and Killworth, P. D. (1997). The effects of assimilation on the physics of an ocean model. part i: Theoretical model and barotropic results. *Journal of Atmospheric and Oceanic Technology*, 14:897–909.

Wunsch, C. (1977). Determining the general circulation of the oceans: A preliminary discussion. *Science*, 196:871–875.

Wunsch, C. and Grant, B. (1982). Towards the general circulation of the north atlantic ocean. *Prog. in Oceanog.*, 11:1–59.

Wyrtki, K. (1967). Circulation and water masses in the eastern equatorial Pacific Ocean. *Int J Oceanol Limnol*.

Xie, P. and Arkin, P. (1997). Global precipitation: A 17-year monthly analysis based on gauge observations, satellite estimates, and numerical model outputs. *Bulletin of the American Meteorological Society*, 78(11):2539–2558.

Xie, S. (2004). Satellite observations of cool ocean–atmosphere interaction. *Bulletin of the American Meteorological Society*.

Xie, S., Miyama, T., Wang, Y., Xu, H., de Szoeke, S., Small, R., Richards, K., Mochizuki, T., and Awaji, T. (2007). A Regional Ocean–Atmosphere Model for Eastern Pacific Climate: Toward Reducing Tropical Biases. *Journal of Climate*.

Xie, S.-P., Deser, C., Vecchi, G. A., Ma, J., Teng, H., and Wittenberg, A. T. (2010). Global Warming Pattern Formation: Sea Surface Temperature and Rainfall*. *Journal of Climate*, 23(4):966–986.

Yáñez, E., Barbieri, M., Silva, C., Nieto, K., and Espindola, F. (2001). Climate variability and pelagic fisheries in northern Chile. *Prog. Oceanogr.*

Yasunari, T. (1979). Cloudiness fluctuations associated with the Northern Hemisphere summer monsoon. *J. Meteor. Soc. Japan*, 57:227–242.

Yuan, Y., Yang, H., Zhou, W., and Li, C. (2008). Influences of the Indian Ocean dipole on the Asian summer monsoon in the following year. *International Journal of Climatology*, 28(14):1849–1859.

Zavala-Garay, J., Zhang, C., Moore, A., and Kleeman, R. (2005). The linear response of ENSO to the Madden-Julian Oscillation. *J Climate*, 18(13):2441–2459.

Zhang, C. (2005a). Madden-Julian Oscillation. *Rev. Geophys.*, 43(2):1–36.

Zhang, C. (2005b). Madden-Julian Oscillation. *Reviews of Geophysics*, 43(2).

Zhang, C., Dong, M., Gualdi, S., Hendon, H., and Maloney, E. (2006a). Simulations of the Madden–Julian oscillation in four pairs of coupled and uncoupled global models. *Climate Dynamics*, 27:573–592.

Zhang, C., Dong, M., Gualdi, S., Hendon, H. H., and Maloney, E. (2006b). Simulations of the Madden–Julian oscillation in four pairs of coupled and uncoupled global models. *Climate Dynamics*.

Zhang, G. and McFarlane, N. A. (1995). Role of convective scale momentum transport in climate simulation. *Journal of Geophysical Research*, 100:1417–1426.

Zhang, G. J. and Mu, M. (2005). Convective quasi-equilibrium in the tropical western Pacific: Comparison with midlatitude continental environment. *Journal of Geophysical Research*, 18:4046–4063.

Zheng, Y., Shinoda, T., Kiladis, G., Lin, J., and Metzger, E. (2010). Upper Ocean Processes Under the Stratus Cloud Deck in the Southeast Pacific Ocean. *Journal of Physical Oceanography*.

Zheng, Y., Shinoda, T., Lin, J.-L., and Kiladis, G. N. (2011). Sea Surface Temperature Biases under the Stratus Cloud Deck in the Southeast Pacific Ocean in 19 IPCC AR4 Coupled General Circulation Models. *Journal of Climate*.

Zhou, L., Neale, R., Jochum, M., and Murtugudde, R. (2011a). Better Madden-Julian Oscillations with better physics: the impact of improved convection parameterizations. *J Climate (sub judice)*.

Zhou, L., Neale, R. B., Jochum, M., and Murtugudde, R. (2011b). Better Madden-Julian Oscillations with better physics: the impact of improved convection parameterizations. *Journal of Climate*.

Zou, Y. and Ghanem, R. (2005). A multiscale data assimilation with the ensemble Kalman filter. *Multiscale Modeling and Simulation*, 3(1):131–150.

Zveryaev, I. I. (2002). Interdecadal changes in the zonal wind and the intensity of intraseasonal oscillations during boreal summer Asian monsoon. *Tellus A*, 54(3):288–298.